Neutrino Oscillation Parameters and Optimization Techniques

Ghulam Mustafa

Submitted in Partial Fulfillment of the requirements for the Degree of

DOCTOR OF PHILOSOPHY

at

CENTRE FOR HIGH ENERGY PHYSICS
UNIVERSITY OF THE PUNJAB
LAHORE

DEDICATION

To my parents,

My wife and Usama Mustafa

DECLARATION

This thesis is being submitted to the University of the Punjab, to meet the partial requirements of the “DEGREE OF PHILOSOPHY” in the field of “High Energy Physics”. It does not contain any material already submitted for award of any degree or diploma in any university. To the best of my knowledge, there is no material published or written by another person, except with references. If any reference is found missing that would be completely unintentional and I do not pretend to own any credit for that.

Ghulam Mustafa

Doctoral Dissertation Certificate

It is certified that I have read this dissertation and that in my opinion; it is adequate in scope and quality as dissertation for the degree of “Doctor of Philosophy” in High Energy Physics.

Supervisor:

Asso. Prof. Dr. Bilal Masud
Centre for High Energy Physics,
University of the Punjab,
Lahore, Pakistan

Submitted Through:

Prof. Dr. Haris Rashid
Director
Centre for High Energy Physics,
University of the Punjab,
Lahore, Pakistan

Table of Contents

List of Tables

List of Figures

List of Publications

1. Ghulam Mustafa, Faisal Akram, Bilal Masud, *Optimization of the Neutrino Oscillation Parameters using Differential Evolution*, arXiv: 1109.2431v1 [physics.comp-ph] 12 Sep 2011.
   Journal reference: Commun. Theor. Phys. Vol. 59, No. 3, pp. 324-330, 2013.
   DOI: 10.1088/0253-6102/59/3/14

Acknowledgements

All praise for "ALMIGHTY ALLAH", whose Uniqueness, Oneness and Wholeness is unchangeable, who guided me in difficult and congeal circumstances. All respects for the Holy Prophet "HAZRAT MUHAMMAD (PBUH)", who provided us the unique and complete way of life.

This thesis builds on the work of hundreds of other people who have written on the topic of neutrino physics. There is no space to thank all of them individually. I nevertheless want to acknowledge those people who have made the biggest difference to me personally and professionally.

I express my sincere thanks to my respectable teacher and supervisor Dr. Bilal Masood for his proper guidance, valuable suggestions and encouraging attitude during my research work. May Allah bless him in every field of life.

I am thankful to Dr. Faisal Akram, for his proper guidance, providing the helpful material used in research and help in understanding the terminology used in the neutrino physics.

I am grateful to Professor Dr. Haris Rashid, Director, Center for High Energy Physics, for his valuable encouragement during my research work.

I acknowledge my gratitude to Dr. Fazal Mahmood and Dr. Afaq Ahmad for their encouragement to continue my studies.

We are thankful to the Higher Education Commission (HEC) of Pakistan for its financial support through Grant No.17-5-2(Ps2-044) HEC/Sch/2004.

GHULAM MUSTAFA

Abstract

We present a global analysis, through traditional and a new technique, of the solar neutrino data using total event rates of chlorine (Homestake), Gallax+GNO, SAGE, Superkamiokande and SNO detectors for the two neutrino case. The traditional is the grid search technique, where we calculate well known chi-square (χ^2) function for neutrino oscillations for a grid of the parameters Δm^2 and $\tan^2\theta$. We find our global minima in the LMA region with $\Delta m^2 = 2.512 \cdot 10^{-5}\text{eV}^2$ and $\tan^2\theta = 0.3981$. We also find local minimum χ^2 values in different regions of the parameter space. The new technique we chose is Differential Evolution. The Differential Evolution is a population based stochastic algorithm for optimization of real valued non-linear non-differentiable objective functions that has become very popular during the last decade. We combined this with the traditional grid based method for optimization of solar neutrino oscillation parameters Δm^2 and $\tan^2\theta$. We explore regions around the minima found in the global analysis using Differential Evolution for the fine tuning of the parameters, allowing even those values of the parameters which do not lie on any grid. We note as much as 4 times decrease in χ^2 value in the SMA region and even better goodness-of-fit as compared to our grid-based results. All this indicates a way out of the impasse faced due to CPU limitations of the larger grid method.

Chapter 1

Introduction

The flux of solar neutrinos was first measured by Raymond Davis Junior and John N. Bahcall at Homestake in late 1960s and a deficit was detected between theory (Standard Solar Model) and experiment [1]. This deficit is known as the *Solar Neutrino Problem*. Several theoretical explanations have been given to explain this deficit. One of these is neutrino oscillations, the change of electron neutrinos to an other neutrino flavour during their travel from a source point in the sun to the detector at the earth surface [2]. There was no experimental proof for the neutrino oscillations until 2002 when Sudbury Neutrino Observatory (SNO) provided strong evidence for neutrino oscillations [3]. The exact amount of depletion, which may be caused by the neutrino oscillations, however, depends upon the neutrino's mass-squared difference $\Delta m^2 \equiv m_2^2 - m_1^2$ (m_1 and m_2 being mass eigen-states of two neutrinos) and mixing angle θ, which defines the relation between flavour eigen-states and mass eigen-states of the neutrinos, in the interval $[0, \pi/2]$.

The data from different neutrino experiments have provided the base to explore the field of neutrino physics. In the global analysis of solar neutrino data, we calculate theoretically expected event rates with oscillations at different detector locations and combine it with experimental event rates statistically through the chi-square (χ^2) function, as defined below by Eq. (3.4.1) below, for a grid of values of the parameters Δm^2 and $\tan^2\theta$. The values of these parameters with minimum chi-square in different regions of the parameter space suggest different oscillation solutions. The names of these solutions, found in the

literature, along with specification of the regions in the parameter space are: Small Mixing Angle (SMA: $10^{-4} \leq \tan^2\theta \leq 3\times10^{-2},\ 3\times10^{-7}\mathrm{eV}^2 \leq \Delta m^2 \leq 10^{-4}\mathrm{eV}^2$), Large Mixing Angle (LMA: $3\times10^{-2} \leq \tan^2\theta \leq 2,\ 2\times10^{-6}\mathrm{eV}^2 \leq \Delta m^2 \leq 10^{-3}\mathrm{eV}^2$), Low Probability Low Mass (LOW: $3\times10^{-2} \leq \tan^2\theta \leq 2,\ 10^{-8}\mathrm{eV}^2 \leq \Delta m^2 \leq 2\times10^{-6}\mathrm{eV}^2$) and Vacuum Oscillation (VO: $0.1 \leq \tan^2\theta \leq 1,\ 10^{-11}\mathrm{eV}^2 \leq \Delta m^2 \leq 10^{-8}\mathrm{eV}^2$) [4]. Extensive work has been done on the global analysis of solar neutrino data [5, 6, 7, 8, 9, 10, 11, 12, 13, 14, 15] and now is the era of precision measurement of the neutrino oscillation parameters [16, 17].

Traditionally, we use grid search method where the whole parameter space ($10^{-4} \leq \tan^2\theta \leq 10,\ 10^{-13}\mathrm{eV}^2 \leq \Delta m^2 \leq 10^{-3}\mathrm{eV}^2$) is divided into a grid of points by assigning a variable to each parameter and varying its logarithm uniformly. The chi-square values are calculated for each point in the parameter space either by using ^{8}B flux constrained by the Standard Solar Model, e.g., BS05(OP) [18] in our case, or by using unconstrained ^{8}B flux [9] where it is varied about the value predicted by the Standard Solar Model. The global minimum chi-square value χ^2_{min} is found and $100\,\beta\%$ C.L. (Confidence Level) contours are drawn in the $\tan^2\theta - \Delta m^2$ plane by joining points with equal $\chi^2 (= \chi^2_{min} + \Delta\chi^2)$, where $\Delta\chi^2$ is the interval of χ^2 that gives a particular value of normalized area under the *chi-square distribution*. From the chi-square distribution one can easily find that $\Delta\chi^2 = 2.28, 4.61, 5.99, 9.21, 11.83$ for 68%, 90%, 95%, 99% and 99.73% C.L.[1] for two degrees of freedom. Minimum chi-square values are found in all the regions and the goodness-of-fit, corresponding to each of the minimum chi-square, is calculated. To find the each goodness-of-fit the chi-square distribution is used and confidence level $100(1-\beta)\%$, corresponding to the minimum chi-square in the region and the degree of freedom of the analysis, is calculated [4, 9]. In our analysis we used total event rates of chlorine (Homestake), Gallax+GNO, SAGE, Superkamiokande, SNO CC and NC experiments. So the number of degrees of freedom was 4 (6(rates)–2(parameters: $\tan^2\theta$ and $\Delta\mathrm{m}^2$)).

With the above mentioned traditional grid search method, we planned to combine

[1]Here β=0.68, 0.90, 0.95, 0.99 and 0.9973 respectively.

another optimization technique for the optimization of the chi-square function in our analysis. The possible direct search optimization techniques are: Annealed Nelder and Mead strategy [19], Adaptive Simulated Annealing [20], Genetic Algorithms [21], Evolution Strategies [22] and the Differential Evolution (DE) [23, 24]. We chose the DE for the purpose due to its ease to use, robustness and consistent convergence to the global minimum in consecutive independent trials .

When we use the Differential Evolution (DE), the parameters are randomly selected in the given range and checked for a decrease of chisquare, in contrast with the traditional grid based method as described above. Thus we selected the vectors with least chi-square values, in different regions of the selected grid, as starting points and used DE for the fine tuning of the parameters by exploring regions around the selected vectors in the parameter space.

In this dissertation, we have an overview of the fundamentals of neutrino physics, necessary for the global analysis of the neutrino data, in chapter 2. We describe standard solar model and the solar neutrino problem that resolves in the form of neutrinos' masses and their oscillations from one flavour to the other. We discuss the neutrino oscillations in some detail. In chapter 3, we discuss how to estimate the neutrino oscillation parameters, Δm^2 and $\tan^2\theta$, by the global analysis of the neutrino data. We find theoretical event rates for a grid of 101 $\times$ 101 values of the parameters and estimate the best fits, out of the grid by comparing each point in the parameter space with experimental result in chi-square analysis. In chapter 4, we explore regions around each of the best fit, found in the global analysis using grid-based method in chapter 3, for the fine tuning of the oscillation parameters using differential evolution. We discuss different optimization techniques in general and the differential evolution technique (DE), we have applied in our analysis, in detail. In the last chapter we summarize our conclusions. Some other results with different density grids and their comparisons with DE results, which are not included in this dissertation, are given in the published paper attached at the end of the thesis.

Chapter 2

Fundamentals of Neutrino Physics

The study of neutrino and its interaction with matter has resulted in a new branch of particle physics known as neutrino physics. It touches the areas of the High Energy Astrophysics, High Energy Physics Phenomenology, including the relevant experiments. Here we discuss the basics of neutrino physics we need for the global analysis of neutrino data and neutrino oscillation parameters.

2.1 Early History of Neutrino

The emission of continuous electron energy spectrum in β decay seemed to violate energy conservation, in the beginning of 20th century, whereas the kinematics of this apparently two body decay process implied mono-energetic beam of electrons. In 1930, Wolfgang Pauli suggested, in his famous letter [25], a third invisible particle that may carry the missing energy. Pauli named his proposed particle "neutron" (neutral one), but with Chadwick's discovery of neutron in 1932 [26], the particle was renamed "neutrino" (little neutral one) by Enrico Fermi. With the calculation of neutrino cross section $\sim 10^{-44}\text{cm}^2$, it was thought that there would be no direct way to detect the neutrino. But the attempts to detect the neutrinos were continued by the aficionados.

In 1956, Cowan and Reines, at the Savannah River nuclear reactor, succeeded in detecting antineutrino in the reaction $\overline{\nu} + p \rightarrow e^+ + n$. An antineutrino, from the nuclear reactor, interacts with the proton at the target producing a positron and a neutron. The

positron annihilates an electron and produce two gamma rays which are detected by the scintillator detectors. The neutron is slowed down and captured by the target [27]. This was the first achievement in detection of (anti)neutrinos that, along with Davis' failure to observe reactor neutrino capture with ^{37}Cl, led the distinction between neutrino and antineutrino.

Muon neutrino was discovered in 1961 at the Brookhaven AGS (Alternating Gradient Synchrotron) where muon, instead of electron, tracks were observed by neutrinos emitted in pion decay [28]. The particle emitted in the pion decay was called "muon neutrino" due to its different nature from "electron neutrino" emitted in β decay.

Tau neutrino (ν_τ) was proposed after the discovery of tau (τ) lepton in 1975 [29]. The ν_τ was experimentally detected in 2001 by the DONUT (Direct Observation of the NU Tau) experiment at Fermilab in the tau-decay of the charmed mesons [30].

Each of the three known types of neutrinos is associated with a massive lepton that experiences weak, electromagnetic, and gravitational forces, but not strong interactions. The known leptons are *electrons*, *muons* and *taus* (in increasing order of their rest masses) [31].

Neutrinos are produced on earth by natural radioactivity, by nuclear reactors, and by high energy accelerators. In the sun, neutrinos are produced by weak interactions that occur during nuclear fusion. Other sources of neutrinos may be atmospheric neutrinos, supernova neutrinos or neutrinos from collision of neutron stars. We focus here solar neutrinos that are electron neutrinos only. Solar neutrinos and their fluxes are best described by the standard solar model we discuss below.

2.2 Standard Solar Model

Solar models refer to mathematical treatment of the sun that has been used to calculate solar neutrino fluxes since 1962 [32]. Improvements with time have been made to the solar models. The solar model constructed with the best available physics and input data, at

its time, is referred to as "the standard solar model". In order to develop a solar model a detailed knowledge of the sun and its evolution is needed. Some parameters of the sun already known with direct or indirect measurements (upright characters) and others calculated by solar models (italic characters) are given in Table 2.1.

Table 2.1: Main Solar Parameters.

Parameter	Value
Mass ($M_\odot$)	1.99×10^{33}g
Radius ($R_\odot$)	6.96×10^{10}cm
Average Density	1.41 g/cm^3
Core Density	1.52×10^2g/cm^3
Luminosity ($L_\odot$)	3.84×10^{33}erg/s
Luminosity in ν's	0.023 ($L_\odot$)
Age	4.57×10^9y
Surface Temperature	6.78×10^3K
Core Temperature	15.7×10^6K
Heavy Element Mass ab.	0.02
Initial He mass ab.	0.27
Total ν flux on earth	6.55×10^{10}cm^{-2}s^{-}1

From the geological studies of the meteorites, the sun age is estimated to be 4.6×10^9y. Different theories for the production of solar energy have been given in the past. Theory of gravitational contraction have been dominant until the late of 19^{th} century that correspond to the solar age of only $3 \times 10^7 y$. With the discovery of nucleus and the mass-energy equivalence theories, the solar energy was started to be interpreted in terms of nuclear fusion reactions. After that, efforts have been made to produce solar models by the resolution of a set of state equations by imposing a few equilibrium assumptions along with the boundary conditions of the measured solar parameter (Table 2.1). Detail of the basic equations, describing evolution of the stars in general and the sun in particular, is available from refs. [33, 34].

All the nuclear reaction chains, as discussed below in section 2.2.1, in the sun imply four protons to fuse into a helium nucleus with the mass difference contributing to the

energy balance. In this way two protons are converted into two neutrons with the emission of two electron neutrinos.

Our sun is very opaque and we can observe electromagnetic radiations coming from its surface layers only. For this reason neutrino emissions in the nuclear reactions was considered of great astrophysical interest as it would make possible to look inside the Sun and a star in general [35]. But after the results from the Homestake experiment this perspective was reversed. The experimental observations clearly indicated the production of electron neutrinos in the sun but the measurements showed a clear deficit of neutrino flux in comparison to the theoretical expectations. This led to what is called *Solar Neutrino Problem* (SNP). The urge to solve the SNP motivated research to improve the solar models.

Different works describing solar neutrino aspects of solar models can be found in the refs. [36, 37, 38, 39, 40]. The currently used reference models are BS05(OP) by J.N. Bahcall and A.M. Serenelli [18] and BP04 by J.N. Bahcall and M.H. Pinsonneault [41]. For our work, we have used the Standard Solar Model BS05(OP) in all the calculations.

2.2.1 Nuclear Reactions in the Sun

In 1930s, Hans Bathe proposed that the sun's energy results from the nuclear fusion reaction where four hydrogen atoms fuse together to form one helium atom. The mass at the end of the process is less than the mass at the start. The difference of the mass is converted into energy according to the famous Einstein's mass-energy relation $E = mc^2$.

Two reaction sequences, pp-chain and CNO cycle, are dominant in nuclear fusion reactions of stars. The CNO cycle is dominant in stars larger than a few solar masses with a core having abundance of heavy elements. The pp-chain is responsible for about 99% of the nuclear energy released in the sun. The detail of both pp and CNO chains is presented in Table 2.2 with energy released per reaction. The Table 2.2 also describes the eight nuclear neutrino sources and neutrino energy from each of these reactions. The pp chain involves three different branches, PPI, PPII and PPIII, for three different ways

Table 2.2: Nuclear reactions in the Sun. First column indicates chain or cycle for the reaction identified in second column. Third column shows the total energy released by the reaction and the average energy carried by neutrinos is given in the fourth column. The usual name given to the neutrino fluxes is given in the small brackets. The effective energy responsible for the solar luminosity, from each reaction, is $Q_\gamma = Q - \langle Q_\nu \rangle$ [33].

Chain	Reaction	Q(MeV)	$\langle Q_\nu \rangle$(MeV)	No.
PPI	$p + p \longrightarrow {}^2H + e^+ + \nu_e + \gamma$	1.442	0.265(pp)	1
	$p + p + e^- \longrightarrow {}^2H + \nu_e$	1.442	1.442(pep)	2
	${}^2H + p \longrightarrow {}^3He + \gamma$	5.49	–	3
	${}^3He + {}^3He \longrightarrow {}^4He + 2p + \gamma$	12.86	–	4
PPII	${}^3He + {}^4He \longrightarrow {}^7Be + \gamma$	1.586	–	5
	${}^7Be + e^- \longrightarrow {}^7Li + \nu_e$	0.862(90%)	0.862(^{7}Be)	6
		0.384(10%)	0.384(^{7}Be)	
	${}^7Li + p \longrightarrow {}^4He + {}^4He + \gamma$	17.347	–	7
PIII	${}^7Be + p \longrightarrow {}^8B + \gamma$	0.137	–	8
	${}^8B \longrightarrow {}^4He + {}^4He + \nu_e + \gamma$	17.98	6.710(^{8}B)	9
	${}^3He + p \longrightarrow {}^4He + e^+ + \nu_e + \gamma$	19.795	9.625(hep)	10
Cycle	Reaction	Q(MeV)	$\langle Q_\nu \rangle$(MeV)	
CN	${}^{12}C + p \longrightarrow {}^{13}N + \gamma$	1.943	–	11
	${}^{13}N \longrightarrow {}^{13}C + e^+ + \nu_e$	2.221	0.7067(^{13}N)	12
	${}^{13}C + p \longrightarrow {}^{14}N + \gamma$	7.551	–	13
	${}^{14}N + p \longrightarrow {}^{15}O + \gamma$	7.297	–	14
	${}^{15}O \longrightarrow {}^{15}N + e^+ + \nu_e$	2.754	0.9965(^{15}O)	15
	${}^{15}N + p \longrightarrow {}^{12}C + {}^4He$	4.966	–	16
NO	${}^{15}N + p \longrightarrow {}^{16}O + \gamma$	12.128	–	17
	${}^{16}O + p \longrightarrow {}^{17}F + \gamma$	0.600	–	18
	${}^{17}F \longrightarrow {}^{17}O + e^+ + \nu_e$	2.762	0.9994(^{17}F)	19
	${}^{17}O + p \longrightarrow {}^{14}N + {}^4He$	1.19	–	20

in which ^{4}He nuclei are produced. The branching between PPI and PPII chains depends on the fate of ^{3}He nuclei, whereas the branching between PPII and PPIII chains depends on weather a ^{7}Be nuclei captures an electron or a proton. The CNO cycle, also known as CNO-bi-cycle, stands for Carbon-Nitrogen-Oxygen cycle. It is actually composed of two sub-cycles, the CN and the NO cycle as described in the Table 2.2.

2.2.2 Input Parameters for a Solar Model

The input parameters to construct a solar model, include nuclear S-factors: S_{11}, S_{33}, S_{34}, $S_{1,14}$, S_{17}, the Luminosity (Lum), the metallacity (Z/X), the sun age (Age) and the opacity (Opa). These parameters are denoted as $\{x_k\}_{k=1,....,9}$. All these are described below:

Nuclear S-Factors

Nuclear S-factors are related to nuclear cross sections of the different nuclear reactions described in pp-chain and SNO cycle. The detail of the Nuclear S-factors is available in the refs. [36, 42, 43]. In general, the nuclear cross sections can be expressed as

$$\sigma_{ij}(E) = S_{ij}(E)E^{-1}\exp(-2\pi\eta), \tag{2.2.1}$$

where $\eta = Z_1 Z_2(e^2/\hbar v)$, Z_1, Z_2 are two nuclear species and v is relative velocity. The factor $\exp(-2\pi\eta)$ is known as *Gamow Penetration factor*. The energy dependence of the cross section is given by the factor $S(E)$ known as "nuclear S-factor" or "astrophysical S-factor". At zero energy, the value of $S(E)$ is known as *cross section factor*, $S_\circ$. The indices of S show the nuclei involved in the reactions, for example, S_{33} and S_{34} show the S-factors of the reactions 4, ${}^3H_e({}^3H_e, 2p)^4He$ and 5, ${}^3H_e({}^3H_e, 2p)^4He$ in the table 2.2.

Solar Luminosity

J.N. Bahcall, in his work [44] has described the luminosity constraint of the solar neutrino fluxes. If the nuclear fusion reactions in the sun are responsible for the luminosity of the sun, the solar constant can be written as the linear combination of the solar neutrino fluxes as:

$$\frac{L_\odot}{4\pi(A.U.)^2} = \sum_i \alpha_i \Phi_i, \tag{2.2.2}$$

where $L_\odot$ is the solar luminosity at the earth surface and 1 $A.U.$ is the average of the earth sun distance. The coefficient α_i is energy provided to the star by the nuclear fusion reactions associated with the solar neutrino fluxes Φ_i.

Metallicity

The chemical abundances of the elements, present in the sun, affect the computed radiative opacity and hence the temperature-density profile of the solar interior. In the SSM, it is assumed that the present surface abundances of the elements reflect the initial abundance, the abundances at the time when our sun entered the hydrogen-burning phase (main sequence). The relative hydrogen, helium, and heavy element mass fractions are represented by X, Y, and Z respectively. The fractional abundance by mass of the elements heavier than helium is called the Metallicity.

The initial ratio by mass of elements heavier than helium relative to hydrogen, Z/X, is one of the crucial input parameters in the determination of the solar model. The fractional abundances of each of the elements are also important in determining the stellar opacity, which is closely linked to the predicted neutrino fluxes. Table 2.3 lists the individual fraction abundances of the heavy elements that are recommended by refs. [45, 46] and are used in SSM.

Solar Age

Before 1920, most of the physicists believed that the sun, and hence the earth, were only a few million years old. But Darwin's theory of biological evolution implied a time scale of several billion years. Also, geologists predicted that the ocean floor should be at least a billion years old to compare the features of sediments. Later, the radioactive dating, developed by Rutherford, made it evident the earth should be several billion years old. From this, and theory of the origin of the solar system, it is implied that the sun also should be several billion years old. The present age of the sun is determined accurately from meteoritic studies through radioactive dating process [47].

$$\text{Solar Age} \approx 4.57 \times 10^9 \text{y}$$

Table 2.3: Fractional abundances of heavy elements.

Element	Number fraction Grevesse [45]	Number fraction Aller [46]
C	0.29661	0.27983
N	0.05918	0.05846
O	0.49226	0.49761
Ne	0.06056	0.06869
Na	0.00129	0.00125
Mg	0.02302	0.02552
Al	0.00179	0.00198
Si	0.02149	0.02672
P	0.00017	0.00018
S	0.00982	0.01040
Cl	0.00019	0.00019
Ar	0.00230	0.00227
Ca	0.00139	0.00134
Ti	0.00006	0.00007
Cr	0.00028	0.00035
Mn	0.00017	0.00016
Fe	0.02833	0.02382
Ni	0.00108	0.00114
Total	1.000	1.000

Radiative Opacity

The radiative opacity is also a crucial input parameter. In the central region of the sun, energy transport is mainly due to the radiation (photons), while convection is dominant near the surface, and electron conduction in the innermost region. The higher the opacity, the slower becomes the heat transport, yielding a higher core temperature. The opacity depends on the elemental abundances and modeling of the complex atomic processes. The calculations require, for the solar interior, the use of large computer codes in order to include all of the known statistical mechanics and atomic physics [48].

The primary source for accurate astrophysical opacities has been, for many years, the Los Alamos National Laboratory codes, presumably developed for related thermonuclear applications. The units of density are $\mathrm{g\,cm^{-3}}$ and the units of temperature are 10^6K.

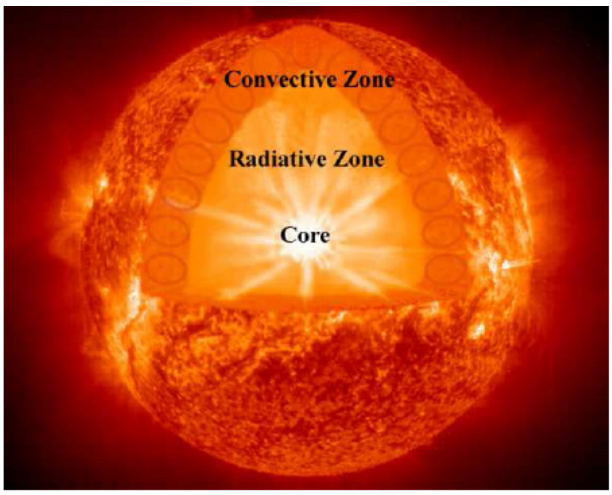

Figure 2.1: The Cross Section of the Sun.

Because the opacity determines in large part the temperature profile, the adopted opacity constitutes an important source of uncertainty for solar neutrino calculations. In 1982 Bahcall et al. [49] compared two different opacity calculations in the region of interest for solar interior calculations and concluded that the typical uncertainty is less than 10%.

2.2.3 Predictions of SSM

The **standard solar model** is calculated using the best available physics and input parameters at the time the model is constructed. Thus the set of numbers that correspond to the SSM has undergone an evolutionary process and improved with time. Some characteristics of the SSM are given in chapter 4 of the ref. [36]. Data for solar neutrino research is also available from the URL: http://www.sns.ias.edu/∼jnb/SNdata/sndata.html. Here we discuss briefly the predictions of the SSM in general and in the context of BP05(OP).

Internal Solar Structure

The solar core ($R < 0.3R_{\odot}$) occupies inner sphere of 30% of the solar radius. It has huge values of temperature and density given as below:

$$\text{Core temperature } \mathrm{T_c} = 1.5843 \times 10^7 \mathrm{K}$$

$$\text{Core density } \rho_{\text{c}} = 1.5843 \times 10^2 \text{g cm}^{-3}$$

This region has very high degree of ionization of the atoms. Almost all of the nuclear energy is produced in this region of the sun. The energy is produced in the form of heat and radiation. Different regions of the sun are shown in the figure 2.1.

The Radiation Zone $(0.3R_\odot < R < 0.71R_\odot)$ transfers energy, produced in solar core, in the form of radiation towards the outer surface. The efficiency of this region to transfer the radiation depends on solar opacity of the region. Solar opacity depends on the element composition and the degree of ionization (e.g high degree of ionization promotes the radiation transfer). Also, the temperature of the solar core depends on opacity values. If opacity is high, radiation is trapped in the core, and hence, core temperature increases.

The Convection zone $(0.71R_\odot < R < R_\odot)$ has low degree of ionization, which means photons cannot travel very long without scattering through the atomic electrons. However, in this region matter can move from place to place and can transfer energy through convection. The depth of the convective zone can be measured directly by the helioseismological studies. Fig 2.2 gives the radial profiles of different quantities as function of radius for the BS05(GS98) solar model. Panel (a) shows the luminosity L (solar units), temperature T ($10^7 K$), pressure P ($10^{17}\text{g cm}^{-3}\text{s}^{-2}$), density ρ (10^2g cm^{-3}), and enclosed mass m (solar units). L increases rapidly from the center and reaches reaches its surface value $\text{L}_\odot$ at $0.3R_\odot$. Panel (b) shows the ratio of the number density to the Avogadro's numbre N_A of the electron (n_e), neutron (n_n) and scatterers of the sterile neutrinos ($n_s = n_e - 0.5\, n_n$). To a good approximation, these quantities can be expressed in terms of ρ and the hydrogen mass fraction X as $n_e = \rho(1+X)/2$, $n_n = \rho(1-X)/2$ and $n_s = \rho(1+3X)/4$ [33]. Approximate Analytic expressions to these quantities can be found in ref. [50]. Panel (c) shows the hydrogen and helium mass fraction profiles. Dotted lines denote the initial hydrogen and helium mass fractions. The vertical dotted line denotes the location of the inner boundary of the convective envelope. Panel (d) is the same as panel (c) but for ^{12}C, ^{14}N, ^{16}O, and ^{3}He.

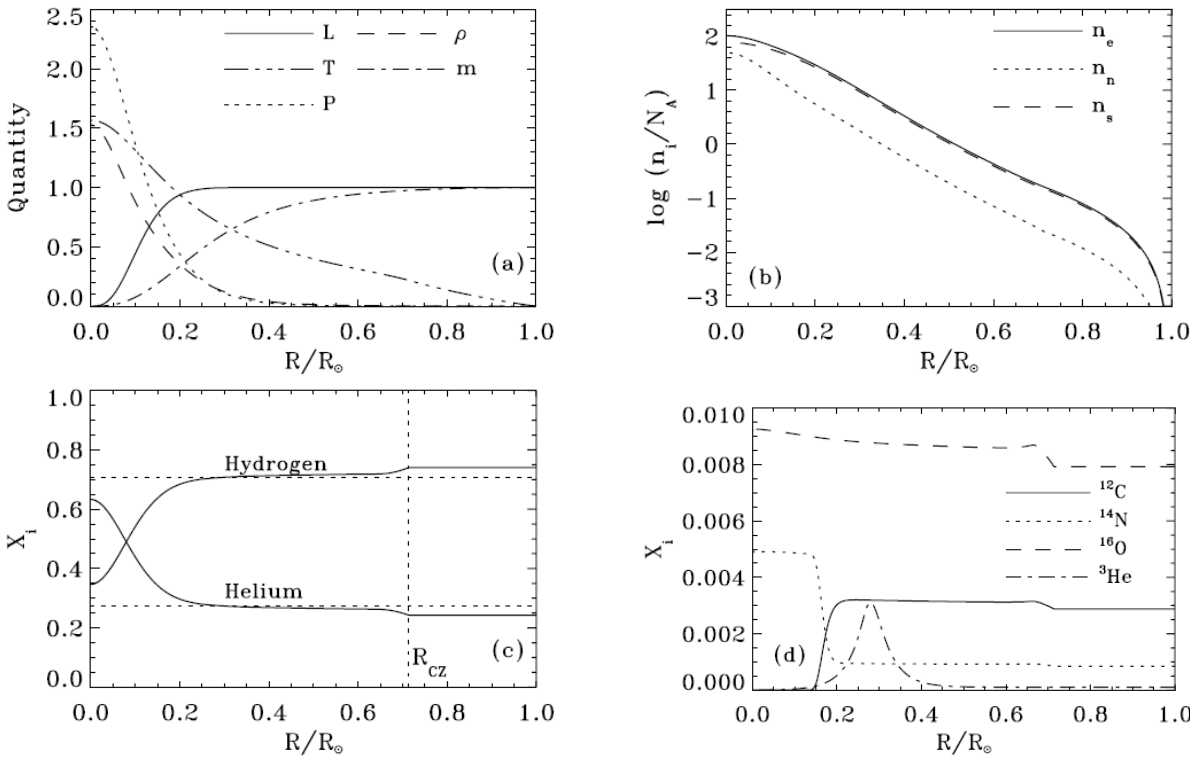

Figure 2.2: Structure of the BS05 SSM. Quantities are given as a function of the distance to the solar center, in units of the solar radius. Panel (a) shows the luminosity L (solar units), temperature T ($10^7 K$), pressure P ($10^{17}\mathrm{g\,cm^{-3}s^{-2}}$), density ρ ($10^2\mathrm{g\,cm^{-3}}$), and enclosed mass m (solar units). Panel (b) shows the logarithm of the number density of electrons (n_e), neutrons (n_n) and sterile neutrino scatterers (n_s) divided by the Avogadro number in units of $\mathrm{cm^{-3}}$. Panel (c) shows the hydrogen and helium mass fraction profiles. Dotted lines denote the initial hydrogen and helium mass fractions. The vertical dotted line denotes the location of the inner boundary of the convective envelope. Panel (d) is the same as panel (c) but for ^{12}C, ^{14}N, ^{16}O, and ^{3}He [33].

Solar Neutrino Fluxes and Solar Neutrino Spectrum

Solar neutrino flux is the prediction of standard solar model while normalized solar neutrino spectrum does not depend on SSM but on Nuclear physics. Predicted total neutrino flux from a particular source depends on total cross section, relative abundance and temperature of reactants. There are eight sources of neutrino flux in the solar core. Table 2.4 gives the total neutrino flux of each source along with energy range of each source. Figure 2.3 show all the neutrino fluxes predicted by BS05(OP) model, as a function of neutrino

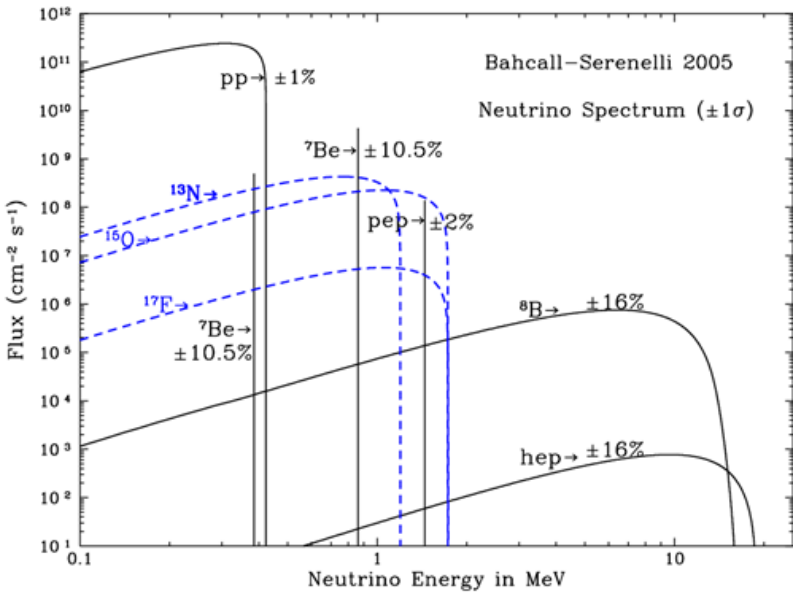

Figure 2.3: Solar neutrino energy spectrum for the SSM BS05(OP).

energy, along with uncertainties calculated by Bahcall and Serenelli (2005) [18].

We note that all neutrino sources, except *pep* and ^7Be that have a line spectrum, have a flux with a range of neutrino energy. The energy range of *hep* flux is maximum that extends up to 18.8 MeV.

Figure 2.4 panels (a) and (b) show the production profile of each neutrino flux defined by $d\phi_i/(dR/dR_\odot)$ that measure the contribution of a shell of thickness $d(R/R_\odot)$ to the

Table 2.4: Solar neutrino fluxes predicted by SSM BS05(OP).

Source	$E_\nu(MeV)$	Flux $(10^{10}cm^{-2}s^{-1})$	Error(%)
pp	$0 \longrightarrow 0.43$	5.99×10^{0}	1.0
pep	1.44	1.42×10^{-2}	1.7
hep	$0 \longrightarrow 18.8$	7.93×10^{-7}	15.5
^7Be	0.86(90%)0.38(10%)	4.84×10^{-1}	10.5
^8B	$0 \longrightarrow 14.06$	5.69×10^{-4}	16.3
^{13}N	$0 \longrightarrow 1.2$	3.07×10^{-2}	$^{+31.2}_{-28.1}$
^{15}O	$0 \longrightarrow 1.7$	2.33×10^{-2}	$^{+33.2}_{-28.8}$
^{17}F	$0 \longrightarrow 1.7$	5.84×10^{-4}	52.2

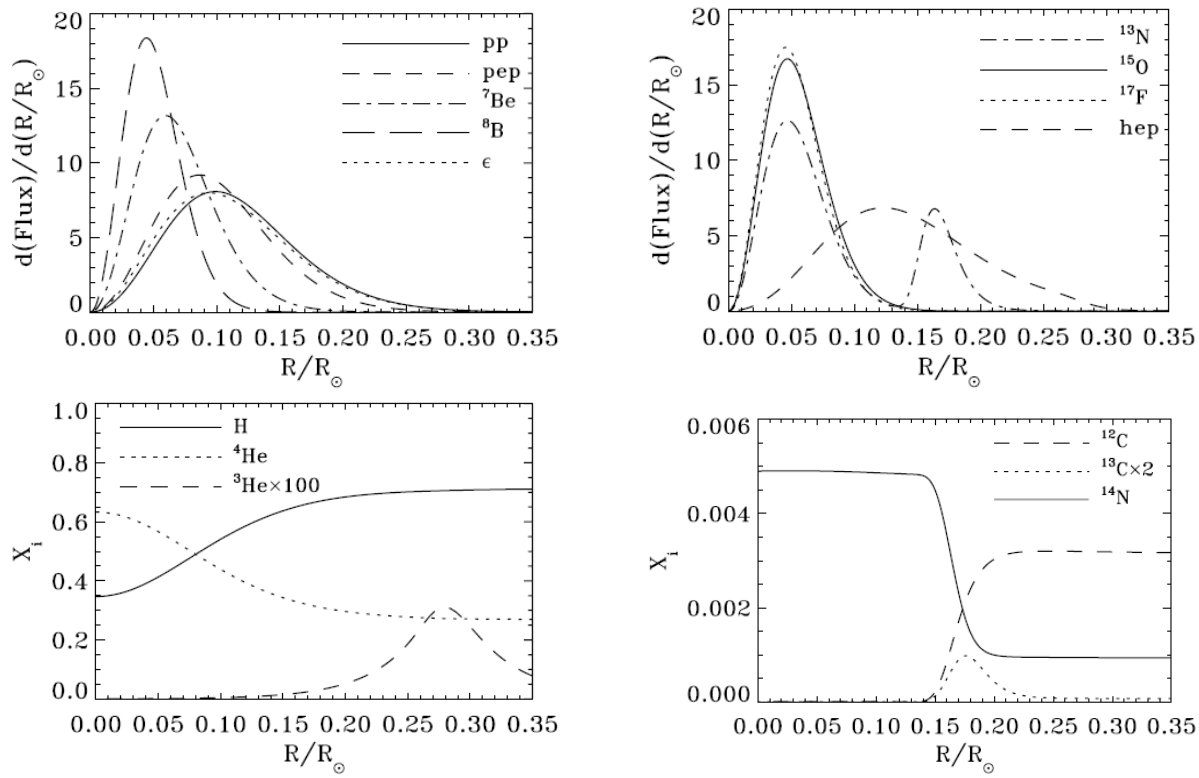

Figure 2.4: Radial Profiles of fluxes and mass fractions. Panels (a) and (b) show the neutrino fluxes as a function of radius. In panel (a) ϵ denotes the production of nuclear energy. All quantities in panels (a) and (b) are normalized. Panels (c) and (d) show the mass fraction of the isotopes most relevant to the production of neutrinos and nuclear energy generation [33].

total production of that neutrino flux. Panels (c) and (d) show the mass fraction of the isotopes most relevant to the production of neutrinos and nuclear energy generation.

2.2.4 Role of Helioseismology

Helioseismology deals with the propagation of acoustic wave oscillations in the Sun. It provides, like terrestrial seismology, information about the interior of the body by using observations of slight motions at its surface. The sound speeds measured by the solar models that include element diffusion agree with helioseismological results of sound speeds to a discrepancy of better than 0.2% throughout the entire sun. In this way helioseismology was able to rule out the possibility that the solar neutrino problem was due to incorrect

models of the interior of the Sun [51].

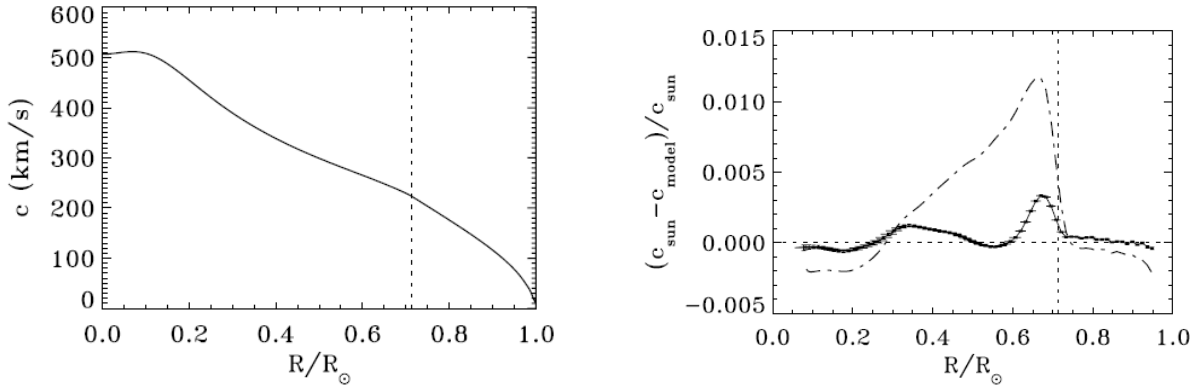

Figure 2.5: Radial profile of sound speed and a relative difference of speeds. Left panel show solar sound speed as a function of the normalized solar radius. Right panel shows the relative difference between the solar (c_{sun}) and the model sound speed (c_{model}) as inferred from helioseismology inversions for the BS05(GS98) (solid line) and BS05(AGS05) (dash-dotted line) models [33].

Figure 2.5 (left panel) shows the sound speed against radius for the BS05 models. The value of c increases inwards with temperature, but in the inner 0.15 $R_{\odot}$ it decreases towards the center due increase in the molecular weight of elements in the core. Figure 2.5 (right panel) shows the relative difference between the solar sound speeds and those determined from helioseismology inversions for the BS05(GS98) and BS05(AGS05) models. The agreement between the solar model and helioseismology measurements is excellent. A detail about the role of helioseismology to cross check the Standard Solar Model results is available in the Ref. [33].

2.3 Solar Neutrino Experiments

Due to very low cross section of neutrinos they have property to escape undisturbed from the sun's core and matter in their way. This makes their detection a challenge. Neutrino detectors are usually built underground to avoid background effects of cosmic rays and radiations from nuclear reactors. They must contain large target mass enough to detect a significant number of neutrinos.

Neutrino detectors can broadly be divided into two categories: *radiochemical experiments* based on neutrino capture by nuclei and *real time detectors* based on neutrino elastic scattering on electrons. The first category, we discuss here briefly, includes Chlorine (Homestake), Gallium (GALLAEX and GNO) and SAGE experiments and second includes Kamiokande, Superkamiokande and SNO experiments.

2.3.1 Chlorine experiment: Homestake

The Homestake was the first solar neutrino experiment, set up by Ray Davis and his collaborators [52], in the period 1965-70, for the measurement of the solar neutrino flux above 0.814 MeV. It continued its operation until 1996. Ray Davis was awarded with Nobel Prize in Physics in 2002 for opening the window of neutrino astronomy.

The experimental facility was located in the gold mine of Homestake in Lead, South Dakota, USA. The target material consisted of 133 *tons* ^{37}Cl dissolved in 613 *tons* of perchloroethylene C_2Cl_4. The tank containing the target material was placed at 4850 ft level underground in the Homestake Gold Mine. A radiochemical technique was used based on inverse beta decay reaction:

$$\nu_{\mathrm{e}} + {}^{37}\mathrm{Cl} \longrightarrow {}^{37}\mathrm{Ar} + \mathrm{e}^{-}, \tag{2.3.1}$$

with a threshold energy of 0.814 MeV that permits all low energy neutrinos except *pp* neutrinos. The number of events were measured by extracting ^{37}Ar produced, at regular intervals, and ^{37}Ar decays were measured in a proportional counter. The predicted event rate of solar neutrinos from theory was $R_{th} = 7.9(1 \pm 0.33)$ SNU[1][37]. The average event rate of about 26 years of data taking by the experiment was $R_{exp} = 2.56 \pm 0.16 \pm 0.16$ SNU [53]. The difference between theory and experiment gave birth to the Solar Neutrino Problem (SNP).

[1] 1 SNU=10^{-36} captures/atom/second

2.3.2 Gallium experiments

The physicists at the Homestake experiment proposed in 1978 an other radiochemical experiment with energy threshold of 233 KeV to detect low energy neutrinos from *pp* neutrino source as well [54]. The experiment was based on the reaction:

$$\nu_{\mathrm{e}} + {}^{71}\mathrm{Ga} \longrightarrow {}^{71}\mathrm{Ge} + \mathrm{e}^{-}, \tag{2.3.2}$$

with energy threshold of 233 KeV. According to the Standard Solar Model, about 54% of the events are due to *pp* neutrinos, whereas 26% and 11% arise from ^{7}Be and ^{8}B neutrinos, respectively. The extraction of ^{71}Ge takes places every 3–4 weeks and the number of ^{71}Ge decays ($t_{1/2}$=11.4 days) is measured in a proportional counter. The experiments involving gallium as target mass are GALLEX, GNO and SAGE described briefly as below.

GALLEX:

Construction of GALLEX (GALLium EXperiment) started in 1988 at Gran Sasso National Laboratory (Italy). The target mass consisted of 30.3 *tons* of gallium in 100.9 *tons* solution of $GaCl_3$ in HCl in a tank. The average event rate provided by the GALLEX experiment [55], during the period of 5 years (1991–97), is given as:

$$R_{exp} = 77.5 \pm 6.2^{+4.3}_{-4.7}\,\mathrm{SNU}. \tag{2.3.3}$$

The expected results from the theory for this experiment was [37]:

$$R_{th} = 132^{+20}_{-17}\,\mathrm{SNU}. \tag{2.3.4}$$

Different independent calibrations [56] have been performed that attested the reliability of the measured rate at the experiment.

GNO:

The GALLEX program was completed in fall 1997 and its successor GNO (Gallium Neutrino Observatory) started taking data in spring 1998. The GNO project was up-gradation

of the GALLEX apparatus with the renewal of its readout electronics. The purpose was to reduce the systematic uncertainty of GALLEX and to monitor the *pp* flux over the 11 year solar cycle.

The project was shut down before schedule due to emergency situation in the Gran Sasso laboratory in April 2003. The final result of the GNO experiment for the period 1998–2003 (58 solar runs) is as below [57]:

$$R_{GNO} = 62.9 \pm 5.4 \pm 2.5\,\text{SNU}. \tag{2.3.5}$$

Combined result with GALLEX (123 solar runs) is:

$$R_{GALLEX+GNO} = 69.3 \pm 4.1 \pm 3.6\,\text{SNU}. \tag{2.3.6}$$

SAGE:

SAGE (Soviet-American Gallium Experiment) [58] is situated at the Baksan Neutrino Observatory in the Caucasus mountains in Russia. Its main difference from the GALLEX and GNO experiments, along with other technical aspects, is its larger target mass ~ 50 *tons* of liquid gallium metal.

The experiment started taking data in 1990 and was planned to work until 2006 but due shutdown of GNO it was continued being the only Gallium experiment. The overall result from 107 solar neutrino runs [59] during January 1990 to March 2003 is $69.1^{+4.3}_{-4.2}(\text{stat})^{+3.8}_{-3.4}(\text{syst})$ SNU that is in agreement with GALLEX+GNO results of Eq.(2.3.6). The result of 168 extractions through December 2007 is $65.4^{+3.1}_{-3.0}(\text{stat})^{+2.6}_{-2.8}(\text{syst})$ SNU whereas the weighted average of the three gallium experiments is 66.1 ± 3.1 SNU [60].

2.3.3 KamiokaNDE and Super-Kamiokande

KamiokaNDE (Kamioka Nucleon Decay Experiment) was the first[2] experiment at the Kamioka Observatory, Institute of Cosmic Ray Research (a neutrino physics laboratory), located underground in the Mozumi mine in Japan. It began its working in 1982 as a

[2]The second experiment at Kamioka Observatory was Super-Kamiokande experiment described below.

nucleon decay experiment. In 1985 it was converted into a neutrino detector. It was the second experiment (after Homestake) to measure solar neutrino fluxes and the first in real time and using Cherenkov light detection. It consisted of a cylindrical tank with 13.1 m height and 14.4 m outer diameter, containing 2142 *tons* of pure water and 948 Photomultiplier Tubes (50 cm diameter) attached to the inner surface [61]. It was operated as neutrino detector from 1987 to 1995 with an energy threshold of 7.5 MeV. The predicted flux consisting of ^{8}B neutrinos was [37]:

$$\Phi_{th} = (5.15^{+0.98}_{-0.72}) \cdot 10^6 \mathrm{cm}^{-2}\mathrm{s}^{-1}. \tag{2.3.7}$$

The observed neutrino flux from 2079 days of data taking is given below that showed a deficit of the neutrino flux verifying the existence of the SNP [62]:

$$\Phi_{exp} = (2.82 \pm 0.19[\mathrm{stat}] \pm 0.33[\mathrm{syst}]) \cdot 10^6 \mathrm{cm}^{-2}\mathrm{s}^{-1}. \tag{2.3.8}$$

Now the physicists started to think about the SNP and the atmospheric neutrino deficit related with the neutrino oscillations.

Super-Kamiokande is the evolution of Kamiokande that was started in April 1996 [63]. Its main purpose was to test the neutrino oscillation hypothesis for solar and atmospheric neutrinos. Like its predecessor Kamiokande it was a real time water cherenkov detector able to detect the neutrinos via elastic scattering (ES) of the neutrinos from the atomic electrons.

$$\nu_a + e^- \longrightarrow \nu_a + e^- \tag{2.3.9}$$

The scattered electrons produce Cherenkov light which is detected by photomultipliers. It consisted of 50,000 tons of pure water surrounded by 11,200 photomultiplier tubes (PMTs) with a cylindrical structure 41.1 m tall and 39.3 m in diameter. The phase-I of the experiment continued from May 1996 to July 2001. The result of the measurement of ^8B neutrinos during this period (1496 days) is given below [64]:

$$\Phi_{SK-I} = (2.35 \pm 0.02[\mathrm{stat}] \pm 0.08[\mathrm{syst}]) \cdot 10^6 \mathrm{cm}^{-2}\mathrm{s}^{-1}, \tag{2.3.10}$$

which is in agreement with Kamiokande result Eq.(2.3.8) along with much lesser uncertainties.

After the completion of phase-I, several PMTs were damaged in an accident, causing implosion of PMTs in a chain, during maintenance operations on November 12, 2001. The survived PMTs were evenly arranged and operation of the detector was restored by adding protective acrylic shells to avoid another such accident.

The data taken after the restoration the detector from December 2002 to the beginning of 2005 is referred to as Phase-II of the Superkamiokande. The measured ^8B flux of the Phase-II is given as below [65]:

$$\Phi_{SK-II} = (2.38 \pm 0.05[\text{stat}]^{+0.98}_{-0.72}[\text{syst}]) \cdot 10^6 \text{cm}^{-2}\text{s}^{-1}, \tag{2.3.11}$$

which is statistically consistent with the results of the Phase-I.

In July 2005, process to restore the detector to its original position was started. Six thousand new PMTs were installed and the process was completed in June 2006. The third phase of Super-Kamiokande (SK-III) involves the period from October 2006 to August 2008 with improved detector calibrations, a full detector simulation, and improved analysis methods. The systematic uncertainty on the total neutrino flux is estimated to be $\pm 2.1\%$, which is about two thirds of the systematic uncertainty for the first phase of Super-Kamiokande. The observed ^8B solar neutrino flux in the total electron energy region of 5.0 to 20 MeV is given as [66]:

$$\Phi_{SK-III} = (2.32 \pm 0.04[stat] \pm 0.05[syst]) \cdot 10^6 cm^{-2} s^{-1}, \tag{2.3.12}$$

which is in agreement with previous measurements.

2.3.4 SNO: The Sudbury Neutrino Observatory

The Sudbury Neutrino Observatory (SNO) [67] is a heavy water Cherenkov detector, located at the Creighton mine near Sudbury in Canada. The detector was designed to

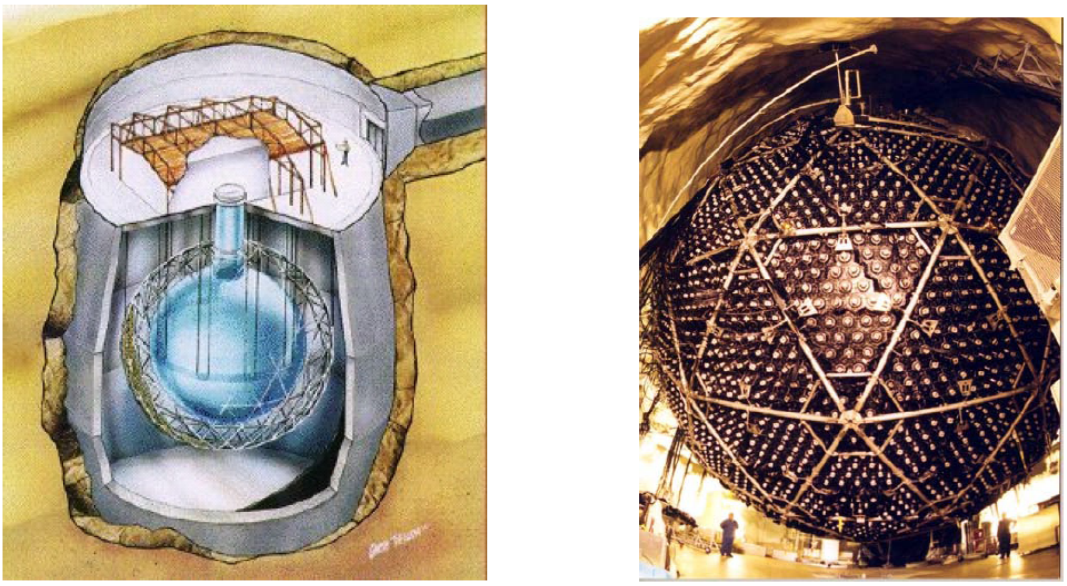

Figure 2.6: Left: Sudbury Neutrino Observatory (SNO). Right: Acrylic vessel with photomultiplier tubes for SNO. Photos courtesy of SNO.

determine weather the currently observed solar neutrino deficit is due to neutrino oscillations. The detector consists of an acrylic vessel, spherical in shape with 6 m radius and containing 1000 *tons* of heavy water (D_2O). The heavy water vessel is inside a 22 m diameter, 34 m high cavity and is surrounded by a 6500 *tons* shield of pure water (Figure 2.6). The heavy water used in the experiment allows detection of neutrino via three types of reactions given below.

Neutral Current, NC: A neutrino dissociates the deuteron breaking it into a neutron and a proton via reaction:

$$\nu_x + d \longrightarrow n + p, \tag{2.3.13}$$

where ν_x refers to any active flavour of neutrino ($\nu_x = \nu_e, \nu_\mu, \nu_\tau$), d is a deuteron nucleus and p is a proton. All three neutrinos can participate in this reaction. The energy threshold for this type of reaction is 2.225 MeV.

Charged Current, CC: A neutrino converts the neutron in a deuteron into a proton; the neutrino is absorbed and an electron is produced that carries energy of the neutrino.

The reaction involved is:

$$\nu_e + d \longrightarrow e^- + p + p, \tag{2.3.14}$$

with energy threshold $T_e > 5MeV$. This reaction is sensitive to electron neutrinos only.

Elastic Scattering, ES: A neutrino collides with an atomic electron and imparts some of its energy to the electron via reaction:

$$\nu_x + e^- \longrightarrow \nu_x + e^-, \tag{2.3.15}$$

with energy threshold $T_e > 5MeV$. This reaction is sensitive to electron neutrino along with small sensitivity with muon and tau neutrino.

First meeting of the SNO collaboration was held in 1984 and its official start was held in 1990 after approval of the funds. The data taking at the SNO started in 1999. The electrons recoiled from ES and CC reactions were detected through their production of Cherenkov light. The energy of the interacting neutrino was measured from the total amount of light detected by the PMT array. The SNO detector operated in three phases depending on how the neutrons from NC interactions were detected [68].

1. **Pure D_2O Phase (November 1999 to May 2001):** In this phase, although the SNO concentrated on the measurement of the CC reaction rate, but also yielded NC measurement by neutron capture on deuterium releasing a single 6.25 MeV γ ray detected as the Cherenkov light.

2. **Salt phase (July 2001 to August 2003):** In 2001 2tons of NaCl have been added to the heavy water to increase the NC sensitivity because ^{35}Cl nuclei have much larger neutron capture cross section than deuterium nuclei. Capture on ^{35}Cl also release more energy (8.6 MeV) that make identification of neutron more efficient.

3. **Neutral Current Detectors (ncds) phase (January 2004 - December 2006):** After the salt removal, an array of ^3He proportional counters or NCD (Neutral Current Detector) Array was deployed in D_2O. The proportional counters were

constructed from high purity nickel tubes welded together to form longer strings. Neutrons were detected via reaction

$$^3He + n \longrightarrow ^3 H + p,$$

producing triton and proton having total kinetic energy of 0.76 MeV and moving in oppsite direction.

The first result of the SNO [69], published in June 2001, consisting of CC and ES measurement of the ^8B flux is given below:

$$\text{Phase} - \text{I} \begin{cases} \phi^{CC}(\nu_e) = 1.75 \pm 0.07[\text{stat}]^{+0.12}_{-0.11}[\text{syst}] \pm 0.05[\text{theor}] \cdot 10^6 \text{cm}^{-2}\text{s}^{-1} \\ \phi^{ES}(\nu_e) = 2.39 \pm 0.34[\text{stat}]^{+0.16}_{-0.14}[\text{syst}] \cdot 10^6 \text{cm}^{-2}\text{s}^{-1} \end{cases} \tag{2.3.16}$$

Here the ES flux was fully compatible with SK results described above and the CC flux was significantly lower.

In the two following years, the historical release of the NC results from Phase-I (April 2002) [3] and from the first part of Phase-II (254 days) (September 2003) [70] showed the strong evidence of the neutrino flavour transformations. The final results of the Phase-II (391 days) [71] of the SNO released in February 2005 are:

$$\text{Phase} - \text{II} \begin{cases} \phi^{CC}(\nu_e) = 1.68 \pm 0.06[\text{stat}] \pm 0.05[\text{syst}] \cdot 10^6 \text{cm}^{-2}\text{s}^{-1} \\ \phi^{ES}(\nu_x) = 2.35 \pm 0.22[\text{stat}] \pm 0.15[\text{syst}] \cdot 10^6 \text{cm}^{-2}\text{s}^{-1} \\ \phi^{NC}(\nu_x) = 4.94 \pm 0.21[\text{stat}] \pm 0.36[\text{syst}] \cdot 10^6 \text{cm}^{-2}\text{s}^{-1} \end{cases} \tag{2.3.17}$$

Here the flux from electron neutrinos is directly given by ϕ^{CC}, whereas the flux from non-ν_e ($\phi_{\mu\tau}$) can be measured by subtracting CC component of the flux from NC and ES fluxes.

$$\phi(\nu, \tau) = \phi^{NC} - \phi^{CC} = 3.26 \pm 0.25[\text{stat}]^{+0.40}_{-0.35}[\text{syst}] \cdot 10^6 \text{cm}^{-2}\text{s}^{-1} \tag{2.3.18}$$

Figure 2.7 shows the flux of non-electron flavour active neutrinos ($\phi_{\mu\tau}$) versus the flux of electron neutrinos (ϕ_e). The nonzero value of $\phi_{\mu\tau}$ shows strong evidence for neutrino flavour transformation. The independent dashed line show ^{8}B solar neutrino flux predicted

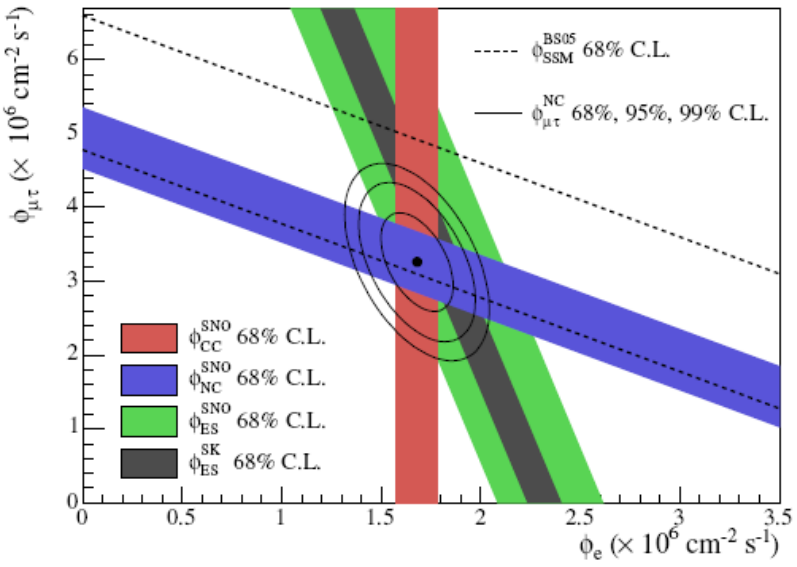

Figure 2.7: SNO Results: flux of muon and tau neutrinos ($\phi_{\mu\tau}$) vs flux of electron neutrinos (ϕ_ν). CC, NC and ES fluxes are given by the filled bands. Dashed lines show SSM predictions. There is a strong evidence for a non-zero $\phi_{\mu\tau}$ [71].

SSM [18]. The neutrino flux measured with NC channel is shown as the solid band parallel to the dashed line of the model prediction. The intercepts of the bands with the axes represent $\pm 1\sigma$ uncertainties. The nonzero value of $\phi_{\mu\tau}$ gives evidence for neutrino flavour transformation. The point shows ϕ_e from CC flux and $\phi_{\mu\tau}$ from NC-CC difference along with 68%, 95%, and 99% C.L. contours.

The results of the SNO phase-III (385.17 days) [72] were presented first time in June 2008. A detailed analysis of the Phase-III data set is provided in the reference [73]. The equivalent neutrino fluxes assuming the ^8B neutrino spectrum from [74], is given as:

$$\text{Phase}-\text{III}\begin{cases}\phi^{CC}(\nu_e) = 1.67^{+0.05}_{-0.04}[\text{stat}]^{+0.07}_{-0.08}[\text{syst}]\cdot 10^6\text{cm}^{-2}\text{s}^{-1}\\ \phi^{ES}(\nu_x) = 1.77^{+0.24}_{-0.21}[\text{stat}]^{+0.09}_{-0.10}[\text{syst}]\cdot 10^6\text{cm}^{-2}\text{s}^{-1}\\ \phi^{NC}(\nu_x) = 5.54^{+0.33}_{-0.31}[\text{stat}]^{+0.36}_{-0.34}[\text{syst}]\cdot 10^6\text{cm}^{-2}\text{s}^{-1}\end{cases} \quad (2.3.19)$$

These results are in agreement with the previous measurements and the Standard Solar Model along with more precision that results in the reduced uncertainty of the mixing angle in the global analysis [72].

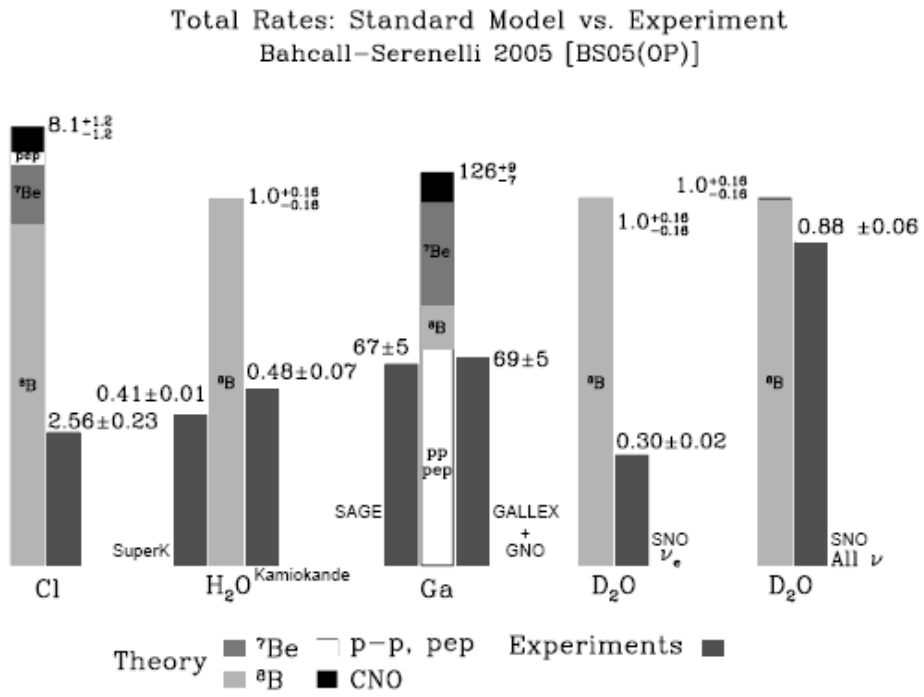

Figure 2.8: Comparison of Experimental Results vs predictions of SSM BS05(OP).

A comparison of different neutrino experiments with the Standard Solar Model results is shown in the figure 2.8. The difference between theory and experiment caused Solar Neutrino Problem, the solution of which was suggested in oscillations of neutrino flavours discussed in the next section.

2.4 Neutrino Oscillations

"Neutrino oscillation is a quantum mechanical interference of different neutrino states. A neutrino created with a specific lepton flavour (electron, muon, or tau) can later be measured to have a different flavour" [75].

Oscillations between different neutrino states can occur if at least one neutrino eigenstate that is coupled to the electron neutrino has a nonzero mass and if the neutrino states that are created in weak interaction decays are not states of definite mass, that is, not

stationary states of free Hamiltonian. The neutrino states, $|\nu_e\rangle$, $|\nu_\mu\rangle$, $|\nu_\tau\rangle$ that are produced in weak interaction-decays in association with particular charged leptons are called **flavour or current eigenstates**. The flavour eigenstates are linear combinations of the **mass eigenstates**, the states that diagonalize the free Hamiltonian.

2.4.1 Two Neutrino Oscillations in Vacuum

Let $|\nu_e\rangle$, $|\nu_\mu\rangle$ be flavour eigen-states of electron and mu neutrino and $|\nu_1\rangle$,$|\nu_2\rangle$ their mass eigenstates. The flavour eigenstates can be written as linear combinations of the mass eigen-states given below:

$$\begin{cases} |\nu_e\rangle = a_{11}|\nu_1\rangle + a_{12}|\nu_2\rangle \\ |\nu_\mu\rangle = a_{21}|\nu_1\rangle + a_{22}|\nu_2\rangle \end{cases} \tag{2.4.1}$$

In matrix form, above equations can be written as:

$$\begin{bmatrix} |\nu_e\rangle \\ |\nu_\mu\rangle \end{bmatrix} = \begin{bmatrix} a_{11} & a_{12} \\ a_{21} & a_{22} \end{bmatrix} \begin{bmatrix} |\nu_1\rangle \\ |\nu_2\rangle \end{bmatrix} \tag{2.4.2}$$

Above equation can also be written as:

$$|\nu_f\rangle \; = \; U_v \; |\nu_m\rangle \tag{2.4.3}$$

where $|\nu_f\rangle = \begin{bmatrix} |\nu_e\rangle \\ |\nu_\mu\rangle \end{bmatrix}$, $U_v = \begin{bmatrix} a_{11} & a_{12} \\ a_{21} & a_{22} \end{bmatrix}$ and $|\nu_m\rangle = \begin{bmatrix} |\nu_1\rangle \\ |\nu_2\rangle \end{bmatrix}$.

To preserve normalizatin (probability), the matrix U_v must be a unitary matrix, that is

$$U_v^\dagger U_v = U_v U_v^\dagger = I. \tag{2.4.4}$$

The U_v matrix can be given as:

$$U_v = \begin{bmatrix} \cos\theta_v & \sin\theta_v \\ -\sin\theta_v & \cos\theta_v \end{bmatrix}, \tag{2.4.5}$$

where θ_v denotes the vacuum mixing angle. Without loss of genreality, we can choose $0 \leq \theta_v \leq \frac{\pi}{4}$ so that ν_e is "mostly" ν_1. So, the Eq. (2.4.2) becomes:

$$\begin{bmatrix} |\nu_e\rangle \\ |\nu_\mu\rangle \end{bmatrix} = \begin{bmatrix} \cos\theta_v & \sin\theta_v \\ -\sin\theta_v & \cos\theta_v \end{bmatrix} \begin{bmatrix} |\nu_1\rangle \\ |\nu_2\rangle \end{bmatrix}, \; 0 \leq \theta_v \leq \frac{\pi}{4}. \tag{2.4.6}$$

Suppose that at some initial time t=0, we have a pure electron neutrino. Equation of state of the electron neutrino can be written as:

$$|\nu_e\rangle_{t=0} = \cos\theta_v|\nu_1\rangle + \sin\theta_v|\nu_2\rangle. \tag{2.4.7}$$

The mass eigenstates $|\nu_1\rangle$ and $|\nu_2\rangle$ may also be energy eigen states which evolve according to Schrodinger Equation by the phase factor e^{-iEt}. So the state of the electron neutrino at time 't' can be given as:

$$|\nu_e\rangle_t = \cos\theta_v e^{-iE_1t}|\nu_1\rangle + \sin\theta_v e^{-iE_2t}|\nu_2\rangle, \tag{2.4.8}$$

where E_1 and E_2 are the energies of two mass eigenstates.
Taking dot product of Eq. (2.4.7) with Eq. (2.4.8), we get:

$${}_0\langle\nu_e|\nu_e\rangle_t = \cos^2\theta_v e^{-iE_1t} + \sin^2\theta_v e^{-iE_2t}. \tag{2.4.9}$$

Taking square modulus of above equation, we can get:

$$|{}_0\langle\nu_e|\nu_e\rangle_t|^2 = 1 - \sin^2 2\theta_v \sin^2\left[\frac{1}{2}(E_2 - E_1)t\right]. \tag{2.4.10}$$

Above equation shows the probability that an electron neutrino remains unchanged, also called electron neutrino's survival probability. The two mass eigenstates are assumed to have same momentum, which implies that they have slightly different energies if they have different masses. The energy difference for relativistic neutrinos is given as:

$$E_2 - E_1 = \frac{E_2^2 - E_1^2}{E_2 + E_1},$$

where $E_2^2 = c^2p^2 + {m_2}^2c^4$ and $E_1^2 = c^2p^2 + {m_1}^2c^4$.
Hence

$$E_2 - E_1 = \pm\frac{(\Delta m^2)c^4}{2E} \tag{2.4.11}$$

where E is the average energy and the appearance of $\pm$ sign reflects the introduction of positive definite quantity Δm^2 given as:

$$\Delta m^2 = |{m_2}^2 - {m_1}^2|. \tag{2.4.12}$$

The plus sign in Eq. (2.4.11) applies when $m_2 > m_1$ and minus sign in opposite case. Using Eqs. (2.4.10) and (2.4.11), we get:

$$|\langle\nu_e|\nu_e\rangle|^2 = 1 - \sin^2 2\theta_v \sin^2\left[\frac{\Delta m^2 c^4 t}{4E}\right].$$

Taking $R = ct$ and using natural units, we can right the above equation as:

$$|\langle\nu_e|\nu_e\rangle|^2 = 1 - \sin^2 2\theta_v \sin^2\left[\frac{\Delta m^2 R}{4E}\right] \tag{2.4.13}$$

or

$$|\langle\nu_e|\nu_e\rangle|^2 = 1 - \sin^2 2\theta_v \sin^2\left[\frac{\pi R}{L_v}\right]. \tag{2.4.14}$$

Here R is the distance traveled in time t and $L_v = \frac{4\pi E}{\Delta m^2}$ is called vacuum oscillation length.

Eq. (2.4.14) shows that the survival probability of electron neutrino depends upon the mixing angle θ_v, squared mass difference Δm^2 and average energy E of the two mass eigenstates. Bringing back $\hbar$ and c vacuum oscillation length, L_v can be written in the form:

$$L_v \equiv \frac{4\pi E\hbar}{\Delta m^2 c^2} = 2.48\left(\frac{E}{\text{MeV}}\right)\left(\frac{\text{eV}^2}{\Delta m^2}\right)\text{m}, \tag{2.4.15}$$

which is often used in discussing terrestrial oscillation experiments that employ beams from reactors or accelerators [36].

2.4.2 Evolution Equations in Vacuum

To study neutrino oscillations in vacuum we need to develop the differential equations which describe the evolution of flavour eigenstates in the vacuum. The flavour eigenstates of neutrino can be written as linear combination of mass eigenstates and vice versa. Using Eq. (2.4.6), we have:

$$\begin{cases} |\nu_e\rangle = \cos\theta_v|\nu_1\rangle + \sin\theta_v|\nu_2\rangle \\ |\nu_\mu\rangle = -\sin\theta_v|\nu_1\rangle + \cos\theta_v|\nu_2\rangle. \end{cases} \tag{2.4.16}$$

An arbitrary neutrino state can be written in the flavour basis as:

$$|\nu(t=0)\rangle = c_e(0)|\nu_e\rangle + c_\mu(0)|\nu_\mu\rangle \tag{2.4.17}$$

where $c_e(0)$ and $c_\mu(0)$ are neutrino amplitudes at $t = 0$. At time t the same state can be given as:

$$|\nu(t)\rangle = c_e(t)|\nu_e\rangle + c_\mu(t)|\nu_\mu\rangle, \tag{2.4.18}$$

where $c_e(t)$ and $c_\mu(t)$ are the probability amplitudes in flavour basis at any time t. The same state can also be written in mass basis as:

$$|\nu(t)\rangle = c_1(t)|\nu_1\rangle + c_2(t)|\nu_2\rangle. \tag{2.4.19}$$

To find the relation between the probability amplitudes in the flavour and mass basis, we use Eq. (2.4.16) in Eq. (2.4.18) to get:

$$|\nu(t)\rangle = c_e(t)[\cos\theta_v|\nu_1\rangle + \sin\theta_v|\nu_2\rangle] + c_\mu(t)[-\sin\theta_v|\nu_1\rangle + \cos\theta_v|\nu_2\rangle]$$

or

$$|\nu(t)\rangle = [c_e(t)\cos\theta_v - c_\mu(t)\sin\theta_v]|\nu_1\rangle + [c_e(t)\sin\theta_v + c_\mu(t)\cos\theta_v]|\nu_2\rangle.$$

Comparing above equation with Eq. (2.4.19), we get:

$$c_1(t) = c_e(t)\cos\theta_v - c_\mu(t)\sin\theta_v$$

and

$$c_2(t) = c_e(t)\sin\theta_v + c_\mu(t)\cos\theta_v.$$

Solving these equations for c_e and c_μ, we get:

$$c_e(t) = c_1(t)\cos\theta_v + c_2(t)\sin\theta_v$$

and

$$c_\mu(t) = -c_1(t)\sin\theta_v + c_2(t)\cos\theta_v$$

In matrix notation, above equations can be written as:

$$\begin{bmatrix} c_e(t) \\ c_\mu(t) \end{bmatrix} = \begin{bmatrix} \cos\theta_v & \sin\theta_v \\ -\sin\theta_v & \cos\theta_v \end{bmatrix} \begin{bmatrix} c_1(t) \\ c_2(t) \end{bmatrix} \tag{2.4.20}$$

or

$$|c_f(t)\rangle \;=\; U_v\,|c_m(t)\rangle, \tag{2.4.21}$$

where $|c_f(t)\rangle = \begin{bmatrix} c_e(t) \\ c_\mu(t) \end{bmatrix}$, $|c_m(t)\rangle = \begin{bmatrix} c_1(t) \\ c_2(t) \end{bmatrix}$ and $U_v = \begin{bmatrix} \cos\theta_v & \sin\theta_v \\ -\sin\theta_v & \cos\theta_v \end{bmatrix}$.

Comparing Eqs. (2.4.6) and (2.4.20), we see that the relation between amplitudes in flavour and mass basis is same as the relation between flavour and mass eigen-states.

Now, consider the general state of neutrino in mass basis, from Eq. (2.4.19):

$$|\nu(t)\rangle = c_1(t)|\nu_1\rangle + c_2(t)|\nu_2\rangle.$$

The mass eigenstates evolve according to the Schrodinger Wave Equation as:

$$i\frac{d}{dt}c_1(t) = E_1c_1(t) \Rightarrow c_1(t) = e^{-iE_1t}c_1(t=0) \tag{2.4.22}$$

and

$$i\frac{d}{dt}c_2(t) = E_2c_2(t) \Rightarrow c_2(t) = e^{-iE_2t}c_2(t=0). \tag{2.4.23}$$

Above equations describe how the amplitude in mass basis change with time. In matrix form, these equations can be written as:

$$i\frac{d}{dt}\begin{bmatrix} c_1(t) \\ c_2(t) \end{bmatrix} = \begin{bmatrix} E_1 & 0 \\ 0 & E_2 \end{bmatrix}\begin{bmatrix} c_1(t) \\ c_2(t) \end{bmatrix}. \tag{2.4.24}$$

Since, subtraction of a number times the unit matrix from the mass matrix only changes the overall state vector by a phase and does not affect probability amplitudes [36], we can write above equation as:

$$i\frac{d}{dt}\begin{bmatrix} c_1(t) \\ c_2(t) \end{bmatrix} = \begin{bmatrix} E_1 - E_2 & 0 \\ 0 & 0 \end{bmatrix}\begin{bmatrix} c_1(t) \\ c_2(t) \end{bmatrix}, \tag{2.4.25}$$

or

$$i\frac{d}{dt}|c_m\rangle = E|c_m\rangle \tag{2.4.26}$$

where

$$|c_m\rangle = \begin{bmatrix} c_1(t) \\ c_2(t) \end{bmatrix}$$

and

$$E = \begin{bmatrix} E_1 - E_2 & 0 \\ 0 & 0 \end{bmatrix}.$$

Now, from equation (2.4.21), we have:

$$|c_m\rangle = U_v^{-1}|c_f\rangle$$

where $|c_f\rangle = \begin{bmatrix} c_e(t) \\ c_\mu(t) \end{bmatrix}$ and $U_v^{-1} = \begin{bmatrix} \cos\theta_v & -\sin\theta_v \\ \sin\theta_v & \cos\theta_v \end{bmatrix}$

Using above relations, Eq. (2.4.26) becomes:

$$i\frac{d}{dt}U_v^{-1}|c_f\rangle = EU_v^{-1}|c_f\rangle.$$

Since for vacuum U_v is independent of time, above equation can be written as:

$$U_v^{-1}i\frac{d}{dt}|c_f\rangle = EU_v^{-1}|c_f\rangle$$

or

$$i\frac{d}{dt}|c_f\rangle = U_vEU_v^{-1}|c_f\rangle. \tag{2.4.27}$$

Written in full this becomes

$$i\frac{d}{dt}\begin{bmatrix} c_e(t) \\ c_\mu(t) \end{bmatrix} = \tag{2.4.28}$$
$$\begin{bmatrix} \cos\theta_v & \sin\theta_v \\ -\sin\theta_v & \cos\theta_v \end{bmatrix}\begin{bmatrix} E_1 - E_2 & 0 \\ 0 & 0 \end{bmatrix}\begin{bmatrix} \cos\theta_v & -\sin\theta_v \\ \sin\theta_v & \cos\theta_v \end{bmatrix}\begin{bmatrix} c_e(t) \\ c_\mu(t) \end{bmatrix}.$$

Simplifying the above equation, we get:

$$i\frac{d}{dt}\begin{bmatrix} c_e(t) \\ c_\mu(t) \end{bmatrix} = \frac{E_1 - E_2}{2}\begin{bmatrix} \cos 2\theta_v & -\sin 2\theta_v \\ \sin 2\theta_v & \cos 2\theta_v \end{bmatrix}\begin{bmatrix} c_e(t) \\ c_\mu(t) \end{bmatrix}. \tag{2.4.29}$$

Putting the value of $E_1 - E_2$ in above equation from Eq. 2.4.11, we get:

$$i\frac{d}{dt}\begin{bmatrix} c_e(t) \\ c_\mu(t) \end{bmatrix} = \pm\frac{\Delta_v}{2}\begin{bmatrix} \cos 2\theta_v & -\sin 2\theta_v \\ \sin 2\theta_v & \cos 2\theta_v \end{bmatrix}\begin{bmatrix} c_e(t) \\ c_\mu(t) \end{bmatrix}, \tag{2.4.30}$$

where $\Delta_v = \frac{\Delta m^2}{2E}$ in natural units. Here, we have plus sign if $m_2 > m_1$ and minus sign otherwise. The above equation describes the evolution of probability amplitudes in the flavour basis.

2.4.3 Neutrino Oscillations in Matter

From Eq. (2.4.30), evolution equation of probability amplitudes in flavour basis for vacuum can be written as:

$$i\frac{d}{dt}\begin{bmatrix} c_e(t) \\ c_\mu(t) \end{bmatrix} = M_\circ \begin{bmatrix} c_e(t) \\ c_\mu(t) \end{bmatrix} \tag{2.4.31}$$

where $M_\circ = \frac{\Delta_v}{2}\begin{bmatrix} -\cos 2\theta_v & \sin 2\theta_v \\ \sin 2\theta_v & \cos 2\theta_v \end{bmatrix}$ and $\Delta_v = \frac{\Delta m^2}{2E}$.

Here $M_\circ$ is the vacuum mass matrix. This equation is valid if the neutrino are evolving in free space. However, if the neutrinos are moving in matter, the matrix M_o should be replaced by the following matrix:

$$M = M_o + M_{matter}, \tag{2.4.32}$$

where M_{matter} is the matrix containing the contribution due to the interaction of electron neutrinos with matter. The form of M_{matter} was derived first by Wolfenstein [76]. It is given as:

$$M_{matter} = \sqrt{2}G_F n_e(t) P_e, \tag{2.4.33}$$

where $P_e = \begin{bmatrix} 1 & 0 \\ 0 & 0 \end{bmatrix}$ is the projection operator for electron neutrinos, n_e is the electron number density and G_F is the Fermi coupling constant.

The new matrix M comes to be:

$$M = \frac{\Delta m^2}{4E}\begin{bmatrix} -\cos 2\theta_v & \sin 2\theta_v \\ \sin 2\theta_v & \cos 2\theta_v \end{bmatrix} + \sqrt{2}G_F n_e(t)\begin{bmatrix} 1 & 0 \\ 0 & 0 \end{bmatrix}$$

or

$$M = \frac{1}{4E}\begin{bmatrix} -\Delta m^2 \cos 2\theta_v + 4\sqrt{2}G_F n_e(t)E & \Delta m^2 \sin 2\theta_v \\ \Delta m^2 \sin 2\theta_v & \Delta m^2 \cos 2\theta_v \end{bmatrix}.$$

Since addition or subtraction of a constant from the diagonal elements does not alter the probability, so subtracting "$2\sqrt{2}G_F n_e(t)E$" from diagonal elements we get:

$$M = \frac{1}{4E}\begin{bmatrix} -\Delta m^2 \cos 2\theta_v + 2\sqrt{2}G_F n_e(t)E & \Delta m^2 \sin 2\theta_v \\ \Delta m^2 \sin 2\theta_v & \Delta m^2 \cos 2\theta_v - 2\sqrt{2}G_F n_e(t)E \end{bmatrix},$$

or

$$M = \frac{1}{4E}\begin{bmatrix} -\Delta m^2 \cos 2\theta_v + A(t) & \Delta m^2 \sin 2\theta_v \\ \Delta m^2 \sin 2\theta_v & \Delta m^2 \cos 2\theta_v - A(t) \end{bmatrix} \tag{2.4.34}$$

where $A(t) = 2\sqrt{2}G_F n_e(t)E$. Here value of $A(t)$ is constant for a specific time. Replacing the matrix M_o by the matrix M, the evolution Eq. (2.4.31) becomes:

$$i\frac{d}{dt}\begin{bmatrix} c_e(t) \\ c_\mu(t) \end{bmatrix} = \frac{1}{4E}\begin{bmatrix} -\Delta m^2 \cos 2\theta_v + A(t) & \Delta m^2 \sin 2\theta_v \\ \Delta m^2 \sin 2\theta_v & \Delta m^2 \cos 2\theta_v - A(t) \end{bmatrix}\begin{bmatrix} c_e(t) \\ c_\mu(t) \end{bmatrix}. \tag{2.4.35}$$

This is standard equation describing the evolution of flavour eigenstates of neutrino in matter. Now we consider neutrino oscillations in matter for the cases of constant and variable density.

Case 1: Constant Density

Consider the two neutrino oscillations in matter of constant density. Using Eq. (2.4.35) the evolution equation in flavour basis in matter can be written as:

$$i\frac{d}{dt}|c_f\rangle = H^m|c_f\rangle, \tag{2.4.36}$$

where

$$H^m = \frac{1}{4E}\begin{bmatrix} -\Delta m^2 \cos 2\theta_v + A(t) & \Delta m^2 \sin 2\theta_v \\ \Delta m^2 \sin 2\theta_v & \Delta m^2 \cos 2\theta_v - A(t) \end{bmatrix} \tag{2.4.37}$$

and

$$|c_f\rangle = \begin{bmatrix} c_e(t) \\ c_\mu(t) \end{bmatrix}.$$

In the case of constant density, the effective Hamiltonian H^m is time independent. In order to solve the equation of motion, we diagonalize the Hamiltonian. Since H^m is real, the unitary transformation to diagonalize it is given as:

$$U^m = \begin{bmatrix} \cos\theta^m & \sin\theta^m \\ -\sin\theta^m & \cos\theta^m \end{bmatrix}. \tag{2.4.38}$$

So,

$$H^m = U^m E^m U^{m\dagger} \tag{2.4.39}$$

where

$$E^m = \begin{bmatrix} E_1^m & 0 \\ 0 & E_2^m \end{bmatrix}.$$

Here E_1^m and E_2^m are eigen values of the matrix H^m and $U^{m\dagger}$ is Hermitian conjugate of U^m.

The eigen value Eq. (2.4.36) can be written as:

$$i\frac{d}{dt}|c_f\rangle = U^m E^m U^{m\dagger}|c_f\rangle. \tag{2.4.40}$$

Operating both sides with $U^{m\dagger}$ where U^m is time independent, we get:

$$i\frac{d}{dt}U^{m\dagger}|c_f\rangle = E^m U^{m\dagger}|c_f\rangle$$

or

$$i\frac{d}{dt}|c_m\rangle = E^m|c_m\rangle \tag{2.4.41}$$

where, $|c_m\rangle = U^{m\dagger}|c_f\rangle$ using Eq. (2.4.21) for matter and $|c_m\rangle = \begin{bmatrix} c_1(t) \\ c_2(t) \end{bmatrix}$.
Here c_1 and c_2 are probability amplitudes of mass eigenstates. Writing in full, Eq. (2.4.41) is

$$i\frac{d}{dt}\begin{bmatrix} c_1(t) \\ c_2(t) \end{bmatrix} = \begin{bmatrix} E_1^m & 0 \\ 0 & E_2^m \end{bmatrix}\begin{bmatrix} c_1(t) \\ c_2(t) \end{bmatrix}. \tag{2.4.42}$$

Now, we find E_1^m and E_2^m, the eigen values of the Hermitian operator H^m, by using the following characteristic equation

$$det(H^m - \lambda I) = 0 \tag{2.4.43}$$

$$\Rightarrow \quad \det\begin{bmatrix} \frac{-\Delta m^2\cos 2\theta_v + A}{4E} - \lambda & \frac{\Delta m^2 \sin 2\theta_v}{4E} \\ \frac{\Delta m^2 \sin 2\theta_v}{4E} & \frac{\Delta m^2\cos 2\theta_v - A}{4E} - \lambda \end{bmatrix} = 0$$

$$\Rightarrow \quad \left(\frac{-\Delta m^2\cos 2\theta_v + A}{4E} - \lambda\right)\left(\frac{\Delta m^2\cos 2\theta_v - A}{4E} - \lambda\right) - \frac{(\Delta m^2 \sin 2\theta_v)^2}{16E^2} = 0$$

$$\Rightarrow \quad -\left(\frac{\Delta m^2\cos 2\theta_v - A}{4E} + \lambda\right)\left(\frac{\Delta m^2\cos 2\theta_v - A}{4E} - \lambda\right) - \frac{(\Delta m^2 \sin 2\theta_v)^2}{16E^2} = 0$$

$$\Rightarrow \qquad \frac{(\Delta m^2 \cos 2\theta_v - A)^2}{16E^2} - \lambda^2 + \frac{(\Delta m^2 \sin 2\theta_v)^2}{16E^2} = 0$$

$$\Rightarrow \qquad \lambda = \pm \frac{1}{4E}\sqrt{(\Delta m^2 \cos 2\theta_v - A)^2 + (\Delta m^2 \sin 2\theta_v)^2}.$$

This expression gives us two possible eigen values of H^m.

$$E_1^m = \frac{1}{4E}\sqrt{(\Delta m^2 \cos 2\theta_v - A)^2 + (\Delta m^2 \sin 2\theta_v)^2} \tag{2.4.44}$$

and

$$E_2^m = -\frac{1}{4E}\sqrt{(\Delta m^2 \cos 2\theta_v - A)^2 + (\Delta m^2 \sin 2\theta_v)^2}. \tag{2.4.45}$$

From above two equations:

$$E_2^m - E_1^m = \frac{1}{2E}\sqrt{(\Delta m^2 \cos 2\theta_v - A)^2 + (\Delta m^2 \sin 2\theta_v)^2} \tag{2.4.46}$$

Now, putting the values of U^m, E^m and $U^{m\dagger}$ in equation (2.4.39), we get:

$$H^m = \begin{bmatrix} E_1^m \cos^2\theta^m + E_2^m \sin^2\theta^m & \frac{E_2^m - E_1^m}{2}\sin 2\theta^m \\ \frac{E_2^m - E_1^m}{2}\sin 2\theta^m & E_1^m \sin^2\theta^m + E_2^m \cos^2\theta^m \end{bmatrix} \tag{2.4.47}$$

Comparing Eqs. (2.4.37) and (2.4.47), and using equation (2.4.46), we get [77]:

$$\sin 2\theta^m = \frac{\Delta m^2 \sin 2\theta_v}{\sqrt{(\Delta m^2 \cos 2\theta_v - A)^2 + (\Delta m^2 \sin 2\theta_v)^2}} \tag{2.4.48}$$

and

$$\cos 2\theta^m = \frac{\Delta m^2 \cos 2\theta_v - A}{\sqrt{(\Delta m^2 \cos 2\theta_v - A)^2 + (\Delta m^2 \sin 2\theta_v)^2}}\ . \tag{2.4.49}$$

Hence

$$\tan 2\theta^m = \frac{\Delta m^2 \sin 2\theta_v}{\Delta m^2 \cos 2\theta_v - A}\ . \tag{2.4.50}$$

Now, we again consider the evolution Eq. (2.4.42) given as:

$$i\frac{d}{dt}\begin{bmatrix} c_1(t) \\ c_2(t) \end{bmatrix} = \begin{bmatrix} E_1^m & 0 \\ 0 & E_2^m \end{bmatrix}\begin{bmatrix} c_1(t) \\ c_2(t) \end{bmatrix}.$$

Since, subtraction of a number times the unit matrix from the mass matrix only changes the overall state vector by a phase and does not affect probability amplitudes [36], we can write the above expression as:

$$i\frac{d}{dt}\begin{bmatrix} c_1(t) \\ c_2(t) \end{bmatrix} = \begin{bmatrix} E_1^m - E_2^m & 0 \\ 0 & 0 \end{bmatrix}\begin{bmatrix} c_1(t) \\ c_2(t) \end{bmatrix} \tag{2.4.51}$$

Now, following the procedure similar to that in deriving Eq. (2.4.29) from Eq. (2.4.25), we can write the evolution Eq. (2.4.51) in flavour basis in matter of constant density as:

$$i\frac{d}{dt}\begin{bmatrix} c_e(t) \\ c_\mu(t) \end{bmatrix} = \frac{E_1^m - E_2^m}{2}\begin{bmatrix} -\cos 2\theta^m & \sin 2\theta^m \\ \sin 2\theta^m & \cos 2\theta^m \end{bmatrix}\begin{bmatrix} c_e(t) \\ c_\mu(t) \end{bmatrix} \tag{2.4.52}$$

This equation is just like the neutrino evolution equation in vacuum except that instead of having vacuum energy and vacuum mixing angle we have matter energy and matter mixing angle. Since $E_1^m - E_2^m = \frac{(\Delta m^2)}{2E}$ following Eq. (2.4.11), above equation becomes:

$$i\frac{d}{dt}\begin{bmatrix} c_e(t) \\ c_\mu(t) \end{bmatrix} = \frac{1}{4E}\begin{bmatrix} -\Delta m^2 \cos 2\theta^m & \Delta m^2 \sin 2\theta^m \\ \Delta m^2 \sin 2\theta^m & \Delta m^2 \cos 2\theta^m \end{bmatrix}\begin{bmatrix} c_e(t) \\ c_\mu(t) \end{bmatrix} \tag{2.4.53}$$

Now comparing Eq. (2.4.53) with Eq. (2.4.35), we get:

$$\Delta m^2 \cos 2\theta^m = \Delta m^2 \cos 2\theta_v + A(t) \tag{2.4.54}$$

and

$$\Delta m^2 \sin 2\theta^m = \Delta m^2 \sin 2\theta_v. \tag{2.4.55}$$

Dividing Eq. (2.4.55) by Eq. (2.4.54), we get:

$$\tan 2\theta^m = \frac{\tan 2\theta_v}{\left[1 \pm \frac{A(t)}{\Delta m^2 \cos 2\theta_v}\right]}.$$

Since $A(t) = 2\sqrt{2}G_F n_e(t)E$, above equation becomes:

$$\tan 2\theta^m = \frac{\tan 2\theta_v}{\left[1 \pm \frac{2\sqrt{2}G_F n_e(t)E}{\Delta m^2 \cos 2\theta_v}\right]}$$

or

$$\tan 2\theta^m = \frac{\tan 2\theta_v}{\left[1 \pm \left(\frac{L_v}{L_e}\right)\sec 2\theta_v\right]}. \tag{2.4.56}$$

Here, the plus sign applies for $m_2 < m_1$ and the minus sign for $m_2 > m_1$. The term L_e is neutrino-electron interaction length [36]. In Eq. (2.4.56):

$$\frac{L_v}{L_e} = \frac{2\sqrt{2}G_F n_e(t)E}{\Delta m^2} \tag{2.4.57}$$

Putting the value of $L_v = \frac{4\pi E}{\Delta m^2}$ from Eq. (2.4.15), using natural units, in above equation, we get:

$$L_e = \frac{\sqrt{2}\pi}{G_F n_e} \tag{2.4.58}$$

We see that the interaction length, L_e is independent of energy, unlike the oscillation length in vacuum or in matter.

Resonance Condition

For $m_2 > m_1$, the expression for mixing angle in matter, using Eq. (2.4.56), is given as:

$$\tan 2\theta^m = \frac{\tan 2\theta_v}{\left[1 - \left(\frac{L_v}{L_e}\right)\sec 2\theta_v\right]}\,. \tag{2.4.59}$$

Eq. (2.4.59) along with Eq. (2.4.57) shows that matter mixing angle depends upon vacuum mixing angle, electron density, squared mass difference of the two neutrinos and average energy of the neutrinos. If the following condition is satisfied, the matter mixing angle becomes maximum and independent of all factors:

$$\left[\frac{L_v}{L_e}\right]_{res} = \cos 2\theta_v. \tag{2.4.60}$$

This is referred to as the *Resonance Condition*. There is no resonance for electron neutrinos if $m_2 < m_1$. Using values of L_v and L_e in Eq. (2.4.60), we get the electron density at which resonance condition is satisfied.

$$n_{e,res} = \frac{|\Delta m^2| \cos 2\theta_v}{2\sqrt{2} G_F E} \tag{2.4.61}$$

or

$$\frac{n_{e,res}}{N_A} \simeq 66 \cos 2\theta_v \left(\frac{|\Delta m^2|}{10^{-4} eV^2}\right)\left(\frac{10 MeV}{E}\right). \tag{2.4.62}$$

Here N_A is the Avogadro's number. The data of the logarithm of "electron density divided by Avogadro's number" versus the radius of the sun, for use in our calculations and analysis, is available at URL:

http://www.sns.ias.edu/∼jnb/SNdata/Export/BS2005/nele_bs05op.dat

The density run shown at the above URL is for the standard solar model, BP05(OP).

Case 2: Variable Density

The electrons density is not constant in the sun. It is maximum in the center of the sun and decreases practically exponentially to its periphery. The consideration of the dependence of n_e on x allowed to discover *possibilities for the large effects of the transitions of solar electron neutrinos into other states in matter* (**MSW Effect**) [77].

The exact solution of the evolution equations is not possible when the electron density is variable. However it is possible to to find analytical solution under some approximations. Or, we can find exact numerical solutions by solving these equations through some numerical techniques. The "Exact Analytical Solution of the Two-Neutrino Evolution Equation in Matter with Exponentially Varying Density" is discussed in [78, 79]. Here we will find an expression for the survival probability of electron neutrino in matter of variable electron density in terms of the parameters Δm^2 and $\sin^2 2\theta$.

Consider the evolution Eq. (2.4.35) in flavour basis. When the Hamiltonian depends upon time 't' or distance 'x', it is given as [80]:

$$i\frac{d}{dt}\begin{bmatrix} c_e(t) \\ c_\mu(t) \end{bmatrix} = \frac{1}{4E}\begin{bmatrix} -\Delta m^2\cos 2\theta_v + A(t) & \Delta m^2 \sin 2\theta_v \\ \Delta m^2 \sin 2\theta_v & \Delta m^2 \cos 2\theta_v - A(t) \end{bmatrix}\begin{bmatrix} c_e(t) \\ c_\mu(t) \end{bmatrix}.$$

This equation can be written as:

$$i\frac{\partial}{\partial t}a(t) = H^m(t)a(t) \tag{2.4.63}$$

where

$$a(t) = \begin{bmatrix} c_e(t) \\ c_\mu(t) \end{bmatrix},$$

$$H^m(t) = \frac{1}{4E}\begin{bmatrix} -\Delta m^2\cos 2\theta_v + A(t) & \Delta m^2 \sin 2\theta_v \\ \Delta m^2 \sin 2\theta_v & \Delta m^2 \cos 2\theta_v - A(t) \end{bmatrix}$$

and

$$A(t) = 2\sqrt{2}G_F n_e(t)E.$$

In order to solve Eq. (2.4.63), we diagonalize $H^m(t)$ by unitary transformation $U^m(t)$, such that:

$$H^m(t) = U^m(t)E^m(t)U^{m\dagger}(t), \tag{2.4.64}$$

where $E^m(t)$ is a diagonal matrix.

Under this unitary transformation, the Eq. (2.4.63) becomes:

$$i\frac{\partial}{\partial t}a(t) = U^m(t)E^m(t)U^{m\dagger}(t)a(t).$$

Operating with $U^{m\dagger}(t)$ from the left, we get:

$$U^{m\dagger}(t)i\frac{\partial a(t)}{\partial t} = E^m(t)U^{m\dagger}(t)a(t) \tag{2.4.65}$$

$$U^{m\dagger}(t)i\frac{\partial a(t)}{\partial t} = E^m(t)a'(t) \tag{2.4.66}$$

where

$$a'(t) = U^{m\dagger}(t)a(t) \tag{2.4.67}$$

$$a(t) = U^m(t)a'(t). \tag{2.4.68}$$

Now, differentiating Eq. (2.4.67) with respect to 't', we get:

$$i\frac{\partial a'(t)}{\partial t} = i\frac{\partial}{\partial t}\left[U^{m\dagger}(t)a(t)\right]$$

$$i\frac{\partial a'(t)}{\partial t} = iU^{m\dagger}(t)\frac{\partial a(t)}{\partial t} + i\frac{\partial U^{m\dagger}(t)}{\partial t}a(t).$$

Since $a(t) = U^m(t)a'(t)$ from Eq. (2.4.68), above equation becomes:

$$i\frac{\partial a'(t)}{\partial t} = iU^{m\dagger}(t)\frac{\partial a(t)}{\partial t} + iU^m(t)\frac{\partial U^{m\dagger}(t)}{\partial t}a'(t)$$

or

$$U^{m\dagger}(t)i\frac{\partial a(t)}{\partial t} = i\frac{\partial a'(t)}{\partial t} - iU^m(t)\frac{\partial U^{m\dagger}(t)}{\partial t}a'(t).$$

Since $U^m(t)U^{m\dagger}(t) = I$, giving $U^m(t)\frac{\partial U^{m\dagger}(t)}{\partial t} = -U^{m\dagger}(t)\frac{\partial U^m(t)}{\partial t}$, the above equation becomes:

$$U^{m\dagger}(t)i\frac{\partial a(t)}{\partial t} = i\frac{\partial a'(t)}{\partial t} + iU^{m\dagger}(t)\frac{\partial U^m(t)}{\partial t}a'(t) \tag{2.4.69}$$

or

$$i\frac{\partial a'(t)}{\partial t} = U^{m\dagger}(t)i\frac{\partial a(t)}{\partial t} - iU^{m\dagger}(t)\frac{\partial U^m(t)}{\partial t}a'(t) \tag{2.4.70}$$

Using Eq. (2.4.66), above equation becomes:

$$i\frac{\partial a'(t)}{\partial t} = E^m(t)a'(t) - iU^{m\dagger}(t)\frac{\partial U^m(t)}{\partial t}a'(t) \tag{2.4.71}$$

or

$$i\frac{\partial a'(t)}{\partial t} = \left[E^m(t) - iU^{m\dagger}(t)\frac{\partial U^m(t)}{\partial t}\right]a'(t) \tag{2.4.72}$$

Adiabatic Approximation

In adiabatic approximation, we assume that the density of electron is slowly varying or we say that it depends weakly on time or distance. In such a case second term in the Eq. (2.4.72) may be neglected and it becomes:

$$i\frac{\partial a'_i(t)}{\partial t} = E^m_i(t)a'_i(t) \tag{2.4.73}$$

Solution of the above equation is given as:

$$a'_i(t) = e^{-i\int_{t_o}^{t} E^m_i(t)dt}a'_i(t_o), \tag{2.4.74}$$

t_o being the initial time.

It follows from the Eqs. (2.4.73) and (2.4.74) that in the adiabatic approximation, a neutrino on the way from the point t_o to the point t remains at the same energy level. From Eqs. (2.4.68) and (2.4.74), we obtain the following solution of the evolution equation in flavour basis:

$$a(t) = U^m(t)e^{-i\int_{t_o}^{t} E^m(t)dt}U^{m\dagger}(t_o)a(t_o). \tag{2.4.75}$$

The amplitude of $\nu_\alpha \to \nu_{\alpha'}$ transition in adiabatic approximation can be given as:

$$\mathcal{A}_{\nu_{\alpha'};\nu_\alpha} = \sum U^m_{\alpha' i}(t)e^{-i\int_{t_\circ}^{t} E^m_i(t)\,dt}U^{m*}_{\alpha i}(t_\circ). \tag{2.4.76}$$

For the case of two flavour neutrinos, we have:

$$U^m(t) = \begin{bmatrix} \cos\theta^m(t) & \sin\theta^m(t) \\ -\sin\theta^m(t) & \cos\theta^m(t) \end{bmatrix}. \tag{2.4.77}$$

To discuss the validity of adiabatic approximation, we consider the second part of Eq. (2.4.72). By taking time derivative of Eq. (2.4.77) and multiplying by $U^{m\dagger}(t)$ from the left, we get:

$$U^{m\dagger}(t)\frac{\partial U^m(t)}{\partial t} = \begin{bmatrix} 0 & \frac{\partial\theta^m(t)}{\partial t} \\ -\frac{\partial\theta^m(t)}{\partial t} & 0 \end{bmatrix}. \tag{2.4.78}$$

Now the equation (2.4.72) becomes:

$$i\frac{\partial}{\partial t}\begin{bmatrix} a_1' \\ a_2' \end{bmatrix} = \begin{bmatrix} E_1^m & -i\frac{\partial\theta^m}{\partial t} \\ i\frac{\partial\theta^m}{\partial t} & E_2^m \end{bmatrix}\begin{bmatrix} a_1' \\ a_2' \end{bmatrix}. \tag{2.4.79}$$

Now using the expressions $E_1^m = \frac{1}{2}(E_1^m + E_2^m) - \frac{1}{2}(E_2^m - E_1^m)$, $E_2^m = \frac{1}{2}(E_1^m + E_2^m) + \frac{1}{2}(E_2^m - E_1^m)$ and $\Delta E^m = E_2^m - E_1^m$, the Hamiltonian in the right hand side of the above equation can be written as:

$$H_m = \frac{1}{2}(E_1^m + E_2^m) + \begin{bmatrix} -\frac{1}{2}\Delta E^m & -i\frac{\partial\theta^m}{\partial t} \\ i\frac{\partial\theta^m}{\partial t} & \frac{1}{2}\Delta E^m \end{bmatrix}. \tag{2.4.80}$$

Here the diagonal elements represent first term of the equation (2.4.72) and the off-diagonal elements represent the second term. So the adiabatic approximation is valid if the following condition is satisfied:

$$\left|\frac{\partial\theta^m}{\partial t}\right| \ll \frac{1}{2}\Delta E^m. \tag{2.4.81}$$

Now using Eq. (2.4.50) and $A(t) = 2\sqrt{2}G_F n_e(t)E$ we get:

$$\left|\frac{\partial\theta^m}{\partial t}\right| = \frac{\Delta m^2 \sin 2\theta_v \sqrt{2}G_F E\left|\frac{\partial n_e(t)}{\partial t}\right|}{(\Delta m^2\cos 2\theta_v - A(t))^2 + (\Delta m^2 \sin 2\theta_v)^2}. \tag{2.4.82}$$

Using Eqs. (2.4.46) and (2.4.82) in Eq. (2.4.81) we get:

$$4\sqrt{2}G_F E^2 \Delta m^2 \sin 2\theta_v \left|\frac{\partial n_e(t)}{\partial t}\right| \ll \left[(\Delta m^2\cos 2\theta_v - A(t))^2 + (\Delta m^2 \sin 2\theta_v)^2\right]^{3/2}. \tag{2.4.83}$$

If the resonance condition

$$\Delta m^2 \cos 2\theta_v = A(t_R) \tag{2.4.84}$$

is satisfied at the point $t = t_R$, the ***condition of validity of adiabatic approximation*** can be written as:

$$4\sqrt{2}G_F E^2 \Delta m^2 \sin 2\theta_v \left|\frac{\partial n_e(t_R)}{\partial t}\right| \ll (\Delta m^2 \sin 2\theta_v)^3 \tag{2.4.85}$$

or

$$\frac{2E\ 2\sqrt{2}G_F E n_e(t_R)\frac{1}{n_e(t_R)}\left|\frac{\partial n_e(t_R)}{\partial t}\right|}{(\Delta m^2)^2\sin^2 2\theta_v} \ll 1 \tag{2.4.86}$$

or

$$\frac{2EA(t_R)\left|\frac{\partial}{\partial t}\ln n_e(t_R)\right|}{(\Delta m^2)^2\sin^2 2\theta_v} \ll 1 \tag{2.4.87}$$

or

$$\frac{2E\Delta m^2\cos 2\theta_v\left|\frac{\partial}{\partial t}\ln n_e(t_R)\right|}{(\Delta m^2)^2\sin^2 2\theta_v} \ll 1 \tag{2.4.88}$$

or

$$\frac{2E\cos 2\theta_v\left|\frac{\partial}{\partial t}\ln n_e(t_R)\right|}{\Delta m^2\sin^2 2\theta_v} \ll 1. \tag{2.4.89}$$

Now modulus square of the Eq. (2.4.76) gives the following probability for the $\nu_\alpha \to \nu_{\alpha'}$ transition in the *adiabatic approximation*:

$$\begin{aligned} P(\nu_\alpha \to \nu_{\alpha'}) \quad &= \sum_i |U^m_{\alpha' i}(t)|^2 |U^m_{\alpha i}(t_\circ)|^2 \\ &+2Re\sum_{i<k} U^m_{\alpha' i}(t) {U^m_{\alpha' k}}^* e^{-i\int_{t_\circ}^t (E^m_i - E^m_k)\,dt} U^{m*}_{\alpha i}(t_\circ) U^m_{\alpha k}(t_\circ)\,. \end{aligned} \tag{2.4.90}$$

For solar neutrinos the second term in the r.h.s. of this expression disappears due to averaging over the energy and the region in which neutrinos are produced. Hence for the averaged transition probability we have:

$$\overline{P}(\nu_\alpha \to \nu_{\alpha'}) = \sum_i |U^m_{\alpha' i}(t)|^2 |U^m_{\alpha i}(t_\circ)|^2. \tag{2.4.91}$$

Thus, in the *adiabatic approximation*, the averaged transition probability is determined by the elements of the mixing matrix in matter at the initial and final points [80]. For the case of two neutrino flavours, using expression for U^m in the Eq. (2.4.38), we have the following simple expression for the ν_e survival probability:

$$\begin{aligned} \overline{P}(\nu_e \to \nu_e) \quad &= \cos^2\theta^m(t)\cos^2\theta^m(t_\circ) + \sin^2\theta^m(t)\sin^2\theta^m(t_\circ) \\ &= \frac{1}{2}\left[1 + \cos 2\theta^m(t)\cos 2\theta^m(t_\circ)\right], \end{aligned} \tag{2.4.92}$$

where $\cos 2\theta^m(t)$ is given by the Eq. (2.4.49). The above equation shows that the average survival probability depends only on the values of matter mixing angles at initial and final

point. It also shows, along with Eq (2.4.49) and (2.4.84), that if the neutrino passes the point $t = t_R$ where the resonance condition is satisfied, a large effect of disappearance of ν_e will be observed. For solar neutrino, the final point is always the one at which density of electron is always almost zero. At zero or low electron density, matter mixing angle is equal to vacuum mixing angle and hence, the factor $\cos\theta^m(t)$ can be replaced by $\cos\theta_v$. Hence:

$$\overline{P}(\nu_e \to \nu_e) = \frac{1}{2}\left[1 + \cos 2\theta_v(t)\cos 2\theta^m(t_\circ)\right]. \tag{2.4.93}$$

Now resonance condition in the Eq. (2.4.93) is fulfilled if $\cos 2\theta_v > 0$. At the production point $t_\circ$ the density is larger than at point t_R and $A(t_\circ) > \Delta m^2 \cos 2\theta_v$. From the Eq. (2.4.49), it follows that $\cos 2\theta^m(t_\circ) < 0$. Thus, if the resonance condition is fulfilled, we see from Eq. (2.4.93) that $P(\nu_e \to \nu_e) < \frac{1}{2}$.

If the condition $A(t_\circ) \gg \Delta m^2$ is satisfied for neutrinos produced in the center of the Sun, then $\cos 2\theta^m(t_\circ) \simeq -1$ and, for neutrinos passing through the Sun, the survival probability is:

$$\overline{P}(\nu_e \to \nu_e) = \frac{1}{2}\left[1 - \cos 2\theta_v\right]. \tag{2.4.94}$$

It is obvious from this expression that the ν_e survival probability at small θ_v is close to zero: all ν_e's are transformed into ν_μ's [80].

The Eq. (2.4.91) gives the averaged survival probability in the adiabatic approximation. In the general case we have:

$$\overline{P}(\nu_\alpha \to \nu_{\alpha'}) = \sum_i |U^m_{\alpha' i}(t)|^2 P_{ik} |U^m_{\alpha k}(t_\circ)|^2 \tag{2.4.95}$$

where P_{ik} is the probability of transition from the state with energy E^m_k to the state with energy E^m_i. Let us consider the simplest case of transition between two types of neutrinos. From the conservation of the total probability we have:

$$P_{11} = 1 - P_{21}\,, \qquad P_{22} = 1 - P_{12}\,, \qquad P_{12} = P_{21} \tag{2.4.96}$$

Thus in the case of two neutrinos all transition probabilities P_{ik} are expressed through P_{12}. With the help of Eqs. (2.4.38), (2.4.95) and (2.4.96), for the ν_e survival probability

we have [80]:

$$\overline{P}(\nu_e \to \nu_e) = \frac{1}{2} + \left(\frac{1}{2} - P_{12}\right) \cos 2\theta^m(t) \cos 2\theta^m(t_\circ). \tag{2.4.97}$$

At zero or low electron density, we replace matter mixing angle θ^m with vacuum mixing angle, say θ instead of θ_v for simplicity. The above expression becomes:

$$\overline{P}(\nu_e \to \nu_e) = \frac{1}{2} + \left(\frac{1}{2} - P_{12}\right) \cos 2\theta \cos 2\theta^m. \tag{2.4.98}$$

In the literature there exist different approximate expressions for the transition probability P_{12}. In the Landau-Zener approximation, based on the assumption that the transition occurs mainly in the resonance region,

$$\mathrm{P}_{12} = \frac{\exp[-\gamma \sin^2\theta] - \exp[-\gamma]}{1 - \exp[-\gamma]}, \tag{2.4.99}$$

where

$$\gamma = \pi \frac{\Delta m^2}{E} \left[\left|\frac{d \ln n_e(r)}{dr}\right|_{r=r_{res}}\right]^{-1}. \tag{2.4.100}$$

Here $n_e(r)$ is the radial electron density in the sun and the value $n_{e,res}$ at resonance point is given by the expression in Eq. (2.4.61). The adiabatic approximation is valid if $\gamma \gg 1$. In this case $P_{12} \simeq 0$ [80].

From Eqs. (2.4.97), (2.4.99) and (2.4.100), we see that transition probabilities from one flavour state of neutrino to another can be measured by the parameters Δm^2 and $\sin^2 2\theta$.

Chapter 3

Global Analysis of the Solar Neutrino Data using Grid-based Method

We have discussed in the previous chapter that solution of the solar neutrino problem lies in the neutrino oscillations. The exact amount of the depletion of the solar neutrinos caused by the neutrino oscillations depends on the neutrino's squared mass difference $\Delta m^2 \equiv m_2^2 - m_1^2$ and the mixing angle θ. In the global analysis of the solar neutrino data, we fix the values of these parameters so that the difference between the theoretically calculated values of the observable (event rates) and measured values is minimum.

It is noted that there are always experimental and theoretical uncertainties in the experimental data and theoretically calculated values respectively. In the presence of these uncertainties it is not possible to make an exact comparison between theory and experiment. However, if we appropriately count the uncertainties in this comparison, it is possible to find out the points in parametric space of squared mass difference and mixing angle ($10^{-4} \leq \tan^2\theta \leq 10$, $10^{-13}\text{eV}^2 \leq \Delta m^2 \leq 10^{-3}\text{eV}^2$), where the difference between calculated and measured values of the observable is minimum. When such an analysis is completed we obtain many local minima, which mean many possible solutions. These solutions, as described in the introduction (chapter 1), are named vacuum oscillations (VO), MSW with Small Mixing Angle (SMA), MSW with Large Mixing Angle (LMA) and

MSW at low Δm^2 (LOW). These solutions are presented by local minima in $\Delta m^2 - \tan^2\theta$ plane contoured by iso $-\ \chi^2$ curves. These minima have different goodness-of-fit (g.o.f)[1]. The solution with maximum g.o.f is regarded as the most probable or the best solution.

In this chapter we cover the details of the Global Analysis, completed in this work. The global analysis is accomplished by the calculation of χ^2 function, described below by Eq. (3.4.1), for different values of the oscillation parameters Δm^2 and $\tan^2\theta$. In section 3.1 we describe the experimental data we used. Calculation of the survival probabilities of ν_e for different values of the parameters is discussed in section 3.2. The calculation of the theoretical event rates is given in section 3.3. The error matrix and χ^2 function calculation is described in section 3.4 and the results of global analysis are given in section 3.5.

3.1 Experimental Data used in our Analysis

In our χ^2 analysis, we used the updated data of total event rates of different solar neutrino experiments. We included chlorine (Homestake), weighted average of Gallax and GNO, SAGE, Superkamiokande, SNO CC and SNO NC total rates. The experimental data used in our analysis is shown in Table 3.1. The theory values in column 3 are taken from the SSM BS05(OP) [18].

Table 3.1: Solar Neutrino Data used in our analysis. The results of Homestake, GALLAX+GNO and SAGE are given in the units of SNU (1 SNU=10^{-36} captures/atom/second) whereas others are in units of $10^6\text{cm}^{-2}\text{s}^{-1}$.

Experiment	Result	Theory	Result/Theory	Ref.
Homestake	$2.56 \pm 0.16(\text{stat}) \pm 0.16(\text{syst})$	$7.6^{+1.3}_{-1.1}$	0.33 ± 0.02	[53]
GALLAX+GNO	69.3 ± 5.5	128^{+9}_{-7}	0.54 ± 0.05	[57]
SAGE	$65.4^{+3.1}_{-3.0}(\text{stat})^{+2.6}_{-2.8}(\text{sys})$	128^{+9}_{-7}	0.51 ± 0.04	[60]
Superkamiokande	$2.32 \pm 0.04(\text{stat}) \pm 0.05(\text{syst})$	$5.69(1 \pm 0.23)$	0.41 ± 0.02	[66]
SNO CC	$1.67^{+0.05}_{-0.04}(\text{stat})^{+0.07}_{-0.08}(\text{syst})$	$5.69(1 \pm 0.23)$	0.29 ± 0.02	[72]
SNO NC	$5.54^{+0.33}_{-0.31}(\text{stat})^{+036}_{-0.34}(\text{syst})$	$5.69(1 \pm 0.23)$	0.97 ± 0.09	[72]

[1] A description of goodness-of-fit is given in the chapter 1.

3.2 Calculation of the Average Survival Probability

Here we discuss the calculation of the year average survival probability $\langle P_{ee}^{k}(E_\nu)\rangle$ for k^{th} neutrino source and for the grid of 101 $\times$ 101 values of $\frac{\Delta m^2}{E}$ (E is neutrino energy in MeV) and $\tan^2\theta$ at different detector locations, used for the calculation of the theoretical event rates in the Eq. (3.4.2) below. For the uniform grid interval distribution, the parameters $\frac{\Delta m^2}{E}$ and $\tan^2\theta$ can be taken exponential functions of variables x_1 and x_2 as:

$$\frac{\Delta m^2}{E} = 10^{(0.1x_1-13)} \tag{3.2.1}$$

and

$$\tan^2\theta = 10^{-2(2-0.025x_2)}, \tag{3.2.2}$$

so that discrete values of x_1 and x_2 from 0 to 100 cover the entire $\tan^2\theta - \Delta m^2$ parameter space.

For the calculation of the average survival amplitude (two neutrino case) of ν_e of energy E_ν from source region in the sun to the detector in the earth, we begin with the general expression:

$$A_{ee} = \sum_{i=1}^{2} A_{ei}^{S} A_{ie}^{E} \texttt{exp}[-im_i^2(L-r)/2E]. \tag{3.2.3}$$

Here, A_{ei}^{S} is the transition amplitude of $\nu_e \to \nu_i$ (ν_i is the i^{th} mass eigenstate) from the production point to the Sun surface, A_{ie}^{E} is the transition amplitude of $\nu_i \to \nu_e$ from the Earth surface to the detector, the exponential part shows the propagation in vacuum from the Sun to the surface of the Earth, L is the distance between the center of the Sun and the surface of the Earth, r is the distance between the neutrino production point and the surface of the Sun [7]. The expression for the survival probability P_{ee}[2] can be given as:

$$P_{ee} = P_1P_{1e} + P_2P_{2e} + 2\sqrt{P_1P_2P_{1e}P_{2e}}\cos\zeta \tag{3.2.4}$$

Here $P_i \equiv |A_{ei}^{S}|^2$ is the probability that the solar neutrinos reach the surface of the Sun as $|\nu_i\rangle$, $P_{ie} \equiv |A_{ie}^{E}|^2$ is the probability of ν_i arriving at the surface of the Earth to be detected

[2]Proof of the expression is given in Appendix A.1.

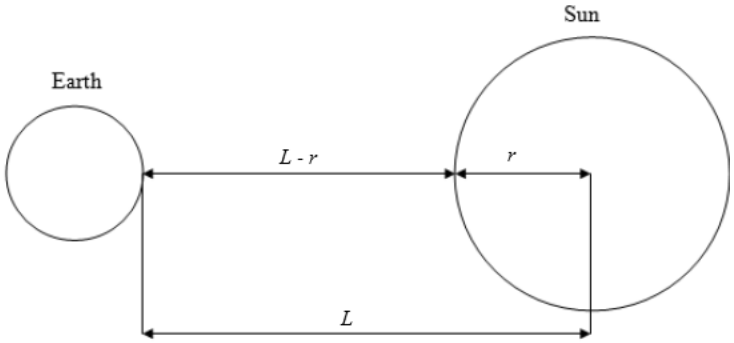

Figure 3.1: Illustration of the parameters L and r. L is the distance from center of the sun to the surface of the earth. r is distance from production point of the neutrino to the surface of the sun.

as a ν_e. Unitarity implies $P_1 + P_2 = 1$ and $P_{1e} + P_{2e} = 1$. The phase ζ is given by:

$$\zeta = \frac{\Delta m^2 (L - r)}{2E} + \delta$$

δ is sum of the relative phases of the transition amplitudes described in Appendix A.1. This phase can always be neglected for calculating average survival probability [81, 82].

3.2.1 Analytical Solution

The analytical expression, described below Eq. (3.2.5) and discussed in the section 2.4.3, to find survival probability at the the earth surface is based on the Landau-Zenner approximation based on the assumption that most of the transitions between different mass or energy eigen states occur at resonance. For most of the region in the parametric space of Δm^2 and $\tan^2\theta$ this approximation is valid to reasonably good extent. However, there are certain region where this approximation is not valid and the difference between the values obtained by the analytical expressions and exact may precipitate. So in these regions we cannot use these analytical expressions. To find out the exact values of survival probability in these regions we have to solve the evolution equation in the sun through numerical techniques discussed in the section 3.2.2. For the selection of numerical or analytical solution, for different points in the parameter space, we followed the prescriptions

given by the refs. [7, 9, 83].

For $\frac{\Delta m^2}{E} > 0.33 \times 10^{-6}\text{eV}^2/\text{MeV}$ and all angles (including $\theta > \pi/4$), we used the analytical expression (also described in Eq. (2.4.98)) to find day time survival probability at the earth surface P_S given as:

$$P_S(\nu_e) = \frac{1}{2} + \left(\frac{1}{2} - P_{12}\right) \cos 2\theta^m \cos 2\theta. \tag{3.2.5}$$

Here $\cos 2\theta^m$ is defined in the Eq. (2.4.49) and P_{12} is the transition probability based on the Landau-Zener approximation given in the Eq. (2.4.99). We averaged the survival probabilities over the relevant neutrino production region for each neutrino flux given in the SSM BS05(OP) [18]. Assuming the neutrinos arriving the earth represent an incoherent superposition of mass eigen states, we use the following expression for the calculation of the average survival probability of electron neutrino, after passing through the earth, at the detector[3]:

$$P_{SE}(\nu_e) = P_S(\nu_e) + \frac{[2P_S(\nu_e) - 1][\sin^2\theta - P_{2e}]}{\cos 2\theta}, \tag{3.2.6}$$

where P_{2e} is the probability of the transition from the mass eigen-state ν_2 to ν_e along the neutrino path in the earth. Calculation if the probability P_{2e} is discussed in the section 3.2.4 below. The only difference between $P_{SE}(\nu_e)$, Eq. (3.2.6) and P_{ee}, Eq. (3.2.4) is that of phase term which is neglected in the Eq. (3.2.6).

3.2.2 Numerical Solution

For $\frac{\Delta m^2}{E} < 0.33 \times 10^{-6}\text{eV}^2/\text{MeV}$, to calculate day time survival probability at the earth surface, we first solved Eq. (2.4.35), the standard equation describing the evolution of flavour eigenstates of neutrino in matter, numerically from the source region in the sun to the surface of the sun and calculated P_1 and P_2 $(= 1 - P_1)$. We used the following expression for the day time survival probability at the earth surface[4]:

$$P_e = P_1 \cos^2\theta + P_2 \sin^2\theta + \sqrt{P_1 P_2} \sin 2\theta \cos \xi, \tag{3.2.7}$$

[3]Proof of the expression is given in Appendix A.2.

[4]The detail of the expression is given in the Appendix A.3.

where phase $\xi = \frac{\Delta m^2(\mathrm{L-r})}{2E} + \epsilon$.

For the night time survival probability at the detector, we calculated P_{1e} and P_{2e} by numerically solving the evolution equations through the earth surface and used the full expression given by the Eq. (3.2.4). Here we average P_1 and P_2 over production points in the sun, P_{1e} and P_{2e} over trajectories (zenith angles described below) in the earth and $\cos\zeta$ over production points in the sun and over the earth sun distance, all for each of the eight neutrino sources. For the production point average of the probabilities we have used the expression:

$$\langle P_1 \rangle_i = \int_{r_\circ}^{r_f} \phi_i(r) P_1 dr, \tag{3.2.8}$$

where $\phi_i(r)$ is the fraction of i^{th} source of neutrino at the point r that varies from $r_\circ$ to r_f in the units of solar radius. The data of $\phi_i(r)$ is taken from the URL: http://www.sns.ias.edu/ jnb/SNdata/sndata.html#bs2005.

3.2.3 Transition through the Earth and Regeneration Effect

During day-time, the neutrinos arriving at Earth are mostly ν_μ (or ν_τ) with some admixture of ν_e. At night-time, neutrinos have to pass through the earth in order to reach the detector. As a result of passing through the earth, the fraction of ν_e increases because of the conversion of ν_μ (or ν_τ) into ν_e by neutrino oscillations. The process of increasing the fraction of electron neutrinos ν_e after passing through the earth is called the "regeneration effect" and has the opposite effect to the conversion of ν_e to ν_μ (or ν_τ) in the sun. Due to the change of neutrino type in the earth, the MSW mechanism predicts that solar neutrino detectors should measure higher event rates at night than during daytime [83].

Figure 3.2 shows a schematic view of a solar neutrino detector at the geographic latitude ϕ. Since the earth is spherically symmetric to $O(10^{-2.5})$, it is enough to consider the cross-section slice shown in the figure. Two lines determine the geometry: one line defines the zenith direction at the detector, and the other line shows the trajectory of the neutrino. The zenith angle α ($0^\circ < \alpha < 180^\circ$) between these two lines specifies the

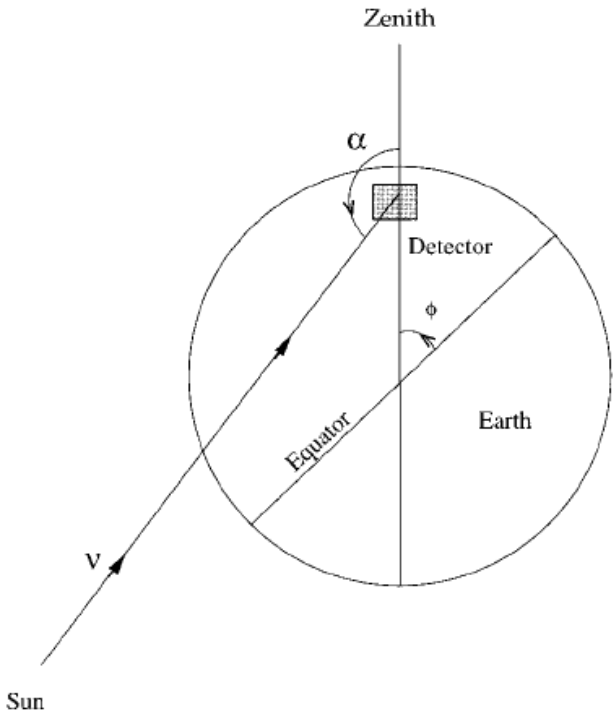

Figure 3.2: Diagram showing a solar neutrino detector at geographic latitude ϕ [83].

neutrino trajectory in the earth. Therefore, production point averaged survival probability depends on the path (i.e, α) the neutrino travels through the earth along with the neutrino oscillations parameters Δm^2 and $\tan^2\theta$ and the neutrino energy E. Due to the apparent motion of the sun, the neutrino survival probability should change with time as well, resulting in an asymmetric distortion of the angular distribution of events [83].

The probability P_{2e} is calculated as a function of Δm^2 and $\tan^2\theta$ for night zenith angles. We have chosen a set of 180 trajectories equally spaced between 90° and 180° of zenith angle. This set is the same for all solar neutrino detectors since the density profiles in the earth are spherically symmetric. In each trajectory P_{2e} is calculated for a grid of 101×101 values of Δm^2 and $\tan^2\theta$.

The one-year average survival probability for i^{th} neutrino source is given by the expression:

$$\langle P_{ee,i} \rangle = \sum_{n=0}^{180} P^n_{ee,i} Y(\alpha_n). \tag{3.2.9}$$

Here α_n are the zenith angles separated by 0.5° interval between 0° and 180° and $Y(\alpha_n)$ is the zenith angle exposure function that defines the relative amount of time the detector is exposed to the sun at a fixed zenith angle α_n during the year. We followed the ref. [83] for the calculation of the $Y(\alpha_n)$ in our case.

The one-year averaged night-time survival probability is given by the expression:

$$\langle P_{ee,i}^{NIGHT} \rangle = \sum_{n=90}^{180} P_{ee,i}^{n} Y(\alpha_n). \tag{3.2.10}$$

Since the night-time and day-time intervals during the year are equal, the day-time average probability is given as:

$$\langle P_{ee,i}^{DAY} \rangle = 0.5 \langle P_{ee,i} \rangle. \tag{3.2.11}$$

Using the probabilities calculated this way we found the day-time and night-time event rates at the detector location as described below.

3.2.4 Calculation of P_{2e}

Here we discuss probability P_{2e} of ν_2 mass eigen-state at the surface of the earth to be detected as ν_e at the detector location after traversing its path through the earth. For this purpose we solved the Eq. (2.4.35), the standard equation describing the evolution of flavour eigenstates of neutrino in matter, using earth's density profile. We have used PREM (Preliminary Reference Earth Model) of Dziewonski and Anderson [84] for the earth density distribution.

The interior of the earth is divided into eight shells in the PREM model, but for the neutrino trajectories through the earth the four outer shells can be grouped into a single shell "upper mantle". The density profile $N(r)$ for the interior of earth is given in detail in Table I of ref. [84]. This density profile for different shells is shown in the figure 3.3. The density changes abruptly between the inner and outer core and also at the border between the lower mantle and the outer core. The authors in ref. [85] have parameterized this density profile. For each shell they use a polynomial fit given as:

$$N_j(r) = \alpha_j + \beta_j r^2 + \gamma_j r^4, \tag{3.2.12}$$

Table 3.2: Coefficients of the electron density parametrization $N_j(r) = \alpha_j + \beta_j r^2 + \gamma_j r^4$, $[N]$ = mol/cm^3, for j_{th} shell range $[r_{j-1}, r_j]$. The radial distance r is normalized to the Earth radius [85].

j	Shell	$[r_{j-1}, r_j]$	α_j	β_j	γ_j
1	Inner Core	[0, 0.192]	6.099	-4.119	0.000
2	Outer Core	[0.192, 0.546]	5.803	-3.653	-1.086
3	Lower mantle	[0.546, 0.895]	3.156	-1.459	0.280
4	Transition zone	[0.895, 0.937]	-5.376	19.210	-12.520
5	Upper Mantle	[0.937, 1]	11.540	-20.280	10.410

where the coefficient α_j, β_j, γ_j are given in Table 3.2.

3.3 Calculation of the Theoretical Event Rates

We used the expression for the average expected event rate in the presence of oscillation in case of Chlorine and Gallium detectors given as:

$$R_j^{th} = \sum_{k=1\,\mathrm{to}\,8} \phi_k \int_{E_{th}^j}^{E_{max}} dE_\nu \lambda_k(E_\nu)[\sigma_{e,j}(E_\nu)\langle P_{ee}^k(E_\nu)\rangle]. \tag{3.3.1}$$

Here E_{th}^j is the process threshold for the jth detector (j=1,2,3 for Homestake, Gallax+GNO and SAGE respectively). The values of energy threshold E_{th}^j for Cl, Ga detectors are 0.814, 0.233 MeV respectively [81]. ϕ_k are the total neutrino fluxes taken from BS05(OP) [18]. For Gallium detector all fluxes contribute whereas for Chlorine detector all fluxes except pp flux contribute. $\lambda_k(E_\nu)$ are normalized solar neutrino energy spectra for different neutrino sources from the sun, taken from refs. [37, 86], and $\sigma_{e,j}$ is the interaction cross section for ν_e in the jth detector. Numerical data of energy dependent neutrino cross sections for chlorine and gallium experiments is available from ref. [86]. Event rates of Chlorine [87] and Gallium [60, 88] experiments and those calculated from Eq.(3.4.2) below directly come in the units of SNU.

SuperKamiokande (SK) and SNO detectors are sensitive for higher energies, so ϕ_k are the total ^{8}B and hep fluxes for these detectors respectively. The expression of the average

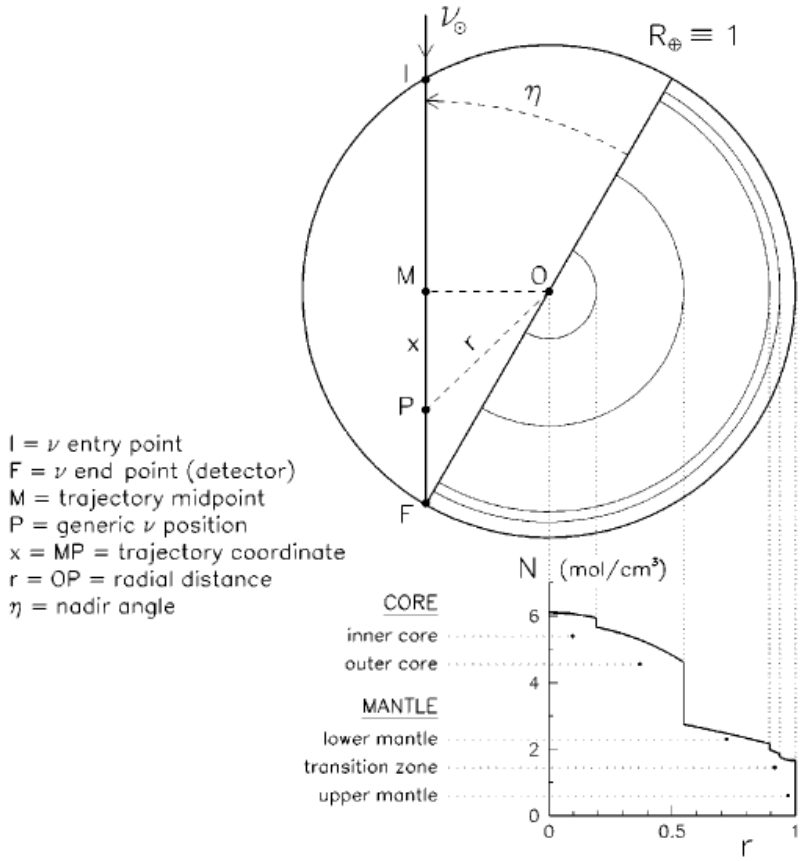

Figure 3.3: Section of the Earth showing different shells and the electron density profile $N(r)$. Different symbols used are also shown in the text [85].

expected event rate with oscillations for elastic scattering at SK detector is as below:

$$N_{SK}^{th} = \sum_{k=1,2} \phi_k \int_0^{E_{max}} dE_\nu \lambda_k(E_\nu) \cdot \{\sigma_e(E_\nu)\langle P_{ee}^k(E_\nu)\rangle + \sigma_\mu(E_\nu)[1 - \langle P_{ee}^k(E_\nu)\rangle]\}. \quad (3.3.2)$$

Here σ_e and σ_μ are elastic scattering cross sections for electron and muon neutrinos that we took from ref. [89].

For the SNO charged-current (CC) reaction, $\nu_e d \to e^- pp$, we calculated event rate using the expression:

$$N_{CC}^{th} = \sum_{k=1,2} \phi_k \int dE_\nu \lambda_k(E_\nu) \sigma_{CC}(E_\nu) \cdot \langle P_{ee}^k(E_\nu)\rangle. \quad (3.3.3)$$

Here σ_{CC} is $\nu_e d$ CC cross section of which calculational method and updated numerical results are given in refs. [90] and [91] respectively.

The expression for the event rate of the SNO neutral-current (NC) reaction, $\nu_x d \rightarrow \nu_x\, p\, n\, (x = e,\, \mu,\, \tau)$, is given as:

$$N_{NC}^{th} = \sum_{k=1,2} \phi_k \int dE_\nu \lambda_k(E_\nu) \sigma_{NC}(E_\nu) \cdot (\langle P_{ee}^k(E_\nu)\rangle + \langle P_{ea}^k(E_\nu)\rangle). \tag{3.3.4}$$

Here σ_{NC} is $\nu_x d$ NC cross section and $\langle P_{ea}^k(E_\nu)\rangle$ is the time average probability of oscillation into any other active neutrino. We used updated version of CC and NC cross section data from the website given in ref. [91]. In case of oscillation of the ν_e into active neutrino only, $\langle P_{ee}^k(E_\nu)\rangle + \langle P_{ea}^k(E_\nu)\rangle = 1$ and N_{NC}^{th} is a constant.

For Superkamiokande [66] and SNO [72] experiments, the event rates come in the unit of $10^6 \mathrm{cm}^{-2}\mathrm{s}^{-1}$. We converted these rates into ratios to SSM predicted rate. We also calculated theoretical event rates as ratios to SSM predicted rate in order to cancel out all energy independent efficiencies and normalizations [8].

$$R_j^{th} = \frac{N_j^{th}}{N_j^{SSM}} \tag{3.3.5}$$

Here N_j^{SSM} (j=4,5,6 for SK, SNO CC and SNO NC respectively) is the predicted number of events assuming no oscillations. We used the Standard Solar Model BS05(OP) [18] in our calculations. Theoretical event rates, so calculated, were used in Eq. (3.4.1) to calculate the chi-square function for different points in the $\tan^2\theta - \Delta m^2$ parameter space.

3.4 Calculation of the Error Matrix and χ^2 Function

The chi-square function to show the statistical significance of solar neutrino deficit can be given as:

$$\chi^2_{\mathrm{Rates}} = \sum_{j_1,j_2=1,6} (R_{j_1}^{th} - R_{j_1}^{exp})[V_{j_1 j_2}]^{-2}(R_{j_2}^{th} - R_{j_2}^{exp}), \tag{3.4.1}$$

where R_j^{th} is the theoretically calculated event rate with oscillations at detector j and R_j^{exp} is the measured rate for different experiments shown in table 3.1. For chlorine, Gallax+GNO and SAGE experiments R^{th} and R^{exp} are in the units of SNU (1 SNU=10^{-36}

captures/atom/sec) and for Superkamiokande, SNO CC and SNO NC these are used as ratio to SSM Eq. (3.3.5).

$V_{j_1 j_2}$ is the error matrix that contains experimental (systematic and statistical) errors and theoretical uncertainties that affect solar neutrino fluxes and interaction cross sections. For the calculation of the error matrix $V_{j_1 j_2}$ we followed ref. [92] and for updated uncertainties we used ref. [93]. Expression for the error matrix is given as:

$$V_{j_1 j_2} = \sigma^2_{j_1 j_2}(\mathrm{TH}) + \sigma^2_{j_1 j_2}(\mathrm{EXP}) = \sigma^2_{j_1 j_2}(\mathrm{TH}) + \delta_{j_1 j_2}\sigma^{exp}_{j_1}\sigma^{exp}_{j_2} \tag{3.4.2}$$

The theoretical errors come from the following sources:

1. The uncertainties in the capture cross-sections (CS) of the detectors. These are specified by uncorrelated relative errors $\Delta \ln C_{ij}$ in the energy-averaged total cross section for i^{th} source and j^{th} detector as given in Table 3.3.

2. The uncertainties in the astrophysical parameters[5] (AP) used as input in the building of different Standard Solar Models. These parameters are nuclear S-factors: S_{11}, S_{33}, S_{34}, $S_{1,14}$, S_{17}, the Luminosity (Lum), the metallacity (Z/X), the sun age (Age) and the opacity (Opa). These parameters are denoted as $\{x_k\}_{k=1,\ldots,9}$. The errors in these parameters are denoted by $\Delta \ln X_k$ given in table 3.4. The last two sources of error which are not listed in the ref. [92] are "Diffusion Error" and and the uncertainty in $^7Be(e^-, \nu_e)^7Li$ capture rate [93].

The expression for the theoretical errors is given as:

$$\sigma^2_{j_1 j_2}(\mathrm{TH}) = \sigma^2_{j_1 j_2}(\mathrm{CS}) + \sigma^2_{j_1 j_2}(\mathrm{AP}) \tag{3.4.3}$$

The contributions to $\sigma^2_{j_1 j_2}(\mathrm{CS})$ due to the uncertainties $\Delta \ln C_{ij}$ in the detector cross sections, are uncorrelated in both the indices (i, j) giving rise to the diagonal matrix.

$$\sigma^2_{j_1 j_2}(\mathrm{CS}) = \delta_{j_1 j_2} \sum_{i=1}^{8} R^2_{ij_1} (\Delta \ln C_{ij_1})^2, \tag{3.4.4}$$

[5] Astrophysical Parameters are discussed in detail in section 2.2.2

Table 3.3: $\Delta \ln C_{ij}$, relative errors of the energy averaged cross section in the form of natural logarithm. Uncertainties in the radiative corrections of scattering cross section are negligible [93].

Experiment	pp	pep	hep	Be	B	N	O	F
Ga	0.023	0.170	0.320	0.070	0.320	0.060	0.120	0.120
Cl	0	0.020	0.037	0.020	0.032	0.020	0.020	0.020
SK,SNO	0	0	0	0	0	0	0	0

Table 3.4: $\Delta \ln X_k$, relative errors of SSM input parameters [93].

S_{11}	S_{33}	S_{34}	$S_{1,14}$	S_{17}	Lum	Z/X	Age	Opa	Diff	C_{Be}
0.017	0.060	0.094	0.143	0.106	0.004	0.033	0.004	0.02	0.02	0.02

where R_{ij_1} are event rates with oscillation for i source and j_1 experiment calculated in the section 3.3.

The contributions to $\sigma^2_{j_1 j_2}(\mathrm{AP})$ come from the uncertainties in the input parameters X_k and affect all the fluxes ϕ_i systematically giving rise to off-diagonal elements in the error matrix. The relevant expression is given as:

$$\sigma^2_{j_1 j_2}(\mathrm{AP}) = \sum_{i_1=1}^{8} \sum_{i_2=1}^{8} R_{i_1 j_1} R_{i_2 j_2} \sum_{k=1}^{9} \alpha_{i_1 k} \alpha_{i_2 k} (\Delta \ln X_k)^2. \tag{3.4.5}$$

Here $\alpha_{ik} = \frac{\partial \ln \phi_i}{\partial \ln X_k}$ denotes the matrix giving error propagation from the input parameters X_k to the SSM fluxes ϕ_i[6]. The numerical values of α_{ik} are given in the table 3.5. Following the procedure for calculating the error matrix $V_{j_1 j_2}$ and using the theoretical and experimental event rates we used Eq. (3.4.1) and calculated χ^2 function for the grid of 101 $\times$ 101 values of Δm^2 and $\tan^2\theta$. The results of our analysis are given in the next section.

[6]Fluxes from the SSM BS05(OP) are given in the table 2.4.

Table 3.5: Logarithmic derivatives $\alpha_{ik} = \frac{\partial \ln \phi_i}{\partial \ln X_k}$, showing error propagation from the input parameters X_k to the SSM fluxes ϕ_i [93].

	pp	pep	hep	Be	B	N	O	F
S_{11}	+0.14	–0.17	–0.08	–0.97	–2.59	–2.53	–2.93	–2.94
S_{33}	+0.03	+0.05	–0.45	–0.43	–0.40	+0.02	+0.02	+0.02
S_{34}	–0.06	–0.09	–0.08	+0.86	+0.81	–0.05	–0.05	–0.05
$S_{1,14}$	–0.02	–0.02	–0.01	+0.00	+0.01	+0.85	+1.00	+0.01
S_{17}	+0.00	+0.00	+0.00	+0.00	+1.00	+0.00	+0.00	+0.00
Lum	+0.73	+0.87	+0.12	+3.40	+6.76	+5.16	+5.94	+6.25
Z/X	–0.08	–0.17	–0.22	+0.58	+1.27	+1.86	+2.03	+2.09
Age	–0.07	+0.00	-0.11	+0.69	+1.28	+1.01	+1.27	+1.29
Opa	+0.14	+0.24	+0.54	–1.38	–2.62	–1.67	–2.05	–2.13
Diff	+0.13	+0.22	+0.13	–0.90	–2.00	–2.56	–2.75	–2.75
C_{Be}	+0.00	+0.00	+0.00	+0.00	+0.00	+0.00	+0.00	+0.00

3.5 Results of the Global Analysis

Figure 3.4 and Table 3.6 show our best fit oscillation parameters, in different regions, calculated using a grid of 101 × 101 points of the parameter space. The symbol of star shows the best fit points in the respective regions of the parameter space. Calculations of goodness-of-fit and confidence level are described in the introduction (chapter 1). Calculation of the χ^2 function is described in detail in the section 3.4. We used ^{8}B flux constrained by the Standard Solar Model BS05(OP). We saw that the point with global minimum or the best fit point in the parameter space lies in the LMA region with $\Delta m^2 = 2.512 \cdot 10^{-5}\text{eV}^2$ and $\tan^2\theta = 3.981 \cdot 10^{-1}$ that is consistent with the results found in the literature where SNO data is included in the analysis [9, 10, 12]. Before including the SNO data the best fit was found in the SMA region [5, 83]. The increasing grey level, in Figure 3.4, shows regions with 90%, 95%, 99%, 99.73% C.L. (Confidence Level). Our best-fit points in different regions are marked by stars.

A selection of a fine grid with larger number of points in the parameter space, of course, will give better results. But limitations of the CPU time restricted us to a grid with a

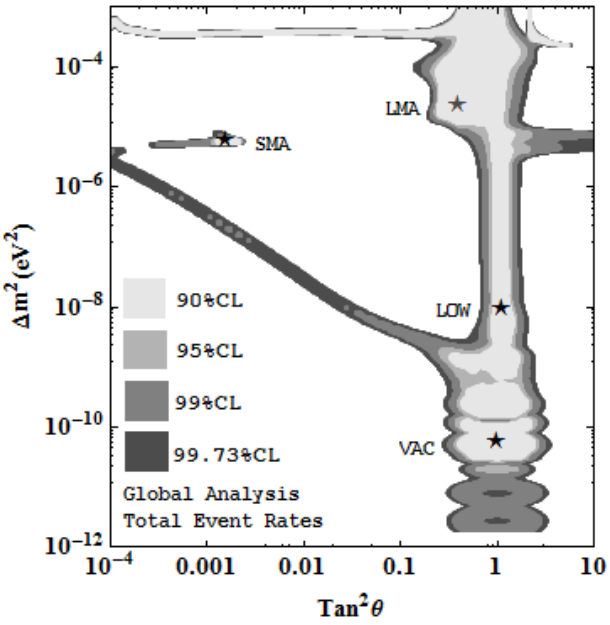

Figure 3.4: Our global solutions for the total rates. The input data includes total event rates of chlorine [87], weighted average of Gallax and GNO [88], SAGE [60], Superkamiokande [66], SNO CC and SNO NC [72]. The increasing grey level shows 90%, 95%, 99%, 99.73% C.L. Our best-fit points in different regions are marked by stars.

small number of points. For this problem we point out that even without increasing the number of points in the grid we can get lower χ^2 and better g.o.f. by *fine tuning* of the oscillation parameters using differential evolution (DE), technique of optimization. We describe what we mean by *fine tuning* and report our improvements obtained this way in the next chapter.

Table 3.6: Our best fit values of the neutrino oscillation parameters Δm^2, $\tan^2\theta$ along with $\chi^2_{\rm min}$ (4 d.o.f) (6(rates)-2(parameters: $\tan^2\theta, \Delta m^2$)) and g.o.f. corresponding to Figure 3.4.

Solution	$\Delta m^2(\mathrm{eV}^2)$	$\tan^2\theta$	$\chi^2_{\rm min}$	g.o.f.
LMA	$2.512 \cdot 10^{-5}$	$3.981 \cdot 10^{-1}$	0.808	93.77%
VAC	$6.31 \cdot 10^{-11}$	$1.00 \cdot 10^{0}$	1.268	86.72%
LOW	$1.00 \cdot 10^{-8}$	$1.122 \cdot 10^{0}$	4.09	39.46%
SMA	$6.31 \cdot 10^{-6}$	$1.585 \cdot 10^{-3}$	7.78	10.01%

Chapter 4

Optimizing Neutrino Oscillation Parameters using Differential Evolution

In the previous chapter we discussed the global analysis of the neutrino data using grid-based method and found the best fit values of Δm^2 and $\tan^2 2\theta$ in 101×101 grid of the parameter space. There we used Δm^2 and $\tan^2\theta$ as exponential functions of the variables x_1 and x_2, described by the Eqs. (3.2.1) and (3.2.2), and selected the grid with discrete values of x_1 and x_2. For each region of the parameter space, namely SMA, LMA, LOW and VAC discussed earlier, best fit parameters (given in the table 3.6) were found. In this chapter, we explore the regions around these points using Differential Evolution (DE), our selected optimization technique. For this purpose we use continuous values of x_1 and x_2 to explore different regions of the parameter space.

Here we discuss briefly about function optimization and different optimization techniques in section 4.1 and 4.2 respectively. We discuss the differential evolution (DE) technique in some detail in section 4.3. The results of our analysis using DE are given in section 4.4.

4.1 Function Optimization

The *optimization* is the most widely used method for performing minimization and maximization of an objective function which we want to minimize or maximize. Maxima and minima are points in the domain of a function at which the function has the largest (maximum), or smallest (minimum) value either within a given neighborhood (called local extrema), or on the function domain in its entirety (called global extrema) [94].

4.1.1 Local Optimization

A point x' is a local (or relative) maximum of a function f if there exists some $\varepsilon > 0$ such that $f(x') \geq f(x)$ for all x with $|x - x'| < \varepsilon$. On a graph of a function, its local maxima will look like the tops of hills.

A local minimum is a point x' for which $f(x') \leq f(x)$ for all x with $|x - x'| < \varepsilon$. On a graph of a function, its local minima will look like the bottoms of valleys.

4.1.2 Global Optimization

A global (or absolute) maximum is a point x' for which $f(x') \geq f(x)$ for all x. Similarly, a global minimum is a point x' for which $f(x') \leq f(x)$ for all x. Any global maximum (minimum) is also a local maximum (minimum), however, a local maximum or minimum need not also be a global maximum or minimum [95].

4.1.3 Optimization of Simple Analytical Functions

For twice-differentiable functions in one variable, a simple technique for finding local maxima and minima is to look for stationary points, which are points where the first derivative is zero. If the second derivative at a stationary point is positive, the point is a local minimum; if it is negative, the point is a local maximum; if it is zero, further investigation is required. If the function is defined over a bounded segment, one also need to check the end points of the segment. Following are examples of optimization of simple

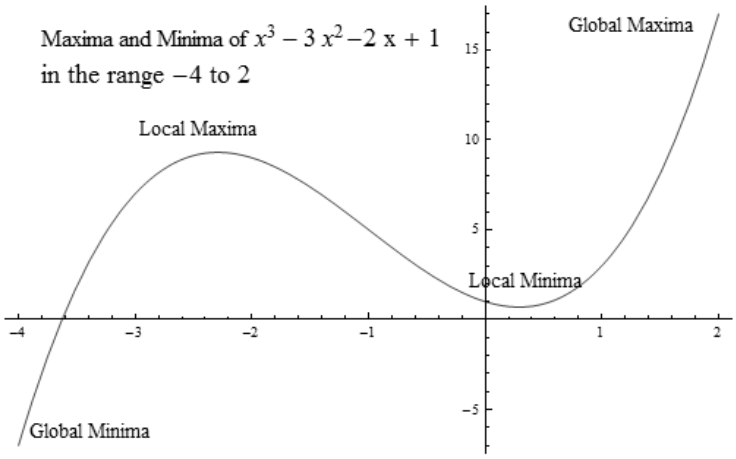

Figure 4.1: A graph illustrating local minima/maxima and global minima/maxima points.

analytical functions [96].

Examples:

- The function x^2 has a unique global minimum at $x = 0$.
- For the function x^3, the first derivative ($3x^2$) is 0 at $x = 0$. But the second derivative ($6x$) is also 0. Hence it has no global or local minima or maxima.
- The function $\frac{x^3}{3} - x$ has first derivative $x^2 - 1$ and second derivative $2x$. Setting the first derivative to 0 and solving for x gives stationary points at -1 and +1. From the sign of the second derivative we can see that -1 is a local maximum and +1 is a local minimum.
- The function $|x|$ has a global minimum at x = 0 that cannot be found by taking derivatives, because the derivative does not exist at $x = 0$.
- The function $\cos(x)$ has infinitely many global maxima at 0, $\pm 2\pi$, $\pm 4\pi$, ..., and infinitely many global minima at $\pm\pi$, $\pm 3\pi$, ...
- The function $2\cos(x) - x$ has infinitely many local maxima and minima.

- The function $x^3 + 3x^2 - 2x + 1$, defined over the closed interval (segment) [-4,2] (see graph figure 4.1), has two extrema: one local maximum at $x = (-1 - \sqrt{15})/3$, one local minimum in $x = (-1 + \sqrt{15})/3$, a global maximum on $x = 2$ and a global minimum on $x = -4$ at the end points.

4.2 Optimization Techniques

Depending on the type of functions involved, optimization problems can be divided into linear and nonlinear (polynomial, algebraic, transcendental etc.) problems. Here we discuss briefly about these types and methods for their optimization.

4.2.1 Linear Programming Problems

These are the optimization problems where the objective function and constraints are all linear. The algorithms commonly used for the optimization of such type of problems are:

Simplex and Revised Simplex Algorithms

These algorithms solve the problems by constructing a feasible solution at the vertex of the polytope[1] defined by the constraints, and then moving along the edges of the polytope to vertices with successively smaller values of the objective function until the minimum is reached. Typically, for a linear programming problem with many more variables than constraints, the *revised simplex* algorithm is faster than the *simplex* algorithm. On the other hand, if there are many more constraints than variables, the simplex algorithm is faster [99].

Interior Point Algorithm

Although the simplex and revised simplex algorithms can be quite efficient on average, they have a poor worst-case behavior. It is possible to construct a linear programming problem

[1] In elementary geometry, a polytope is a geometric object with flat sides, which exists in any general number of dimensions. For example, a polygon is a polytope in two dimensions and a polyhedron in three dimensions [97].

for which the simplex or revised simplex methods take a number of steps exponential in the problem size. The interior point algorithm [100], however, has been proven to converge in a number of steps that are polynomial in the problem size.

4.2.2 Non-linear Programming Problems

These are the programming problems where the objective function and constraints are non-linear. Numerical algorithms for constrained nonlinear optimization can be broadly categorized into gradient-based methods and direct search methods.

Gradient-based Methods

Such type of methods use first derivatives (gradients) or second derivatives (Hessians) information. Different examples gradient-based methods are:

- *Sequential Quadratic Programming (SQP) methods:* are iterative methods for non-linear optimization. Unlike sequential linearly constrained methods, which are effective when most of the constraints are linear, SQP methods show their strength when solving problems with significant nonlinearities [101].

- *Interior Point methods:* As described above for linear programming problems, the Interior Point methods can be used for non-linear convex function optimization problems as well. Interior-point methods became popular in 1980s when Karmarkar described a polynomial algorithm that approaches the solution through the interior of the feasible polytope rather than working its way around the boundary as the simplex method does [101].

- *Augmented Lagrangian methods:* are the alogorithms for solving constrained optimization problems. These are similar to penalty methods that replace a constrained optimization problem by a series of unconstrained problems. The difference is that the augmented Lagrangian method adds an additional term to the unconstrained objective. This additional term is designed to mimic a Lagrange multiplier [102].

Direct Search Methods

Such type of methods do not use derivative information. Direct search methods tend to converge more slowly, but can be more tolerant to the presence of noise in the function and constraints. These methods are Nelder-Mead, Genetic Algorithms, Differential Evolution and Simulated Annealing. We discuss the Differential Evolution in detail in the next section. Other methods are described briefly as below:

- *Nelder-Mead method:* is a nonlinear optimization technique proposed by John Nelder & Roger Mead (1965). This method is some times termed as "simplex" method which is different from the well known simplex method for linear optimization. The algorithm uses the concept of a simplex which is polytope of $N + 1$ vertices in N dimensions. Different examples of simplices are: a line segment on a line, a triangle on a plane and a tetrahedron in three-dimensional space [19, 98].

- *Genetic Algorithms:* are the methods that belong to a larger class called Evolutionary Algorithms (EAs) which solve the problems using techniques, inspired by natural evolution, that are *inheritance*, *mutation*, *selection*, and *crossover* [21].

- *Simulated Annealing:* is a simple stochastic function minimizer. The name is motivated by the physical process of anealing, where a metal object is heated to a high temperature and allowed to cool slowly. The process allows the atomic structure of the metal to settle to a lower energy state, thus becoming a tougher metal. Using optimization terminology, annealing allows the structure to escape from a local minimum, and to explore and settle on a better, hopefully global, minimum [20].

It is to be noted that the technique we used in chapter 3 is a grid search method for optimization where we evaluate the objective function at a large number of selected points and then compare the outputs to decide where the output has a global minima or maxima among the selected points.

4.3 Differential Evolution

Differential Evolution (DE) is a simple population based, stochastic direct search method for optimization of real valued, non-linear, non-differentiable objective functions. It was first introduced by Storn and Price in 1997 [23]. Differential Evolution proved itself to be the fastest evolutionary algorithm when participated in First International IEEE Competition on Evolutionary Optimization [103]. DE performed better when compared to other optimization methods like Annealed Nelder and Mead strategy [19], Adaptive Simulated Annealing [20], Genetic Algorithms [21] and Evolution Strategies [22] with regard to number of function evaluations (nfe) required to find the global minima. DE algorithm is easy to use, robust and gives consistent convergence to the global minimum in consecutive independent trials [23, 24].

The general algorithm of DE [104] for minimizing an objective function carries out a number of steps. Here we summarize the steps we carried out for minimizing the χ^2 function defined in section 3.4. We did optimization of the χ^2 function individually for different regions of the parameter space to do one fine tuning in each region. The results of the optimization are reported in the section 4.4 below.

Step I

An array of vectors was initialized to define a population of size NP=20 with D=2 parameters as

$$\mathbf{x}_i = x_{j,i} \text{ where } i = 1, 2, ..., \texttt{NP} \text{ and } j = 1, .., \texttt{D}. \tag{4.3.1}$$

The parameters, involved here, are x_1 and x_2 of Eqs.(3.2.1) and (3.2.2) on which $\Delta m^2/E$ and $\tan^2\theta$ depend. Upper and lower bounds ($b_{j,U}$ and $b_{j,L}$), individually for different regions of the parameter space described in the introduction (chapter 1), for the x values were specified and each vector i was assigned a value according to

$$x_{j,i} = \text{rand}_j(0, 1) \cdot (b_{j,U} - b_{j,L}) + b_{j,L} \tag{4.3.2}$$

where $\text{rand}_j \in [0,1]$ is j^{th} evaluation of a uniform random number generator. The χ^2 function was calculated for each vector of the population and the vector with least χ^2 function value was selected as base vector $\mathbf{x}_{r_o}$.

Step II

Weighted difference of two randomly selected vectors from the population was added to the base vector $\mathbf{x}_{r_o}$ to produce a mutant vector population $\mathbf{v}_i$ of `NP` trial vectors. The process is known as *mutation*.

$$v_i = \mathbf{x}_{r_o} + F \cdot (\mathbf{x}_{r_1} - \mathbf{x}_{r_2}). \tag{4.3.3}$$

Here the scale factor $F \in [0,2]$ is a real number that controls the amplification of the differential variation. The indices $r_1, r_2 \in [1, \texttt{NP}]$ are randomly chosen integers and are different from r_o.

Different variants of DE *mutation* are denoted by the notation '`DE/x/y/z`', where `x` specifies the vector to be mutated which can be "rand" (a randomly chosen vector) or "best" (the vector of the lowest χ^2 from the current population), `y` is the number of difference vectors used and `z` is the crossover scheme. The above mentioned variant Eq.(4.3.3) is `DE/best/1/bin`, where the best member of the current population is perturbed with `y`=1 and the scheme `bin` indicates that the crossover is controlled by a series of independent binomial experiments. The two variants, reported in the literature [23, 24], very useful for their good convergence properties, are `DE/rand/1/bin`

$$v_i = \mathbf{x}_{r_1} + F \cdot (\mathbf{x}_{r_2} - \mathbf{x}_{r_3}), \tag{4.3.4}$$

and `DE/best/2/bin`

$$\mathbf{v}_i = \mathbf{x}_{ro} + F \cdot (\mathbf{x}_{r_1} + \mathbf{x}_{r_2} - \mathbf{x}_{r_3} - \mathbf{x}_{r_4}) . \tag{4.3.5}$$

For our problem, we used the variant `DE/best/2/bin` Eq.(4.3.5) for DE mutation, where 2 difference vectors were added to the base vector. The values of F we used are reported in section 4.4 below.

Step III

The parameters of *mutant vector* population Eq.(4.3.5) were mixed with the parameters of *target vectors* Eq.(4.3.1) in a process called uniform *crossover* or discrete recombination. After the cross over the *trial vector* became:

$$\mathbf{u}_i = u_{j,i} = \begin{cases} v_{j,i} & \text{If } (\text{rand}_j(0,1) \leq \texttt{Cr} \text{ or } j = j_{\text{rand}}), \\ x_{j,i} & \text{otherwise.} \end{cases} \tag{4.3.6}$$

Here $\texttt{Cr} \in [0,1]$ is the cross over probability that controls fraction of the parameters inherited from the mutant population (the values of `Cr` we used are given in section 5), $\text{rand}_j \in [0,1]$ is the output of a random number generator and $j_{\text{rand}} \in [1,2]$ is a randomly chosen index.

Step IV

The χ^2 function was evaluated for each of the trial vector $\mathbf{u}_i$ obtained from Eq.(4.3.6). If the trial vector resulted in lower objective function than that of the target vector $\mathbf{x}_i$, it replaced the target vector in the following generation. Otherwise the target vector was retained. (This operation is called *selection.*) Thus the target vector for the next generation became:

$$\mathbf{x}'_i = \begin{cases} \mathbf{u}_i & \text{If } \chi^2(\mathbf{u}_i) \leq \chi^2(\mathbf{x}_i), \\ \mathbf{x}_i & \text{otherwise.} \end{cases} \tag{4.3.7}$$

The processes of mutation, crossover and selection were repeated until the optimum was achieved or the number of iterations (generations) specified in section 4.4 were completed.

4.4 Optimization of the Chi-square Function using DE

We have described algorithm of the Differential Evolution in detail in section 4.3. We wrote the subroutine of the chi-square function, denoted by χ^2, following the procedure to calculate chi-square in the section 3.4, that depends on x_1 and x_2 and used it as objective function of the DE algorithm. We combined the traditional grid-based method with DE

in two aspects: First, we used the survival probabilities $\langle P^k_{ee}(E_\nu)\rangle$ already calculated for the discrete values of x_1 and x_2 for our grid of 101 $\times$ 101 points of the parameter space and interpolated them to the continuous values of x_1 and x_2 to calculate event rates and chi-square function in DE algorithm. We used cubic polynomial fit for the interpolation purpose to fit the data. Second, we used the points with minimum chi-square in different regions of the selected grid reported in Table 3.6 as the starting points (and members of the respective population array) and explored the space around them for the *fine tuning*. That is, we searched for the points with smaller χ^2 values and better goodness-of-fit of the oscillation parameters.

In our analysis, the values of DE control variables `F` and `CR` were taken as 0.4 and 0.9 respectively for the LMA, SMA and VAC regions. For the LOW region `F` and `CR` were both taken as 0.3 for better convergence. Maximum number of iterations were taken to be 50 for all regions. We took the best point in a region of the 101 $\times$ 101 grid in Table 3.6 as the first member of the population in the first iteration and used the strategy `DE/best/2/bin` for DE mutation in all the remaining iterations/generations. The steps of DE algorithm, described in section 4.3, are repeated for the number of iterations specified.

Table 4.1 and Figure 4.2 show the results in different regions during and after fine tuning of the oscillation parameters using Differential Evolution. The value of $\chi^2_{\rm min}$ persisted, rejecting all the mutations, for the iterations mentioned in column 2 of Table 4.1. Accepted mutations resulted in new vectors whose components are given in column 3 and 4 of the following rows. $\chi^2_{\rm best}$ is the minimum chi-square value we obtained in the region specified. In comparison to the results of Table 3.6, we note here as much as 4 times decrease in the $\chi^2_{\rm min}$ of the SMA region after fine tuning using DE along with a small decrease in all the other regions. Different vectors in Figure 4.2 show the track of DE algorithm for optima in different regions during iterations specified in Table 4.1.

Solution	Iterations	$\Delta m^2(\text{eV}^2)$	$\tan^2\theta$	χ^2_{min}	χ^2_{best}	g.o.f.
	1-7	$2.51189 \cdot 10^{-5}$	$3.98107 \cdot 10^{-1}$	0.808314		93.77%
	8-9	$2.50999 \cdot 10^{-5}$	$3.97855 \cdot 10^{-1}$	0.807316		
	10-13	$2.40927 \cdot 10^{-5}$	$3.97684 \cdot 10^{-1}$	0.804711		
	14	$2.49798 \cdot 10^{-5}$	$3.97287 \cdot 10^{-1}$	0.804564		
LMA	15	$2.49307 \cdot 10^{-5}$	$3.97028 \cdot 10^{-1}$	0.804289		
	16	$2.45884 \cdot 10^{-5}$	$3.97912 \cdot 10^{-1}$	0.804424		
	17-21	$2.46633 \cdot 10^{-5}$	$3.9751 \cdot 10^{-1}$	0.803315		
	22-29	$2.43264 \cdot 10^{-5}$	$3.98097 \cdot 10^{-1}$	0.803192		
	30-50	$2.45084 \cdot 10^{-5}$	$3.9751 \cdot 10^{-1}$	0.802953	0.802953	93.82%
	1	$6.30957 \cdot 10^{-11}$	1.0	1.26779		86.72%
	2-3	$6.64977 \cdot 10^{-11}$	1.0277	1.260239		
VAC	4-6	$6.70641 \cdot 10^{-11}$	1.01912	1.25977		
	7-43	$6.6423 \cdot 10^{-11}$	0.993134	1.25948		
	44-45	$6.6423 \cdot 10^{-11}$	0.998353	1.25945		
	46-50	$6.70041 \cdot 10^{-11}$	0.99326	1.25939	1.25939	86.82%
	1-3	$6.30957 \cdot 10^{-6}$	$1.58489 \cdot 10^{-3}$	7.77933		10.01%
SMA	4	$6.19532 \cdot 10^{-6}$	$1.64599 \cdot 10^{-3}$	6.24974		
	5	$6.10563 \cdot 10^{-6}$	$1.48276 \cdot 10^{-3}$	5.89341		
	6-50	$5.48095 \cdot 10^{-6}$	$1.72371 \cdot 10^{-3}$	1.86456	1.86456	75.97%
	1	$1.0 \cdot 10^{-8}$	1.12208	4.18897		39.46%
	2-4	$2.37807 \cdot 10^{-8}$	1.03198	3.98339		
	5-9	$2.95404 \cdot 10^{-8}$	1.03198	3.97624		
LOW	10	$3.3042 \cdot 10^{-8}$	1.03069	3.97605		
	11	$2.80796 \cdot 10^{-8}$	1.02741	3.9728		
	12-20	$3.17357 \cdot 10^{-8}$	1.02741	3.96267		
	21-50	$3.14543 \cdot 10^{-8}$	1.02723	3.96125	3.96125	41.12%

Table 4.1: The results of the oscillation parameters during different iterations of the DE algorithm. The improved values of the oscillation parameters Δm^2, $\tan^2\theta$ along with χ^2_{best} (4 d.o.f) and g.o.f. using Differential Evolution strategy `DE/best/2/bin` corresponding to Figure 4.2 are presented. Note in the 1^{st} row of different regions, the points with minimum chi-square given in table 3.6 are taken as first members of the population arrays. The other members of the arrays, for different regions, are selected randomly using DE.

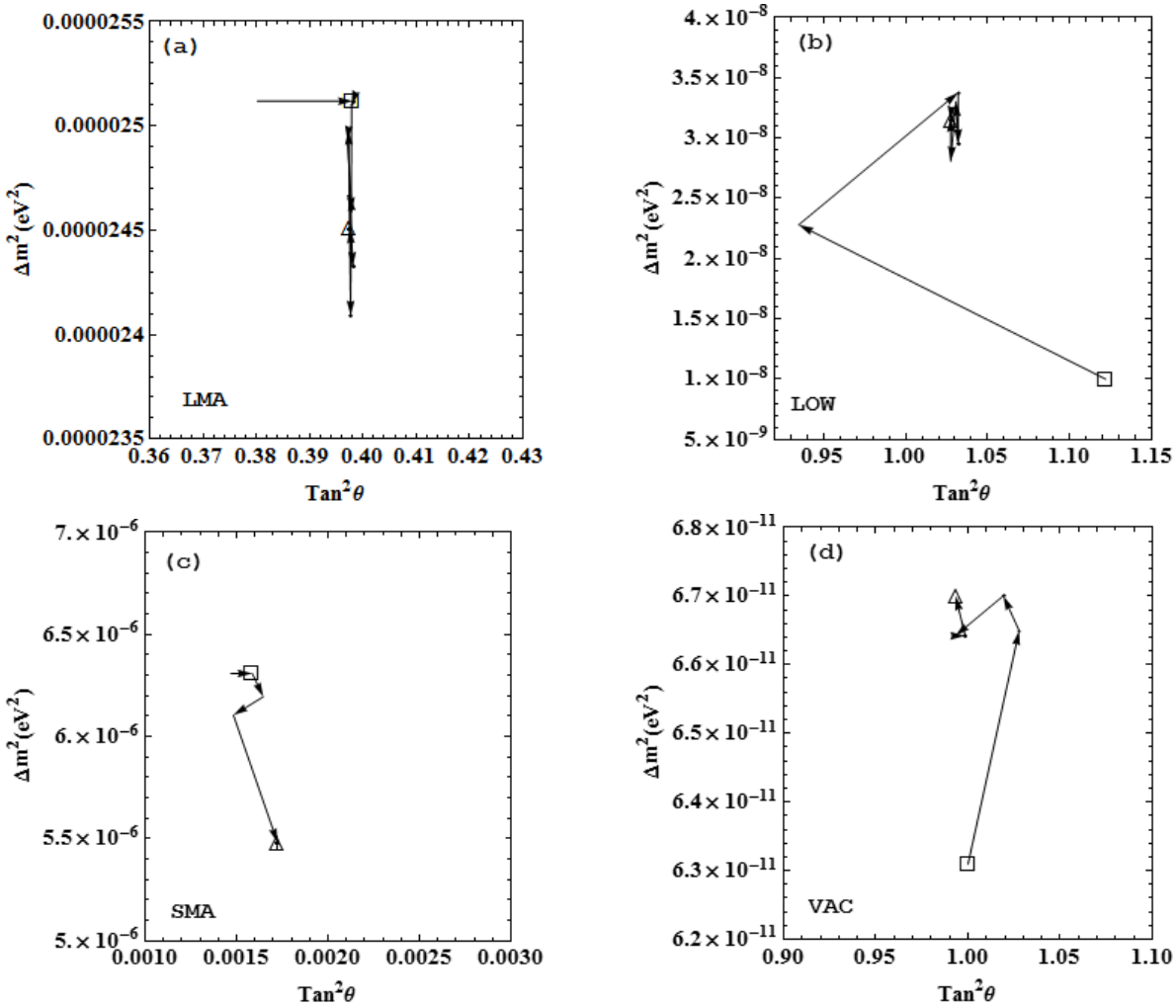

Figure 4.2: Track of the DE algorithm for optima in different regions using the strategy `DE/best/2/bin`. The square symbol shows the best point of the 101 × 101 grid and triangle symbol shows the best point after fine tuning using DE.

Chapter 5

Conclusions

In this work we presented an introduction of the neutrino physics necessary to understand the neutrino oscillation parameters (for two neutrinos in our case) for solar neutrinos. It includes early history of neutrino, solar models and solar neutrino problem (SNP). Further it encompasses the searches for the solution of SNP that come to the phenomena of neutrino oscillations. A complete understanding of the theory of neutrino oscillations, as it travels from source regions in the sun to the solar surface and to the detector at the earth, is necessary to pinpoint the parameters responsible for the survival probabilities of solar neutrinos at different stages. The precise measurement of the neutrino oscillation parameters will surely broaden the horizon of our knowledge about the neutrinos. We presented the optimal values of the oscillation parameters in the global analysis of the neutrino data, first using grid search optimization technique for a selected grid, in different regions of the parameter space. In addition to that, fine tuning of the neutrino oscillation parameters, using the second optimization technique named Differential Evolution, has been introduced as a solution to the impasse faced due to CPU limitations of the larger grid in the first technique. Using the second technique, we can explore the parameter space deeply due to real nature of the parameters x_1 and x_2, described in chapter 3, using DE in contrast to discrete nature of these parameters in the traditional (first) grid based method. We conclude that combination of Differential Evolution along with traditional

method provides smaller chi-square values and better goodness-of-fit of the neutrino oscillation parameters in different regions of the parameter space. We also note a significant change in the results of $\chi^2_{\rm min}$ and g.o.f. in the SMA region after the fine tuning using DE. Even though it is a local decrease, it indicates importance of the exploration of the points between the grid values and the efficiency that can be achieved through DE.

In the present work we have not included the energy bin data of SK and SNO experiments and the reactor neutrino data for the sake of simplicity to check the implementation and efficiency of the DE technique. However, this study shows that the introduced technique represents a useful methodological advancement in analysis of solar neutrino data that could be applied to more up-to-date data.

Bibliography

[1] B. Pontecorvo, Zh. Eksp. Teor. Fiz. **37** (1959) 1751; JETP **10** (1960) 1236.

[2] L. Wolfenstein, Phys. Rev. **D 17**, 2369 (1978).

[3] SNO Collaboration, Phys. Rev. Lett. **89**(1), 011302 (2002).

[4] M.V. Garzelli, C. Giunti, Astroparticle Physics **17**, 205–220 (2002) .

[5] J.N. Bahcall, P. I. Krastev and A. Yu. Smirnov, Phys. Rev. **D 58**, 096016 (1998).

[6] M.C. Gonzalez-Garcia *et al.*, Nuclear Physics **B 573**, 3–26 (2000).

[7] M.C. Gonzalez-Garcia and C. Peña-Garay, Nuclear Physics B (Proc. Suppl.) **91**, 80–88 (2001).

[8] M.C. Gonzalez-Garcia and C. Peña-Garay, Phys. Rev. **D 63**, 073013 (2001).

[9] J.N. Bahcall, P. I. Krastev and A. Yu. Smirnov, J. High Energy Phys. **05**, 015 (2001).

[10] J.N. Bahcall, M. C. Gonzalez-Garcia and C. Peña-Garay, J. High Energy Phys. **08**, 014 (2001).

[11] P.I. Krastev and A. Yu. Smirnov, Phys. Rev. **D 65**, 073022 (2002).

[12] J.N. Bahcall, M.C. Gonzalez-Garcia and C. Peña-Garay, J. High Energy Phys. **07**, 054 (2002).

[13] P.C. de Holanda and A.Yu. Smirnov, Phys. Rev. **D 66**, 113005 (2002).

[14] P. Aliani *et al.*, Phys. Rev. **D 67**, 013006 (2003).

[15] S. Goswami, A. Bandyopadhyayb and S. Choubey, Nuclear Physics B (Proc. Suppl.) **143**, 121–128 (2005).

[16] P. Yang and Q.Y. Liu, Chin. Phys. Lett. Vol.**26** No.3, 031401 (2009).

[17] P. Yang and Q.Y. Liu, Chin. Phys. Lett. Vol.**26** No.8, 081402 (2009).

[18] J.N. Bahcall, A.M. Serenelli and S. Basu, Astrophys. J. **621**, L85–L88 (2005).

[19] W.H. Press, S.A. Teukolsky, W.T. Vetterling, B.P. Flannery, *Numerical recipes in C*, Cambridge University Press (1992).

[20] L. Ingber, Matheml. Comput. Modeling, Vol.**18**, No.**11**, 29–57 (1993).

[21] D.E. Goldberg, *Genetic Algorithms in Search, Optimization and Machine Learning*, Addison-Wesley (1989).

[22] H.P. Schwefel, *Evolution and Optimum Seeking*, John Wiley In. (1995).

[23] R. Storn, K. Price, J. Glob. Optim. **11**, 341–59 (1997).

[24] P.K. Bergey, C. Ragsdale, Omega **33** 255–265 (2005).

[25] E. Charles, M. Karl von, *Wolfgang Pauli, A Biographical Introduction*, p. 19, Springer-Verlag (1994).

[26] J. Chadwick, Nature, vol. **129**, 312 (1932).

[27] F. Reines, Rev. Mod. Phys., vol. **68**, 317 (1996).

[28] G. Danby, et al., Phys. Rev. Lett., vol. **9**, 36 (1962).

[29] M.L. Perl, et al., Phys. Rev. Lett. **35** 1489 (1975).

[30] DONUT Collaboration, Phys. Lett. B, vol. **504**, 218–224, (2001).

[31] J.N. Bahcall, arXiv:physics/**0411190v1** [physics.ed-ph], (2004).

[32] J.N. Bahcall, W.A. Fowler, I. Iben Jr. and R.L. Sears, Astrophysical Journal, vol. **137**, 344-346 (1963).

[33] Aldo Serenelli, in *Neutrinos in Particle Physics, Astrophysics and Cosmology*, edited by F.J.P. Soler, C.D. Froggatt, F. Muheim CRC Press (2009).

[34] B.W. Carroll, D.A. Ostile, *An Introduction to Modern Astrophyics* (Second Edition), Pearson Education Inc. (2007).

[35] J.N. Bahcall, Phys. Rev. Lett. **12** 300–302, (1964); R. Davis Jr., Phys. Rev. Lett. **12**, 303–305 (1964).

[36] J.N. Bahcall, *Neutrino Astrophysics*, Cambridge University Press (1989).

[37] J.N. Bahcall and R.K. Ulrich, Rev. Mod. Phys. **60**, 297 (1988); J.N. Bahcall, Phys. Rev. **D 49**, 3923 (1994).

[38] J.N. Bahcall, M.H. Pinsonneault, Rev. Mod. Phys. **67**, 781–808 (1995).

[39] J.N. Bahcall, S. Basu, M.H. Pinsonneault, Physics Letters **B 433**, 1–8 (1998).

[40] J.N. Bahcall, M.H. Pinsonneault, S. Basu, Astrophys. J. **555**, 990–1012 (2001).

[41] J.N. Bahcall, M.H. Pinsonneault, Phys. Rev. Lett. **92**, 121301 (2004).

[42] E.G. Adelberger, et al., Rev. Mod. Phys., vol. **70**, 1265 (1998); W.C. Haxton, P.D. Parker, C.E. Rolfs, Nucl. Phys. **A777**, 226-253 (2006).

[43] R.W. Kavanagh, in *Essays in nuclear astrophysics*, edited by C.A. Barnes, D.D. Clayton, D.N. Schramm (1982).

[44] J.N. Bahcall, Phys. Rev. **C 65**, 025801 (2002).

[45] N. Grevesse, Physica Scripta. Vol. **T8**, 49–58 (1984).

[46] L.H. Aller , *Spectroscopy of Astrophysical Plasmas*, edited by A. Dalargoo and D. Layzer (Cambridge: Cambridge University Press), **p.89** (1986).

[47] W.C. Bradley, D.A. Ostlie, *An Introduction to Modern Astrophysics*, **p.350**, Pearson Education, Inc. (2007)

[48] W.F. Huebner, in *Physics of the sun*, edited by P.A. Sturrock, et. al., vol. I, **p.33** (1986).

[49] J.N. Bahcall, W.F. Huebner, S.H. Lubow, P.D. Parker, and R.K. Ulrich, Rev. Mod. Phys. **54**, 767 (1982).

[50] J.N. Bahcall, A.M. Serenelli and S. Basu, The Astrophysical Journal Supplement Series, **V 165**, Issue 1, pp. 400–431 (2006).

[51] J.N. Bahcall, M.H. Pinsonneault,S. Basu, J. Christensen-Dalsgaard, , Phys. Rev. Lett. **78** (2), 171-174 (1997).

[52] R.J. Davis, D.S. Harmer, K.C. Hoffman , Phys. Rev. Lett., vol.**20**, 1205–1209 (1968).

[53] B.T. Cleveland, et.al., Astrrophys. J. **496**, 505–526 (1998).

[54] J.N. Bahcall, et.al., Phys. Rev. Lett. **40**, 1351-1354 (1978).

[55] Gallex Collaboration, Phys. Lett. B, **447**, 127–133 (1999).

[56] Gallex Collaboration, Phys. Lett. B, **420**, 114 (1998); Phys. Lett. B, **436**, 158 (1998).

[57] GNO Collaboration, Phys. Lett. B, **616**, 174 (2005).

[58] V.N. Gavrin, for the SAGE Collaboration, Nucl. Phys. Proc. Suppl. **16**, 483–484 (1990).

[59] V.N. Gavrin, for the SAGE Collaboration, Nucl. Phys. Proc. Suppl. **138**, 87–90 (2005).

[60] J.N. Abdurashitov, et. al., Phys. Rev. **C 80**, 015807 (2009).

[61] K.S. Hirata, et.al., Phys. Rev. **D 44**, 2241 (1996).

[62] Kamiokande Collaboration, Phys. Rev. Lett. **77**, 1683 (1996).

[63] Super-Kamiokande Collaboration, Nucl. Instrum. Meth. **A 501**, 418–462, (2003).

[64] Super-Kamiokande Collaboration, Phys. Lett. **B 539**, 179–187 (2002).

[65] Super-Kamiokande Collaboration, Phys. Rev. **D 78**, 032002 (2008).

[66] Super-Kamiokande Collaboration, Phys. Rev. **D 83**, 052010 (2011).

[67] SNO Collaboration, Nucl. Instrum. Meth. **A 449**, 172–207 (2000).

[68] SNO Collaboration, [arXiv:**1109.0763v1**][nucl-ex] (2011).

[69] SNO Collaboration, Phys. Rev. Lett. **87**, 071301 (2001).

[70] SNO Collaboration, Phys. Rev. Lett. **92**, 181301 (2003).

[71] SNO Collaboration, Phys. Rev. **C 72**, 055502 (2005).

[72] SNO Collaboration, Phys. Rev. Lett. **101**, 111301 (2008).

[73] SNO Collaboration, arXiv:**1107.2901v1** [nucl-ex] (2011).

[74] W.T. Winter, et.al., Phys. Rev. **C 73**, 025503 (2006).

[75] Mark Thomson, Phil. Trans. R. Soc. Lond. **A 360**, 921–938 (2002).

[76] L. Wolfenstein, Phys. Rev. **D 17**, 2369 (1978).

[77] W.M. Alberico, S.M. Bilenki, Phys. Part. Nucl. **35** 297–323 (2004); Fiz. Elem. Chast. Atom. Yadra **35**, 545–596 (2004).

[78] S. Toshev, Phys. Lett. **B 196**, 170 (1987).

[79] W.C. Haxton, Phys. Rev. **D 35**, 2352 (1987).

[80] S.M. Bilenki, Lectures given at the European School of High Energy Physics CPapiernicka, Slovakia, arXiv:hep-ph/**0001311v1** (1999).

[81] M.C. Gonzalez-Garcia, Yosef Nir, Rev. Mod. Phys. **75**, 345 (2003).

[82] E. Lisi, et. al., Phys. Rev. **63**, 093002 (2002).

[83] J.N. Bahcall and P.I. Krastev, Phys. Rev. **56**, 2839 (1997).

[84] A.M. Dziewonski and D.L. Anderson, Phys. Earth Planet. Inter. **25**, 297 (1981).

[85] E. Lisi, D. Montanio, Phys. Rev. **D 56**, 1792 (1997).

[86] J.N. Bahcall, et.al., Phys. Rev. **C 54**, 411 (1996); J. N. Bahcall, Phys. Rev. **C 56**, 3391 (1997).

[87] B.T. Cleveland, et.al., Astrophys. J. **496**, 505 (1998).

[88] C.M. Cattadori, Nuclear Physics B (Proc. Suppl.) **110**, 311-314 (2002).

[89] J.N. Bahcall, et.al., Phys. Rev. **D 51**, 6146 (1995).

[90] S. Nakamura, et.al., Phys. Rev. **C 63**, 034617 (2001); S. Nakamura, et.al., ibid. 73, 049904(E) (2006).

[91] S. Nakamura, et.al., Nuclear Physics **A 707**, 561–576 (2002).

[92] G.L. Fogli and E. Lisi, Astropart. Phys. **3** 185 (1995).

[93] G.L. Fogli and E. Lisi, Phys. Rev. **D 62**, 013002 (2001).

[94] J. Stewart, *Calculus: Early Transcendentals* (6th ed.), Brooks/Cole. ISBN 0-495-01166-5 (2008).

[95] R. Larson, B.H. Edwards, *Calculus* (9th ed.), Brooks/Cole. ISBN 0-547-16702-4 (2009).

[96] G.B. Thomas, M.D. Weir, J.T. Hass, *Thomas' Calculus: Early Transcendentals* (12th ed.), Addison-Wesley. ISBN 0-321-58876-2 (2010).

[97] G. Branko, *Convex polytopes* (2nd ed.), New York & London: Springer-Verlag, ISBN 0-387-00424-6 (2003).

[98] J.A. Nelder and R. Mead., The Computer Journal **7**, 308–313 (1965).

[99] Brett Champion, Adam Strzebonski, *Constrained Optimization*, Wolfram Mathematica Tutorial Collection, Wolfram Research, Inc. (2008).

[100] S. Mehrotra, SIAM Journal on Optimization **2**, 575–601 (1992).

[101] J. Nocedal, J.W. Stephen, *Numerical Optimization (Springer Series in Operations Research)*, Springer-Verlag New York, Inc. (1999).

[102] M.R. Hestenes, Journal of Optimization Theory and Applications, **4** 303–320 (1969).

[103] K. Price and R. Storn, *Procedings of 1996 IEEE International Conference on Evolutionary Computation (ICEC 96)*, 842-844 (1996).

[104] K. V. Price, R. M. Storn and J. A. Lampinen, *Differential Evolution: A Practical Approach to Global Optimization*, Springer-Verlag Berlin Heidelberg (2005).

Appendix A

Expressions for the Survival Probability

A.1 Survival Probability at the Detector (Full Expression)

Eq. (3.2.3), the general expression for the average survival amplitude of ν_e of energy E_ν from source region in the sun to the detector in the earth is given as:

$$A_{ee} = \sum_{i=1}^{2} A_{ei}^{S} A_{ie}^{E} \texttt{exp}[-im_i^2(L-r)/2E].$$

The respective survival amplitude can be given as:

$$P_{ee} = A_{ee} A_{ee}^{*} \tag{A.1.1}$$

$$\Rightarrow \qquad P_{ee} = \sum_{i=1}^{2}\sum_{k=1}^{2} A_{ei}^{S} A_{ie}^{E} e^{\frac{-im_i^2(L-r)}{2E}} A_{ek}^{S^*} A_{ke}^{E^*} e^{\frac{-im_k^2(L-r)}{2E}} \tag{A.1.2}$$

$$\begin{aligned} \Rightarrow \qquad P_{ee} &= |A_{e1}^{S}|^2|A_{1e}^{E}|^2 + |A_{e1}^{S}|^2|A_{1e}^{E}|^2 \\ &+(A_{e1}^{S})(A_{1e}^{E})(A_{e2}^{S^*})(A_{2e}^{E^*})e^{-i\frac{(L-r)}{2E}(m_1^2-m_2^2)} \\ &+(A_{e2}^{S})(A_{2e}^{E})(A_{e1}^{S^*})(A_{1e}^{E^*})e^{-i\frac{(L-r)}{2E}(m_2^2-m_1^2)}. \end{aligned} \tag{A.1.3}$$

Let $A_{e1}^{S} = |A_{e1}^{S}|e^{ia}$, $A_{e2}^{S} = |A_{e2}^{S}|e^{ib}$, $A_{1e}^{E} = |A_{1e}^{E}|e^{ic}$ and $A_{2e}^{E} = |A_{2e}^{E}|e^{id}$, then using the notations described in the section 3.2, the above expression comes:

$$\begin{aligned} P_{ee} &= P_1P_{1e} + P_2P_{2e} \\ &+\sqrt{P_1P_2P_{1e}P_{2e}}e^{i(a-b)}e^{i(c-d)}e^{-i\frac{(L-r)}{2E}(m_1^2-m_2^2)} \\ &+\sqrt{P_1P_2P_{1e}P_{2e}}e^{i(a-b)}e^{i(c-d)}e^{i\frac{(L-r)}{2E}(m_1^2-m_2^2)} \end{aligned} \tag{A.1.4}$$

By a simple treatment above expression can be written as:

$$P_{ee} = P_1 P_{1e} + P_2 P_{2e} + 2\sqrt{P_1 P_2 P_{1e} P_{2e}} \cos\zeta, \tag{A.1.5}$$

where, $\zeta = \frac{\Delta m^2 (L-r)}{2E} + \delta$ with $\Delta m^2 = m_1^2 - m_2^2$ and $\delta = a - b + c - d$.

A.2 The Survival Probability P_{SE} at the Detector (Analytical Expression)

Here we prove the Eq.(3.2.6) given as:

$$P_{SE}(\nu_e) = P_S(\nu_e) + \frac{[2P_S(\nu_e) - 1][\sin^2\theta - P_{2e}]}{\cos 2\theta}$$

An arbitrary state of neutrino at sun surface in mass basis can be written as:

$$|\psi(t=0)\rangle = A_1(0)|\nu_1\rangle + A_2(0)|\nu_2\rangle. \tag{A.2.1}$$

At earth surface neutrino state can be written as:

$$|\psi(t)\rangle = A_1 e^{-iE_1 t}|\nu_1\rangle + A_2 e^{-iE_2 t}|\nu_2\rangle. \tag{A.2.2}$$

By inner product with $|\nu_e\rangle$ on both sides, we get:

$$\langle\nu_e|\psi(t)\rangle_E = A_1 e^{-iE_1 t}\langle\nu_e|\nu_1\rangle + A_2 e^{-iE_2 t}\langle\nu_e|\nu_2\rangle$$

Using Eq. 2.4.16, the expression for the probability amplitude at the earth surface becomes:

$$A_S(\nu_e) = A_1 e^{-iE_1 t}\cos\theta + A_2 e^{-iE_2 t}\sin\theta$$

The corresponding probability, neglecting phase terms, at the earth's surface becomes:

$$P_S(\nu_e) = A_S(\nu_e)A_S(\nu_e)^* = |A_1|^2\cos^2\theta + |A_2|^2\sin^2\theta$$

For ν_e and ν_μ above expression can be written as:

$$\begin{cases} P_S(\nu_e) = P_1(\nu_1)\cos^2\theta + P_2(\nu_2)\sin^2\theta \\ P_S(\nu_\mu) = P_1(\nu_1)\sin^2\theta + P_2(\nu_2)\cos^2\theta \end{cases} \tag{A.2.3}$$

Above expression gives equation (A1) of ref. [85] given as:

$$\begin{bmatrix} P_S(\nu_e) \\ P_S(\nu_\mu) \end{bmatrix} = \begin{bmatrix} \cos^2\theta & \sin^2\theta \\ \sin^2\theta & \cos^2\theta \end{bmatrix} \begin{bmatrix} P_1(\nu_1) \\ P_2(\nu_2) \end{bmatrix}. \tag{A.2.4}$$

A similar expression for the probability $P_{SE}(\alpha)$ of ν_2 state at earth surface to be detected as ν_α at the detector, with $P_{2e} = \sin^2\theta$, after passing through the earth is given as:

$$\begin{bmatrix} P_{SE}(\nu_e) \\ P_{SE}(\nu_\mu) \end{bmatrix} = \begin{bmatrix} 1 - P_{2e} & P_{2e} \\ P_{2e} & 1 - P_{2e} \end{bmatrix} \begin{bmatrix} P_1(\nu_1) \\ P_2(\nu_2) \end{bmatrix}, \tag{A.2.5}$$

where P_{2e} is the probability of the transition $\nu_2 \to \nu_e$ in the earth. Now eliminating $P_2(\nu_2)$ in Eq. (A.2.4), we get:

$$P_S(\nu_e)\cos^2\theta - P_S(\nu_\mu)\sin^2\theta = P_1(\nu_1)(\cos^4\theta - \sin^4\theta)$$

$$\begin{aligned} P_1(\nu_1)\cos 2\theta &= P_S(\nu_e)\cos^2\theta - P_1(\nu_\mu)\sin^2\theta \\ P_1(\nu_1) &= \frac{P_S(\nu_e)\cos^2\theta - [1 - P_1(\nu_e)]\sin^2\theta}{\cos 2\theta} \\ P_1(\nu_1) &= \frac{P_S(\nu_e) - \sin^2\theta}{\cos 2\theta} \end{aligned} \tag{A.2.6}$$

Form Eq. (A.2.5), we have:

$$P_{SE}(\nu_e) = [1 - P_{2e}]P_1(\nu_1) + P_{2e}P_2(\nu_2)$$

By eliminating $P_2(\nu_2)$, we get:

$$P_{SE}(\nu_e) = [1 - P_{2e}]P_1(\nu_1) + P_{2e}[1 - P_1(\nu_1)]$$

$$P_{SE}(\nu_e) = P_1(\nu_1)[1 - 2P_{2e}] + P_{2e}$$

Putting the value of $P_1(\nu_1)$ from Eq. A.2.6, we get:

$$P_{SE}(\nu_e) = \frac{[P_S(\nu_e) - \sin^2\theta][1 - 2P_{2e}]}{\cos 2\theta} + P_{2e}$$

Simplifying above expression we get required result:

$$P_{SE}(\nu_e) = P_S(\nu_e) + \frac{[2P_S(\nu_e) - 1][\sin^2\theta - P_{2e}]}{\cos 2\theta}.$$

A.3 Day Time Survival Probability at the Earth Surface (Numerical Solution)

The relations between neutrino states in flavour and mass bases are given as:

$$\begin{cases} |\nu_1\rangle = \cos\theta|\nu_e\rangle - \sin\theta|\nu_\mu\rangle \\ |\nu_2\rangle = \sin\theta|\nu_e\rangle + \cos\theta|\nu_\mu\rangle \end{cases} \tag{A.3.1}$$

$$\begin{cases} |\nu_e\rangle = \quad \cos\theta|\nu_1\rangle + \sin\theta|\nu_2\rangle \\ |\nu_\mu\rangle = -\sin\theta|\nu_1\rangle + \cos\theta|\nu_2\rangle \end{cases} \tag{A.3.2}$$

An arbitrary neutrino state in mass and flavour bases can be written as:

$$|\psi(0)\rangle = A_1|\nu_1\rangle + A_2|\nu_2\rangle \tag{A.3.3}$$

$$|\psi(0)\rangle = A_e|\nu_e\rangle + A_\mu|\nu_\mu\rangle \tag{A.3.4}$$

Usinf Eq. (A.3.2) in Eq. (A.3.4), we get

$$|\psi(0)\rangle = (A_e\cos\theta - A_\mu\sin\theta)|\nu_1\rangle + (A_e\sin\theta + A_\mu\cos\theta)|\nu_2\rangle \tag{A.3.5}$$

Comparing Eqs. (A.3.5) and (A.3.3), we get amplitudes of neutrino mass states as:

$$A_1 = A_e\cos\theta - A_\mu\sin\theta \tag{A.3.6}$$

$$A_2 = A_e\sin\theta + A_\mu\cos\theta \tag{A.3.7}$$

Let ν_e travels from source region in the sun and reach the sun surface as ν_1 that travels from sun surface and is detected at earth surface as ν_e after time t. We find numerically A_e and A_μ at sun surface and put in above equations to find A_1 and A_2. The state function after time t can be given as:

$$|\psi(t)\rangle = A_1 e^{-iE_1 t}|\nu_1\rangle + A_2|e^{-iE_2 t}\nu_2\rangle \tag{A.3.8}$$

Using Eq. (A.3.1) in Eq. (A.3.8), we get

$$|\psi(t)\rangle = (A_1\cos\theta e^{-iE_1 t} + A_2\sin\theta e^{-iE_2 t})|\nu_e\rangle + (-A_1\sin\theta e^{-iE_1 t} + A_2\cos\theta e^{-iE_2 t})|\nu_\mu\rangle \tag{A.3.9}$$

Comparing with Eq. (A.3.4), we get survival amplitude of electron neutrino at earth surface as:

$$A_e = A_1\cos\theta e^{-iE_1 t} + A_2\sin\theta e^{-iE_2 t} \tag{A.3.10}$$

Its complex conjugate can be given as:

$$A_e^* = A_1^* \cos\theta e^{iE_1 t} + A_2 \sin\theta e^{iE_2 t} \tag{A.3.11}$$

The corresponding survival probability at the earth surface becomes:

$$\begin{aligned} P_e = A_e A_e^* = |A_1|^2 \cos^2\theta + |A_2|^2 \sin^2\theta + \\ A_1^* A_2^* \cos\theta \sin\theta e^{-i(E_1 - E_2)t} + \\ A_2^* A_1^* \sin\theta \cos\theta e^{i(E_1 - E_2)t} \end{aligned} \tag{A.3.12}$$

Assuming $A_1 = |A_1| e^{i\epsilon_1}$, $A_2 = |A_2| e^{i\epsilon_2}$, the above expression comes:

$$P_e = |A_1|^2 \cos^2\theta + |A_2|^2 \sin^2\theta + |A_1||A_2| \sin 2\theta \cos[(E_1 - E_2)t - \epsilon], \tag{A.3.13}$$

where $\epsilon = \epsilon_1 - \epsilon_2$.

From Eqs. (2.4.10) and (2.4.13) $\frac{(E_1 - E_2)t}{2} = \frac{\Delta m^2 R}{4E}$ and $R = L - r$ (distance traveled from the Sun's surface to the earth's surface) from figure 3.1. The above expression can be written as:

$$P_e = P_1 \cos^2\theta + P_2 \sin^2\theta + \sqrt{P_1 P_2} \sin 2\theta \cos\left[\frac{\Delta m^2 (L - r)}{2E} + \epsilon\right] \tag{A.3.14}$$

or

$$P_e = P_1 \cos^2\theta + P_2 \sin^2\theta + \sqrt{P_1 P_2} \sin 2\theta \cos\xi, \tag{A.3.15}$$

where phase $\xi = \frac{\Delta m^2 (L - r)}{2E} + \epsilon$.

Commun. Theor. Phys. **59** (2013) 324–330 Vol. 59, No. 3, March 15, 2013

Optimization of Neutrino Oscillation Parameters Using Differential Evolution

Ghulam Mustafa,* Faisal Akram,† and Bilal Masud‡

Centre for High Energy Physics, University of the Punjab, Lahore (54590), Pakistan

(Received October 26, 2012)

Abstract *We show how the traditional grid based method for finding neutrino oscillation parameters Δm^2 and $\tan^2\theta$ can be combined with an optimization technique, Differential Evolution (DE), to get a significant decrease in computer processing time required to obtain minimal chi-square (χ^2) in four different regions of the parameter space. We demonstrate efficiency for the two-neutrinos case. For this, the χ^2 function for neutrino oscillations is evaluated for grids with different density of points in standard allowed regions of the parameter space of Δm^2 and $\tan^2\theta$ using experimental and theoretical total event rates of chlorine (Homestake), Gallex+GNO, SAGE, Superkamiokande, and SNO detectors. We find that using DE in combination with the grid based method with small density of points can produce the results comparable with the one obtained using high density grid, in much lesser computation time.*

PACS numbers: 14.60.Pq, 26.65.+t, 02.60.Pn
Key words: solar neutrinos, neutrino masses and mixing, numerical optimization

1 Introduction

The flux of solar neutrino was first measured by Raymond Davis Junior and John N. Bahcall at Homestake in late 1960s and a deficit was detected between theory i.e., Standard Solar Model (SSM) and experiment. This deficit is known as Solar Neutrino Problem.[1] Several theoretical attempts have been made to explain this deficit.[2] One of these is neutrino oscillations, the change of electron neutrinos to another neutrino flavour during their travel from a source point in the sun to the detector at the earth surface.[3] There was no experimental proof for the neutrino oscillations until 2002 when Sudbury Neutrino Observatory (SNO) provided strong evidence for neutrino oscillations.[4] The exact amount of depletion, which may be caused by the neutrino oscillations, however, depends upon the neutrinos' mass-squared difference $\Delta m^2 \equiv m_2^2 - m_1^2$ and mixing angle θ, in the interval $[0, \pi/2]$, defining the relation between flavor eigen-states and mass eigen-states of the neutrinos.

The data from different neutrino experiments have provided the base to explore the field of neutrino physics. In global analysis of solar neutrino data, theoretically expected event rates, with oscillations, at different detector locations are calculated and combined with experimental event rates statistically through the chi-square (χ^2) function, as defined below by Eq. (1), for a grid of values of the parameters Δm^2 and $\tan^2\theta$. The values of these parameters with minimum chi-square in different regions of the parameter space suggest different oscillation solutions. The names of these solutions, found in the literature, along with specification of the respective region in the parameter space are: Small Mixing Angle (SMA: $10^{-4} \leq \tan^2\theta \leq 3\times10^{-2}$, 3×10^{-7} eV^2 $\leq \Delta m^2 \leq 10^{-4}$ eV^2), Large Mixing Angle (LMA: $3\times10^{-2} \leq \tan^2\theta \leq 2$, 2×10^{-6} eV^2 $\leq \Delta m^2 \leq 10^{-3}$ eV^2), Low Probability Low Mass (LOW: $3\times10^{-2} \leq \tan^2\theta \leq 2$, 10^{-8} eV^2 $\leq \Delta m^2 \leq 2\times10^{-6}$ eV^2) and Vacuum Oscillation (VO: $0.1 \leq \tan^2\theta \leq 1$, 10^{-11} eV^2 $\leq \Delta m^2 \leq 10^{-8}$ eV^2).[5] Extensive work has been done on the global analysis of solar neutrino data[6−16] and now is the era of precision measurement of the neutrino oscillation parameters.[17−18]

Traditionally, the whole parameter space (10^{-13} eV^2 $\leq \Delta m^2 \leq 10^{-3}$ eV^2, $10^{-4} \leq \tan^2\theta \leq 10$) is divided into a grid of points by varying the logarithm of each parameter uniformly. The density of points in the grid is usually taken as 50×50 point per decade (ppd), in logarithmic scale of the parameters Δm^2 and $\tan^2\theta$, which corresponds to 500×250 points in the whole parameter space. The chi-square values are calculated for each point in the parameter space either by using ^{8}B flux constrained by the SSM in our case or by using unconstrained ^{8}B flux[10] where it is varied about the value predicted by the Standard Solar Model. The global minimum chi-square value $\chi^2_{\rm min}$ is found and $100\beta\%$ C.L. (Confidence Level) contours are drawn in the $\tan^2\theta - \Delta m^2$ plane by joining points with $\chi^2 = \chi^2_{\rm min} + \Delta\chi^2$ for different confidence levels. From the chi-square distribution one can easily find that $\Delta\chi^2 = 2.28, 4.61, 5.99, 9.21, 11.83$ for 68%, 90%, 95%, 99% and 99.73% C.L. (with $\beta = 0.68$, 0.90, 0.95, 0.99 and 0.9973 respectively) for two degrees of freedom (d.o.f.). Minimum chi-square values are found in all the regions and the goodness-of-fit (g.o.f) corresponding to each of the minimum chi-square is calculated. To find each g.o.f. the chi-square distribution is used and $100(1-\beta)\%$ confidence level, corresponding to the minimum chi-square in the region and the d.o.f. of the analysis, is calculated.[5,10] It is

*E-mail: g_mustafa61@yahoo.com
†E-mail: faisal.chep@pu.edu.pk
‡E-mail: bilalmasud.chep@pu.edu.pk

observed that the results of this analysis depend upon the choice of density of points in the parameter space. Increasing the grid density generally produces the results with lower chi-square and better g.o.f., but also requires high computing power. This limitation motivates us to explore other optimization techniques more efficient than simple grid based method. One such technique is the Differential Evolution (DE). It is a population based stochastic algorithm for optimization of real valued non-linear non-differentiable objective functions that has become very popular during the last decade. We combine DE technique with the grid based method for the optimization of Δm^2 and $\tan^2\theta$. The result of this combined analysis are compared with the simple grid based method with different choices of grid density. We have used the terms "small density", "large density" and "very large density" for different density grids. Our results show that DE in combination with grid based method with small density of points can produce the results of global analysis of solar neutrino data obtained with very large density of points. This saves a lot of computing time.

The paper is organized as follows: In Sec. 2, we define the chi-square (χ^2) function for the solar neutrino oscillations that is used as objective function for DE algorithm as well as for the traditional method. In Sec. 3, we describe resulting values of the parameters with minimum chi-square along with respective g.o.f. in standard allowed regions for different density grids. In Sec. 4 we give our respective results obtained using DE. Some concluding remarks are made in the Sec. 5. Algorithm of DE is described in Appendix A.

2 Chi-Square (χ^2) Function Definition

In our χ^2 analysis, we used the updated data of total event rates of different solar neutrino experiments. We followed the χ^2 definition of Ref. [19] and included chlorine (Homestake),[20] weighted average of Gallex and GNO[21] SAGE,[22] Superkamiokande,[23] SNO CC (Charged Current) and SNO NC (Neutral Current)[24] total rates. Expression for the χ^2 function is given as:

$$\chi^2_{\rm Rates} = \sum_{j_1,j_2=1,6} (R^{\rm th}_{j_1} - R^{\rm exp}_{j_1})[V_{j_1 j_2}]^{-2}(R^{\rm th}_{j_2} - R^{\rm exp}_{j_2})\,, \quad (1)$$

where $R^{\rm th}_j$ is the theoretically calculated event rate with oscillations at detector j and $R^{\rm exp}_j$ is the measured rate. For chlorine, Gallex+GNO and SAGE experiments $R^{\rm th}$ and $R^{\rm exp}$ are in the units of SNU (1 SNU=10^{-36} captures/atom/sec) and for Superkamiokande, SNO CC and SNO NC, these are used as ratio to SSM Eq. (8) below. $V_{j_1 j_2}$ is the error matrix that contains experimental (systematic and statistical) errors and theoretical uncertainties that affect solar neutrino fluxes and interaction cross sections. For calculating the error matrix $V_{j_1 j_2}$ we followed Ref. [19] and for updated uncertainties we used Ref. [25]. For calculating the theoretical event rates, using Eqs. (4)–(7) below, we first found the time average survival probabilities, over the whole year, of electron neutrino $\langle P^k_{ee}(E_\nu)\rangle$ (E_ν is the neutrino energy in MeV) at the detector locations for the $k^{\rm th}$ neutrino source and for a grid of values of $\Delta m^2/E_\nu$ and $\tan^2\theta$ following the prescriptions described in Ref. [10]. For uniform grid interval distribution we used the parameters $\Delta m^2/E_\nu$ and $\tan^2\theta$ as exponential functions of the variables x_1 and x_2 as:

$$\frac{\Delta m^2}{E_\nu} = 10^{(0.1x_1-13)}\,, \quad (2)$$

$$\tan^2\theta = 10^{-2(2-0.025x_2)}\,, \quad (3)$$

so that discrete values of x_1 and x_2 from 0 to 100 cover the entire $\tan^2\theta - \Delta m^2$ parameter space. We used the expression for the average expected event rate in the presence of oscillation in case of Chlorine and Gallium detectors given as:

$$R^{\rm th}_j = \sum_{k=1\,{\rm to}\,8} \phi_k \int_{E^j_{\rm th}}^{E_{\rm max}} {\rm d}E_\nu \lambda_k(E_\nu)[\sigma_{e,j}(E_\nu)\langle P^k_{ee}(E_\nu)\rangle]. \quad (4)$$

Here $E^j_{\rm th}$ is the process threshold for the j-th detector (j=1,2,3 for Homestake, Gallex+GNO and SAGE respectively). The values of energy threshold $E^j_{\rm th}$ for Cl, Ga detectors are 0.814, 0.233 MeV respectively.[26] ϕ_k are the total neutrino fluxes taken from BS05(OP).[27] Different sources of solar neutrino flux are: pp, pep, hep, ^{7}Be, ^{8}B, ^{13}N, ^{15}O and ^{17}F. For Gallium detector all fluxes contribute whereas for Chlorine detector all fluxes except pp flux contribute. $\lambda_k(E_\nu)$ are normalized solar neutrino energy spectra for different neutrino sources from the sun, taken from Refs. [28–29], and $\sigma_{e,j}$ is the interaction cross section for ν_e in the j-th detector. Numerical data of energy dependent neutrino cross sections for chlorine and gallium experiments is available from Ref. [28].

Superkamiokande and SNO detectors are sensitive for higher energies, so ϕ_k are the total ^{8}B and hep fluxes for these detectors respectively. Expression of the average expected event rate with oscillations for elastic scattering at SK detector is as below:

$$N^{\rm th}_{\rm SK} = \sum_{k=1,2} \phi_k \int_0^{E_{\rm max}} {\rm d}E_\nu \lambda_k(E_\nu)\{\sigma_e(E_\nu)\langle P^k_{ee}(E_\nu)\rangle + \sigma_\mu(E_\nu)[1-\langle P^k_{ee}(E_\nu)\rangle]\}\,. \quad (5)$$

Here σ_e and σ_μ are elastic scattering cross sections for electron and muon neutrinos that we took from Ref. [30].

For the SNO CC reaction, $\nu_e d \to e^- pp$, we calculated event rate using the expression:

$$N^{\rm th}_{\rm CC} = \sum_{k=1,2} \phi_k \int_0^{E_{\rm max}} {\rm d}E_\nu \lambda_k(E_\nu)\sigma_{\rm CC}(E_\nu)\langle P^k_{ee}(E_\nu)\rangle. \quad (6)$$

Here $\sigma_{\rm CC}$ is νd CC cross section of which calculational method and updated numerical results are given in Refs. [31] and [32] respectively.

Expression for the SNO NC reaction, $\nu_x d \to \nu_x pn$ ($x = e, \mu, \tau$), event rate is given as:

$$N^{\rm th}_{\rm NC} = \sum_{k=1,2} \phi_k \int_0^{E_{\rm max}} {\rm d}E_\nu \lambda_k(E_\nu) \times \sigma_{\rm NC}(E_\nu)(\langle P^k_{ee}(E_\nu)\rangle + \langle P^k_{ea}(E_\nu)\rangle)\,. \quad (7)$$

Here $\sigma_{\rm NC}$ is νd NC cross section and $\langle P^k_{ea}(E_\nu)\rangle$ is the time average probability of oscillation of ν_e into any other active neutrino. We used updated version of CC and NC cross section data from the website given in Ref. [32]. In case of oscillation of the ν_e into active neutrino only, $\langle P^k_{ee}(E_\nu)\rangle + \langle P^k_{ea}(E_\nu)\rangle = 1$ and $N^{\rm th}_{\rm NC}$ is a constant.

For superkamiokande[23] and SNO[24] experiments, the event rates come in the unit of 10^6 cm$^{-2}\cdot$s^{-1}. We converted these rates into ratios to SSM predicted rate. We also calculated theoretical event rates as ratios to SSM predicted rate in order to cancel out all energy independent efficiencies and normalizations.[9]

$$R^{\rm th}_j = \frac{N^{\rm th}_j}{N^{\rm SSM}_j}\,. \tag{8}$$

Here $N^{\rm SSM}_j$ ($j = 4, 5, 6$ for SK, SNO CC, and SNO NC respectively) is the predicted number of events assuming no oscillations. We used the SSM BS05(OP)[27] in our calculations. Theoretical event rates, so calculated, were used in Eq. (1) to calculate the chi-square function for different points in the $\tan^2\theta - \Delta m^2$ parameter space.

3 Analysis from Different Density Grids

Table 1 shows oscillation parameters with minimum χ^2 and respective g.o.f. values, in standard allowed regions described in Sec. 1, calculated for different density grids in the parameter space. The density of points in grid-based searches is usually denoted by the number of points per decade (ppd), i.e., the interval between x and $10x$ in logarithmic scale, for each parameter. Different density grids we selected are: 10×20 ppd (small density), 50×50 ppd (large density) and 100×100 ppd (very large density). Calculation of g.o.f. is described in the introduction section. We used chi-square function definition of Sec. 2. Small density grid for Δm^2 and $\tan^2\theta$ was obtained by simply varying x_1 and x_2 in Eqs. (2) and (3) with step size equal to 1. Other grids given in the Table 1 were obtained by varying x_1 and x_2 with appropriate step size.

We see from Table 1 that increasing density of the grid gives the parameters with smaller χ^2 and better goodness-of-fit. The effect is more prominent in LOW and SMA regions. Selecting a finer grid with larger number of points in the parameter space, of course, will give better results but limitations of the computation time restrict us,[5] to a grid with limited density of points. But we point out that even without increasing the number of points in the grid we can get lower χ^2 and better g.o.f. by fine tuning of the oscillation parameters using DE. We describe what we mean by fine tuning and report our results obtained this way in the next section.

4 Optimization of the Chi-square Function Using DE

The steps of the DE algorithm we used, for the optimization of chi-square function, are described in detail in Appendix A. We wrote the subroutine of the chi-square function, denoted by χ^2, following its definition described in Sec. 2, that depends on x_1 and x_2 and used it as objective function of the DE algorithm. We used the survival probabilities $\langle P^k_{ee}(E_\nu)\rangle$ already calculated for the small density grid and interpolated them to the continuous values of x_1 and x_2 to calculate event rates and chi-square function in DE algorithm. We used cubic polynomial fit for the interpolation purpose to fit the data. The results of the interpolated probabilities were verified to be equivalent to the originally calculated probabilities with reasonable accuracy. For each of the four regions we used the point with minimum chi-square of the small density grid, given in Table 1, as the starting point and explored the space around it for the fine tuning using DE. That is, in each region we searched for points with smaller χ^2 values and better g.o.f. of the oscillation parameters.

Table 1 $\chi^2_{\rm min}$ values for 4 d.o.f. (6(rates)-2(parameters: $\tan^2\theta, \Delta m^2$)) and respective goodness-of-fit (g.o.f.) values of the oscillation parameters Δm^2 and $\tan^2\theta$, in standard allowed regions, for different grid sizes in points per decade (ppd) in logarithmic scale of the parameters.

Solution	Grid Size (points per decade) Δm^2	Grid Size (points per decade) $\tan^2\theta$	$\Delta m^2/{\rm eV}^2$	$\tan^2\theta$	$\chi^2_{\rm min}$	g.o.f.
LMA	10	20	$2.512\cdot 10^{-5}$	$3.981\cdot 10^{-1}$	0.808	93.74%
	50	50	$2.512\cdot 10^{-5}$	$3.981\cdot 10^{-1}$	0.808	93.74%
	100	100	$2.455\cdot 10^{-5}$	$3.981\cdot 10^{-1}$	0.805	93.78%
VAC	10	20	$6.31\cdot 10^{-11}$	$1.00\cdot 10^{0}$	1.268	86.68%
	50	50	$6.61\cdot 10^{-11}$	$1.00\cdot 10^{0}$	1.259	86.82%
	100	100	$6.61\cdot 10^{-11}$	$1.00\cdot 10^{0}$	1.259	86.82%
LOW	10	20	$1.00\cdot 10^{-8}$	$1.122\cdot 10^{0}$	4.09	39.46%
	50	50	$3.02\cdot 10^{-8}$	$1.059\cdot 10^{0}$	4.04	40.12%
	100	100	$3.09\cdot 10^{-8}$	$1.029\cdot 10^{0}$	3.968	41.04%
SMA	10	20	$6.31\cdot 10^{-6}$	$1.585\cdot 10^{-3}$	7.78	10.01%
	50	50	$5.74\cdot 10^{-6}$	$1.679\cdot 10^{-3}$	1.949	74.52%
	100	100	$5.46\cdot 10^{-6}$	$1.728\cdot 10^{-3}$	1.86	76.24%

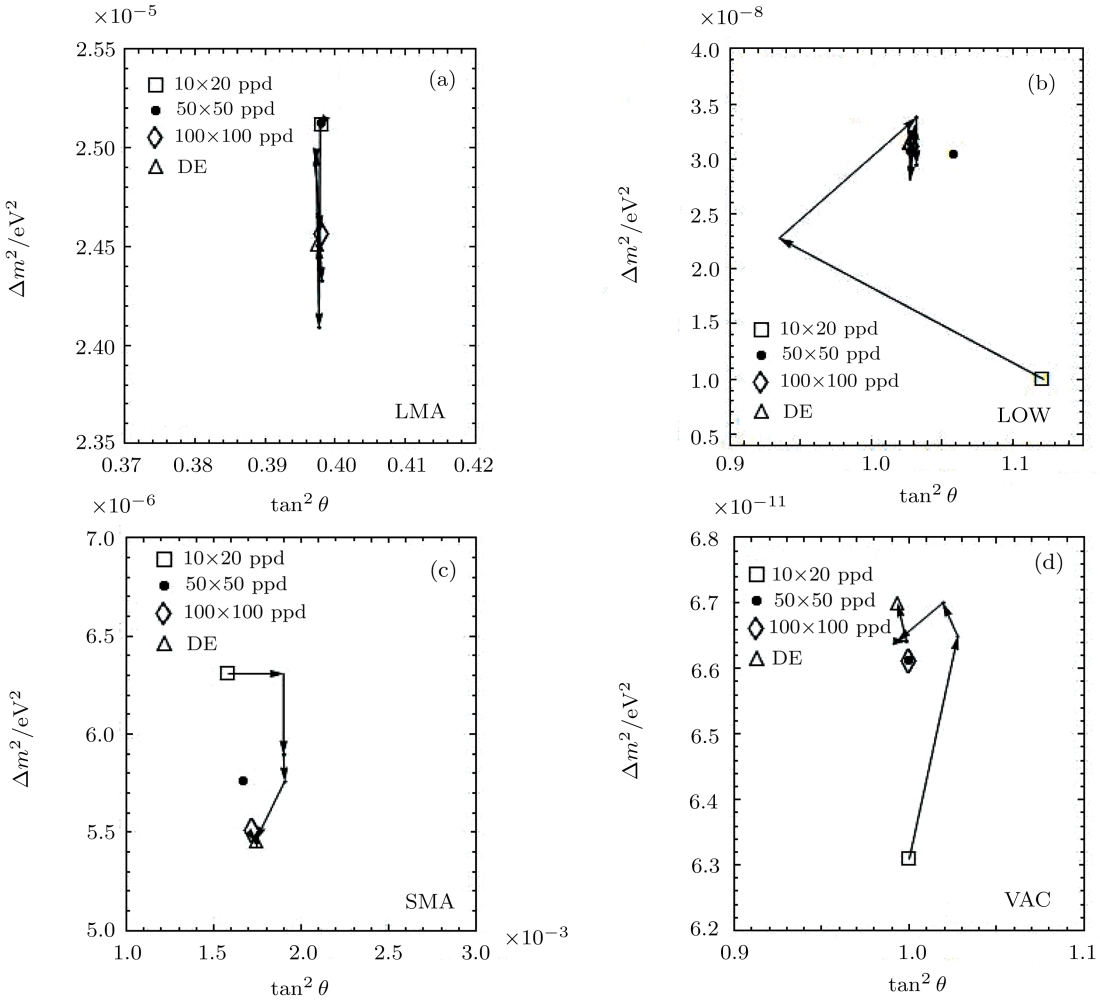

Fig. 1 Track of the DE algorithm for optima in different regions using the strategy DE/best/2/bin are shown by the vector arrows. The symbols □, • and ◊ show the best points of different density grids in units of points per decade (ppd), in logarithmic scale of the parameters Δm^2 and $\tan^2\theta$, shown in Table 1 and triangle symbol △ shows the best point after fine tuning using DE.

In our analysis, the values of DE control variables F and CR were taken as 0.4 and 0.9 respectively for the LMA and VAC regions. For the LOW and SMA regions F and CR were both taken as 0.3 for better convergence. Maximum number of iterations were taken to be 50 for all regions. We took the best point in the small density grid in Table 1 as the first member of the population in the first iteration, as described above, and used the strategy DE/best/2/bin for DE mutation in all the remaining iterations or generations. The steps of DE algorithm, described in Appendix A, were repeated for the number of iterations specified.

Table 2 and Fig. 1 show the results in different regions of parameter space during and after optimization of the parameters using DE. The values of chi-square function after each accepted mutation are given in column 5, whereas, columns 3 and 4 contain the corresponding values of Δm^2 and $\tan^2\theta$. Table 2 also shows that DE causes a small decrease in the value of $\chi^2_{\min}$ and accordingly a small change in the values of Δm^2 and $\tan^2\theta$ for LMA and VAC solutions. This result is consistent with the earlier observation, in grid based method as shown in Table 1, that LMA and VAC solutions are not significantly affected by the increase in the density of points. It is interesting to note that in case of LMA solution a slight decrease in $\chi^2_{\min}$ occurs only when the density of points is taken to be 100×100 ppd, whereas DE obtains the same result within only 50 iterations, with 20 points randomly selected in each iteration. Though the improvement in this case is very modest but it requires much lesser computing time when DE is used instead of the grid based method alone with very large density of points. In case of LOW solution, though DE produces a small decrease in $\chi^2_{\min}$, a significant change in Δm^2 can be noted merely after a few iterations. This result is again consistent with the variations in these parameters when density of point is increased in the grid based method. In case of the SMA solution, we note a large decrease in $\chi^2_{\min}$ and accordingly some change in

Δm^2 and $\tan^2\theta$. Table 2 shows that after merely 7 iterations DE produces the value of Δm^2 which we obtained with large density grid and after 50 iteration the result of DE were comparable with those obtained using very large density grid. This comparison shows that combining the DE with the grid based method using a small density grid can produce the results of global analysis of solar neutrino data obtained by using a large or even very large density grid in much lesser computing time. The same results are also shown by Fig. 1 in which progress in values of Δm^2 and $\tan^2\theta$ due to DE is represented by vectors. For comparison, the results of grid based method using different density of points are also shown in the same figure by different symbols.

Table 2 The results of the oscillation parameters during different iterations of the DE algorithm. The improved values of the oscillation parameters Δm^2 and $\tan^2\theta$ along with $\chi^2_{\rm best}$ (4 d.o.f) and g.o.f. using Differential Evolution strategy DE/best/2/bin corresponding to Fig. 1 are presented. Note in the 1^{st} row of different standard regions, the points with minimum chi-square of the small density grid given in Table 1 are taken as first members of the population arrays. The other members of the arrays, for different regions, are selected randomly using DE.

Solution	Iterations	$\Delta m^2/\text{eV}^2$	$\tan^2\theta$	$\chi^2_{\rm min}$	$\chi^2_{\rm best}$	g.o.f.
	1–7	$2.511\,89\cdot10^{-5}$	$3.981\,07\cdot10^{-1}$	0.808 314		93.77%
	8–9	$2.509\,99\cdot10^{-5}$	$3.978\,55\cdot10^{-1}$	0.807 316		
10–13	$2.409\,27\cdot10^{-5}$	$3.976\,84\cdot10^{-1}$		0.804 711		
	14	$2.497\,98\cdot10^{-5}$	$3.972\,87\cdot10^{-1}$	0.804 564		
LMA	15	$2.493\,07\cdot10^{-5}$	$3.970\,28\cdot10^{-1}$	0.804 289		
	16	$2.458\,84\cdot10^{-5}$	$3.979\,12\cdot10^{-1}$	0.804 424		
	17–21	$2.466\,33\cdot10^{-5}$	$3.9751\cdot10^{-1}$	0.803 315		
22–29	$2.432\,64\cdot10^{-5}$	$3.980\,97\cdot10^{-1}$		0.803 192		
30–50	$2.450\,84\cdot10^{-5}$	$3.9751\cdot10^{-1}$	0.802 953	0.802 953		93.82%
	1	$6.309\,57\cdot10^{-11}$	1.0	1.267 79		86.72%
	2-3	$6.649\,77\cdot10^{-11}$	1.0277	1.260 239		
VAC	4–6	$6.706\,41\cdot10^{-11}$	1.019 12	1.259 77		
	7–43	$6.6423\cdot10^{-11}$	0.993 134	1.259 48		
	44–45	$6.6423\cdot10^{-11}$	0.998 353	1.259 45		
	46–50	$6.700\,41\cdot10^{-11}$	0.993 26	1.259 39	1.259 39	86.82%
	1	$6.309\,57\cdot10^{-6}$	$1.584\,89\cdot10^{-3}$	7.779 33		10.01%
	2–5	$5.897\,98\cdot10^{-6}$	$1.899\,28\cdot10^{-3}$	2.995 11		
SMA	6–7	$5.762\,76\cdot10^{-6}$	$1.906\,13\cdot10^{-3}$	2.803 98		
	8–15	$5.4608\cdot10^{-6}$	$1.739\,79\cdot10^{-3}$	1.823 35		
	16–50	$5.455\,14\cdot10^{-6}$	$1.7452\cdot10^{-3}$	1.821 26	1.821 26	76.89%
	1	$1.0\cdot10^{-8}$	1.122 08	4.188 97		39.46%
	2–4	$2.378\,07\cdot10^{-8}$	1.031 98	3.983 39		
	5–9	$2.954\,04\cdot10^{-8}$	1.031 98	3.976 24		
LOW	10	$3.3042\cdot10^{-8}$	1.030 69	3.976 05		
	11	$2.807\,96\cdot10^{-8}$	1.027 41	3.9728		
	12–20	$3.173\,57\cdot10^{-8}$	1.027 41	3.962 67		
	21–50	$3.145\,43\cdot10^{-8}$	1.027 23	3.961 25	3.961 25	41.12%

5 Conclusions

Fine tuning of the neutrino oscillation parameters using Differential Evolution has been introduced as a solution to the impasse faced due to computation limitations of the larger density grid alternative. We find that the results of combining DE with the grid based method using small density grid, described in Sec. 4, are comparable with those obtained through grid based method alone with large and very large density of points, after 10 and 50 iterations of DE algorithm, with 20 points selected in each iteration respectively. Thus DE approaches to the optima in much lesser computing time as compared to the grid based method alone. So we conclude that combining DE with grid based method, a small density grid can produce the results of the analysis of solar neutrino data with very large density of points in the parameter space. As we go from large to very large density grid, the χ^2 value changes in some cases, indicating that the saturation is not achieved. The implied need for going beyond even the presently accessible very large density can be satisfied if we combine the very large density with DE while using only a manageable computing time. In the present work we have not included the energy bin data of SK and SNO experiments and the reactor neutrino data for the sake of simplicity to check the implementation and efficiency of the DE technique. However, this study shows that the

introduced technique represents a useful methodological advancement in analysis of solar neutrino data that could be applied to more up-to-date data.

Appendix

Algorithm of Differential Evolution

The general algorithm of DE[33] for minimizing an objective function carries out a number of steps. Here we summarize the steps we carried out for minimizing the χ^2 function defined in Sec. 2. We did optimization of the χ^2 function individually for different regions of the parameter space to do one fine tuning in each region.

Step 1 An array of vectors was initialized to define a population of size NP = 20 with $D = 2$ parameters as

$$x_i = x_{j,i} \text{ where } i = 1, 2, \ldots, \text{NP} \text{ and } j = 1, \ldots, D\,. \quad \text{(A1)}$$

The parameters, involved here, are x_1 and x_2 of Eqs. (2) and (3) on which $\Delta m^2/E_\nu$ and $\tan^2\theta$ depend. Upper and lower bounds ($b_{j,U}$ and $b_{j,L}$), individually for different regions of the parameter space described in the introduction section, for the x values were specified and each vector i was assigned a value according to

$$x_{j,i} = \text{rand}_j(0,1) \cdot (b_{j,U} - b_{j,L}) + b_{j,L}\,, \quad \text{(A2)}$$

where $\text{rand}_j \in [0,1]$ is j-th evaluation of a uniform random number generator. The χ^2 function was calculated for each vector of the population and the vector with least χ^2 value was selected as base vector $\boldsymbol{x}_{r_0}$.

Step 2 Weighted difference of two randomly selected vectors from the population was added to the base vector $\boldsymbol{x}_{r_0}$ to produce a mutant vector population $\boldsymbol{v}_i$ of NP trial vectors. The process is known as mutation.

$$v_i = x_{r_0} + F \cdot (x_{r_1} - x_{r_2})\,. \quad \text{(A3)}$$

Here the scale factor $F \in [0,2]$ is a real number that controls the amplification of the differential variation. The indices r_1, $r_2 \in [1, \text{NP}]$ are randomly chosen integers and are different from r_0.

Different variants of DE mutation are denoted by the notation "DE/x/y/z", where x specifies the vector to be mutated which can be "rand" (a randomly chosen vector) or "best" (the vector of the lowest χ^2 value from the current population), y is the number of difference vectors used and z is the crossover scheme. The above mentioned variant Eq. (11) is DE/best/1/bin, where the best member of the current population is perturbed with $y = 1$ and the scheme bin indicates that the crossover is controlled by a series of independent binomial experiments. The two variants, reported in Refs. [34–35], very useful for their good convergence properties, are DE/rand/1/bin

$$v_i = x_{r_1} + F \cdot (x_{r_2} - x_{r_3})\,, \quad \text{(A4)}$$

and DE/best/2/bin

$$v_i = x_{r_0} + F \cdot (x_{r_1} + x_{r_2} - x_{r_3} - x_{r_4})\,. \quad \text{(A5)}$$

For our problem, we used the variant DE/best/2/bin Eq. (13) for DE mutation, where 2 difference vectors ($x_{r_1} - x_{r_3}$ and $x_{r_2} - x_{r_4}$) were added to the base vector. The values of F we used are reported in Sec. 4.

Step 3 The parameters of mutant vector population Eq. (13) were mixed with the parameters of target vectors Eq. (9) in a process called uniform crossover or discrete recombination. After the cross over the trial vector became:

$$u_i = u_{j,i} = \begin{cases} v_{j,i} & \text{if } (\text{rand}_j(0,1) \le \text{Cr or } j = j_{\text{rand}}), \\ x_{j,i} & \text{otherwise.} \end{cases} \quad \text{(A6)}$$

Here $\text{Cr} \in [0,1]$ is the cross over probability that controls fraction of the parameters inherited from the mutant population (the values of Cr we used are given in Sec. 4), $\text{rand}_j \in [0,1]$ is the output of a random number generator and $j_{\text{rand}} \in [1,2]$ is a randomly chosen index.

Step 4 The χ^2 function was evaluated for each of the trial vector u_i obtained from Eq. (14). If the trial vector resulted in lower objective function than that of the target vector x_i, it replaced the target vector in the following generation. Otherwise the target vector was retained. (This operation is called selection.) Thus the target vector for the next generation became:

$$x'_i = \begin{cases} u_i & \text{if } \chi^2(u_i) \le \chi^2(x_i), \\ x_i & \text{otherwise.} \end{cases} \quad \text{(A7)}$$

The processes of mutation, crossover and selection were repeated until the optimum was achieved or the number of iterations (generations) specified in Sec. 4 were completed.

Acknowledgments

We are thankful to the Higher Education Commission (HEC) of Pakistan for its financial support through Grant No.17-5-2(Ps2-044) HEC/Sch/2004.

References

[1] J.N. Bahcall, Scientific American **221** (1969) 28.

[2] N. Hata, S. Bludman, and P. Langacker, Phys. Rev. D **49** (1994) 3622.

[3] L. Wolfenstein, Phys. Rev. D **17** (1978) 2369.

[4] Q.R. Ahmad, *et al.*, Phys. Rev. Lett. **89** (2002) 011301.

[5] M.V. Garzelli and C. Giunti, Astroparticle Physics **17** (2002) 205.

[6] J.N. Bahcall, P.I. Krastev, and A.Yu. Smirnov, Phys. Rev. D **58** (1998) 096016.

[7] M.C. Gonzalez-Garcia, *et al.*, Nuclear Physics B **573** (2000) 3.

[8] M.C. Gonzalez-Garcia and C. Peña-Garay, Nuclear Physics B (Proc. Suppl.) **91** (2001) 80.

[9] M.C. Gonzalez-Garcia and C. Peña-Garay, Phys. Rev. D **63** (2001) 073013.

[10] J.N. Bahcall, P.I. Krastev, A.Yu. Smirnov, and J. High Energy Phys. **05** (2001) 15.

[11] J.N. Bahcall, M.C. Gonzalez-Garcia, and C. Peña-Garay, J. High Energy Phys. **08** (2001) 014.

[12] P.I. Krastev and A.Yu. Smirnov, Phys. Rev. D **65** (2002) 073022.

[13] J.N. Bahcall, M.C. Gonzalez-Garcia, and C. Peña-Garay, J. High Energy Phys. **07** (2002) 054.

[14] P.C. de Holanda and A.Yu. Smirnov, Phys. Rev. D **66** (2002) 113005.

[15] P. Aliani, *et al.*, Phys. Rev. D **67** (2003) 013006.

[16] S. Goswami, A. Bandyopadhyayb, and S. Choubey, Nuclear Physics B (Proc. Suppl.) **143** (2005) 121.

[17] P. Yang and Q.Y. Liu, Chin. Phys. Lett. **26** (2009) 031401.

[18] P. Yang and Q.Y. Liu, Chin. Phys. Lett. **26** (2009) 081402.

[19] G.L. Fogli and E. Lisi, Astropart. Phys. **3** (1995) 185.

[20] B.T. Cleveland, *et al.*, Astrophys. J. **496** (1998) 505.

[21] C.M. Cattadori, Nuclear Physics B (Proc. Suppl.) **110** (2002) 311.

[22] J.N. Abdurashitov, *et al.*, Phys. Rev. C **80** (200) 015807.

[23] K. Abe, Y. Hayato, *et al.*, Phys. Rev. D **83** (2011) 052010.

[24] B. Aharmim, , S.N. Ahmed, *et al.*, Phys. Rev. Lett. **101** (2008) 111301.

[25] G.L. Fogli and E. Lisi, Phys. Rev. D **62** (2001) 013002.

[26] M.C. Gonzalez-Garcia and Yosef Nir, Rev. Mod. Phys. **75** (2003) 345.

[27] J.N. Bahcall, A.M. Serenelli, and S. Basu, Astrophys. J. **621** (2005) L85.

[28] J.N. Bahcall, *et al.*, Phys. Rev. C **54** (1996) 411; J.N. Bahcall, Phys. Rev. C **56** (1997) 3391.

[29] J.N. Bahcall and R.K. Ulrich, Rev. Mod. Phys. **60** (1988) 297; J.N. Bahcall, Phys. Rev. D **49** (1994) 3923.

[30] J.N. Bahcall, M. Kamionkowski, and A. Sirlin, Phys. Rev. D **51** (1995) 6146.

[31] S. Nakamura, *et al.*, Phys. Rev. C **63** (2001) 034617; S. Nakamura, *et al.*, Phys. Rev. C **73** (2006) 049904(E).

[32] S. Nakamura, *et al.*, Nuclear Physics A **707** (2002) 561.

[33] V.P. Kenneth, M.S. Rainer, and A.L. Jouni, *Differential Evolution: A Practical Approach to Global Optimization*, Springer-Verlag, Berlin, Heidelberg (2005).

[34] R. Storn and K. Price, J. Glob Optim **11** (1997) 341.

[35] K.B. Paul and R. Cliff, Omega **33** (2005) 255.